Vegetation-hydrology dynamics in complex terrain of semiarid areas: 1. A mechanistic approach to modeling dynamic feedbacks

Valeriy Y. Ivanov,[1,2,3] Rafael L. Bras,[1] and Enrique R. Vivoni[4]

[1] Vegetation, particularly its dynamics, is the often-ignored linchpin of the land-surface hydrology. This work emphasizes the coupled nature of vegetation-water-energy dynamics by considering linkages at timescales that vary from hourly to interannual. A series of two papers is presented. A dynamic ecohydrological model [tRIBS + VEGGIE] is described in this paper. It reproduces essential water and energy processes over the complex topography of a river basin and links them to the basic plant life regulatory processes. The framework focuses on ecohydrology of semiarid environments exhibiting abundant input of solar energy but limiting soil water that correspondingly affects vegetation structure and organization. The mechanisms through which water limitation influences plant dynamics are related to carbon assimilation via the control of photosynthesis and stomatal behavior, carbon allocation, stress-induced foliage loss, as well as recruitment and phenology patterns. This first introductory paper demonstrates model performance using observations for a site located in a semiarid environment of central New Mexico.

Citation: Ivanov, V. Y., R. L. Bras, and E. R. Vivoni (2008), Vegetation-hydrology dynamics in complex terrain of semiarid areas: 1. A mechanistic approach to modeling dynamic feedbacks, *Water Resour. Res.*, *44*, W03429, doi:10.1029/2006WR005588.

1. Introduction

[2] Processes within the terrestrial biosphere and atmosphere are intrinsically coupled with the hydrological cycle. This coupling is multidirectional, implying that an individual component of the system is both under the influence of, as well as impacting upon, the remaining parts of the system [*Eagleson*, 1978a, 1978b, 1978c, 1978d, 1978e, 1978f, 1978g, 2002]. Vegetation represents an essential constituent that significantly influences the water and energy balances, establishing bidirectional links with climate [*Foley et al.*, 2000]. Interactions and feedbacks between the climate and biosphere have been the subject of many studies [e.g., *Eltahir*, 1996; *Hutjes et al.*, 1998; *Dickinson*, 2000; *Wang and Eltahir*, 2000; *Pielke*, 2001]. Recently, the interplay between vegetation, climate, and soil has been illustrated in a series of papers: *Rodriguez-Iturbe et al.* [1999a, 1999b], *D'Odorico et al.* [2000], *Laio et al.* [2001a, 2001b], *Guswa et al.* [2002], *Ridolfi et al.* [2000a, 2000b], and *van Wijk and Rodriguez-Iturbe* [2002], among others.

[3] As known from physiological studies [e.g., *Larcher*, 2001], the fundamental variables determining the vegetation structure and function are light, soil moisture, and nutrient supplies. These are diagnostic variables of the fundamental drivers of vegetation development: climate, soil, and topography [*Eagleson*, 2002; *Protopapas and Bras*, 1987; *Rodriguez-Iturbe*, 2000; *Mackay*, 2001]. Modeling of any of the drivers requires the simultaneous treatment of the others in order to capture variations and feedbacks, which may occur over a wide range of temporal and spatial scales [*Band et al.*, 1993].

[4] In the past, hydrology-vegetation modeling has been extremely simplified in at least one of the following contexts: the effects of climate forcing; soil spatial or vertical heterogeneity; and the impact of topography on lateral fluxes and light exposure. Topography, observed to have a significant influence on vegetation distribution [e.g., *Florinsky and Kuryakova*, 1996; *Franklin*, 1998; *Meentemeyer et al.*, 2001; *Dirnbock et al.*, 2002; *Kim and Eltahir*, 2004; *Ben Wu and Archer*, 2005; *Dietrich and Perron*, 2006], is often entirely disregarded. Vegetation itself is commonly considered as a static component with prescribed characteristics in most hydrology models. Understanding the impact of climatic disturbances, topography, and soil variability on plants, however, requires dynamic vegetation modeling across the watershed.

[5] Particularly interesting for hydrologists are ecosystems of arid and semiarid areas, since soil water is generally considered to be the key limiting resource affecting vegetation structure and organization. The mechanisms through which water limitation impacts ecosystems are related to carbon assimilation, via the control of photosynthesis and stomatal closure, as well as nitrogen assimilation, through the control of nitrogen mineralization. This work is oriented, although not entirely limited, toward applications in

---
[1]Department of Civil and Environmental Engineering, Massachusetts Institute of Technology, Cambridge, Massachusetts, USA.
[2]Center for the Environment, Harvard University, Cambridge, Massachusetts, USA.
[3]Now at Department of Civil and Environmental Engineering, University of Michigan, Ann Arbor, Michigan, USA.
[4]Department of Earth and Environmental Science, New Mexico Institute of Mining and Technology, Socorro, New Mexico, USA.

semiarid regions, as will be discussed in the following sections.

1.1. System Dynamics and Low-Level Processes

[6] This work couples a model of plant development to a physically based hydrological model. The approach taken is to build complex dynamics from the interactions of more fundamental, quantifiable, smaller space-timescale processes. The approach is common to many sciences that deal with complex nonlinear systems and examples of similar constructs abound in literature. The chosen approach can be discussed within the hierarchy perspective used in landscape ecology. *Urban et al.* [1987, p. 123] assert that a hierarchy of functional components operating at different scales can be constructed for almost any natural phenomena. A hierarchical analysis of a landscape pattern/phenomenon then needs "...(1)... to define its spatial and temporal scales... (2) to infer which factors generate [it]... (3) to relate [it] to adjacent [hierarchical] levels". *Urban et al.* [1987] consider the last two notions in order to isolate the pattern/phenomenon of interest from hierarchical levels that contribute little toward its understanding. Apparently, both ecologists and hydrologists often encounter the problem of defining just what levels may lead to an important contribution.

[7] In complex systems, the characteristics of higher hierarchical level are generally the result of low-level interactions. Classical studies of chaos and self-organizing, self-similar processes emphasize this point. The same is unequivocally argued with respect to ecosystems [*Levin*, 1998, p. 431]: "Ecosystems are prototypical examples of complex adaptive systems, in which patterns at higher levels emerge from localized interactions and selection processes acting at lower levels. An essential aspect of such systems is nonlinearity, leading to historical dependency and multiple possible outcomes of dynamics". As the knowledge about processes at small spatiotemporal scales is currently more complete than the perception of how these processes integrate at larger scales, one needs to consider multiple hierarchical levels in order to make any compelling mechanistic sense of landscape-scale phenomena and their essential hydrological drivers. Consequently, this work details controls on water, energy, and carbon fluxes at the subhourly scales over elementary vegetation/bare soil patches. While this inherently introduces constraints on space-time application feasibility, the approach has a greater predictive power than methods that limit the number of lower-level interactions. The importance of particular small-scale processes to the outcome of a particular experiment with a well posed mechanistic model is itself a result of the experiment, which many times cannot be predicted or prejudged in highly nonlinear systems. But even if the conclusion is that a particular process is not important to the experiment at hand, the detailed mechanistic approach allows for interpretation and understanding that may not be otherwise possible.

[8] This work emphasizes the dynamic coupling between vegetation and hydrology processes. It accounts for the spatial variability of the topography-controlled rainfall-runoff process, subject to climatic forcing. The scheme parameterizes vegetation dynamics based on plant biophysical and biochemical characteristics and competition for vital resources. These dynamics respond to seasonal and interannual climate forcing and surface hydrological states. Consequently, the ecohydrological model offers the opportunity to explore interactions between vegetation and hydrological mechanisms, which is the goal of the companion paper by *Ivanov et al.* [2008].

1.2. Model Credibility and Data

[9] Before addressing a problem of interest, every model undergoes a series of tests and adjustments. The language defining this process is rich in terms: validation, verification, corroboration, confirmation, and history matching [e.g., *Schlesinger et al.*, 1979; *Konikow and Bredhoeft*, 1992; *Oreskes et al.*, 1994], to name a few. Despite the relative maturity of numerical modeling in the field of geosciences, guidelines constraining the optimal use of models as well as consistent terminology are still being formulated [*Refsgaard and Henriksen*, 2004]. It is important therefore (1) to identify the purposes of tests illustrated in this work and (2) to comment on experiments/observations that could further verify model predictions. Central to the former objective is the notion of *Rykiel* [1996], who argued that validation is a testing of whether a model is acceptable for its intended use. Theoretical validity of the model is nonetheless always provisional [*Rykiel*, 1996], since even successful testing cannot guarantee a flawless model structure and a solid scientific basis. These two statements are echoed by *Bras et al.* [2003] in the discussion of why even "unverified" models are still useful, which leads to conclusions that also pertain to this study. The consistency, or "acceptability", of the developed modeling scheme is demonstrated in various ways. First, a series of controlled tests is illustrated showing that the model agrees well with scientific understanding of the processes involved in vegetation-hydrology interactions. The simulated dynamics are demonstrated for elementary, subdiurnal, basic energy-water-carbon processes. Second, a test case is developed for a site located in a semiarid environment of the Sevilleta National Wildlife Refuge in central New Mexico. The site is covered with a C_4 grass, which is used as the generic vegetation type by *Ivanov et al.* [2008]. The test includes a comparison with several states and fluxes measured at the site and spans various temporal integration scales. At the hourly scale, the time series of net radiation, latent heat flux, and root soil moisture are verified. At larger scales, mean observed and simulated daily cycles of net radiation and ground heat flux are compared. Matched timescales of evapotranspiration response and soil moisture decay as well as dynamics of biomass accumulation provide an additional "confirmation" [*Oreskes et al.*, 1994] of the model consistency.

[10] It should be noted, however, that since there are no generally agreed validation criteria for a model like the one discussed here, the comparison results merely attempt to build confidence that the model performance is physically plausible for the constructed case. In the authors' opinion, the satisfactory comparison of the simulated dynamics and the observed behavior at various time scales is a sufficient metric for the model to be considered as capable of capturing the essential features of vegetation-hydrology dynamics in semiarid areas. Of course, it is hardly possible that all of the used assumptions are absolutely flawless, as is the case for all models [*Oreskes et al.*, 1994; *Rykiel*, 1996]. Nonetheless, progress in ecohydrology will require the use

of numerical models in scenarios for which absolute validation has not yet been achieved. Numerical experiments carried out in a deductive operation mode may stimulate new insights and lead to new observation practices [Bras et al., 2003], a notion that is discussed below.

[11] Complex models require complex suits of observational data. The paucity of data makes it difficult or sometimes even impossible to test all the desired behavioral aspects. This especially concerns cases when a model crosses a number of different disciplines or space-time-scales. A constructive response to this statement from an empirical scientist would be "What does your model need?" A few ideas are outlined here, patterned for a deductive setting in which the model will be used, but may be general enough for similarly oriented frameworks.

[12] First, a model needs unambiguous forcing in terms of space-, time-, and process partition. Much has been said about precipitation, on the other hand, most ecological models require photosynthetically active radiation as input, partitioned into both direct and diffuse components. There are few stations nationwide that provide this information and no general method exists on how to partition the global shortwave flux, a more commonly measured variable. Second, observations of above and below ground compartments are equally important. By far, numerical conceptualization of below ground processes is most difficult, while observational practices are commonly biased toward the above ground states and fluxes. Third, a spatially explicit model requires spatial observations at the commensurate averaging scale with a measure of associated uncertainty. For example, a biomass estimate can be obtained these days from remotely sensed data. However, an inverse radiative transfer model is used to generate the estimate and thus the associated uncertainty bounds are needed to make a valid comparison. Fourth, observations must span all seasons and, preferably, be long term. The continuity of data is often overlooked but it is well known that even a theoretically incorrect model can be tuned to perform satisfactorily at the "event scale". Evaluation of the model performance over longer timescales is the key and data exercising the continuous simulation over different scenarios are important. Fifth, and likely one of the most important notions, data must be available for all important processes, reasonably collocated in time and space. Data exhibiting disparate nature in terms of collection periods, measurement focus, quantity, and quality are merely inadequate for consistent model testing. For instance, a common situation is the collection of above ground biomass during a seasonal field campaign. What is the value of these data to a mechanistic modeler if little is known about the dynamics of states below ground, hydrometeorology of the period, and its preceding history? The value of interseasonal energy flux data is also diminished if biomass and soil water dynamics are not observed. Additional thoughts on data collection practices in areas of complex terrain are listed in section 5 of Ivanov et al. [2008]. Hopefully, model-driven projections and deeper insights can eventually stimulate model-oriented observational practices.

[13] In summary, the aim of this introductory paper is therefore (1) to develop a modeling system that incorporates state-of-the-art representation of vegetation-hydrology interactions in areas of complex terrain; (2) to illustrate mois-ture-dependent vegetation-hydrology linkages in semiarid zones; and (3) to demonstrate model performance and suitability for a semiarid environment using a variety of available data. Ivanov et al. [2008] employ the developed system to investigate topographic controls on vegetation temporal development and spatial distribution.

2. Model Overview

[14] The system couples a model of plant physiology and spatial dynamics Vegetation Generator for Interactive Evolution (VEGGIE) to the spatially distributed physically based hydrological model, the TIN-based Real-time Integrated Basin Simulator, tRIBS [Garrote and Bras, 1995; Tucker et al., 2001; Ivanov et al., 2004a, 2004b]. Most of the tRIBS hydrological components, however, have been modified in this work to more realistically represent vegetation, as discussed in the following. The modeling system was designed to be amenable to a variety of applications that may involve both exploratory topics of hydrology and ecohydrology as well as more practical issues related to operational hydrologic forecasting.

[15] The model simulates the energy and water budgets of both vegetated and nonvegetated surfaces that can be simultaneously present within a given element. In a domain of study, the dynamics of each computational element are simulated separately. Spatial dependencies are introduced by considering the surface and subsurface moisture transfers among the elements, which affect local dynamics via the coupled energy-water interactions. Consequently, when applied to a catchment system, the model offers a quasi-three-dimensional framework in which lateral moisture transfers may lead to the spatiotemporal variability of states. The model accounts for the hydraulic, thermal, and albedo properties of different soil types.

[16] The system simulates a number of processes that manifest numerous dynamic feedbacks among various components of the coupled vegetation-hydrology system: (1) biophysical energy processes such as absorption, reflection, and transmittance of solar shortwave radiation; absorption, reflection, and emission of longwave radiation; sensible, latent, and ground heat fluxes, partition of latent heat into canopy and soil evaporation, and transpiration; stomatal physiology; (2) biophysical hydrology processes such as interception, throughfall, and stem flow; infiltration in a multilayer soil; lateral water transfer in the vadose zone; runoff and run-on; and (3) biochemical processes and vegetation dynamics such as photosynthesis and primary productivity; plant respiration; tissue turnover and stress-induced foliage loss; carbon allocation; vegetation phenology; plant recruitment. While most models of biophysical processes operate at an hourly timescale, the routines simulating the processes of infiltration, lateral moisture transfer, and runoff (run-on) use a finer time step ($\sim$7.5–15 min). Consequently, at the hourly timescale, the stomatal response to environmental conditions is the only vegetation process that affects the water and energy budgets. At the daily and longer timescales, vegetation affects the land-surface state through the change of its structural attributes (e.g., leaf area index, height) and vegetation fraction. The latter determines the relative contribution of a given vegetation type to the element-scale fluxes. The equations

formulated in the following refer to the vegetation fraction scale only, unless otherwise is indicated.

[17] Certain characteristics of vegetation-hydrology linkages are not addressed in this work. Among these are that the aerodynamic resistance to the heat fluxes is parameterized only as a function of plant height and the amount of foliage biomass does not affect momentum transfer; a single skin soil temperature is estimated to represent both bare soil and under-canopy ground; the soil temperature profile is not explicitly computed; a single canopy temperature is estimated for the several vegetation types present within a given element; nutrient cycling is not accounted for; the assumed root distribution profile is static; seed production, dispersal, germination, seedling establishment, and plant mortality are not considered; no explicit effects of plant interaction and competition are accounted for.

3. Domain Representation

[18] Topography and drainage network of a domain of interest are represented using triangulated irregular network (TIN) of points in the manner discussed by *Vivoni et al.* [2004] and *Ivanov et al.* [2004a]. The reference system of the basic computational element, the Voronoi region, is defined by the axes p and n, where p follows the direction parallel to the plane of the maximum slope $\alpha_{\triangledown}$ (positive downslope) and n follows the direction normal to that plane (positive downward). The state variables of the one-dimensional mass flow equations, when applied to a Voronoi cell, are a function of the direction n. The surface and subsurface mass flux exchange between the contiguous elements is assumed to occur in the plane parallel to the direction p. The reader is referred to the above papers for details on the approach.

4. Vegetation Representation
4.1. Composition and Representation at the Element Scale

[19] The model operates with the concept of plant functional type (PFT). This concept allows combining of species with similar characteristics into the same groups [e.g., *Smith et al.*, 1997]. It is assumed that vegetated surfaces at the level of the basic computational element are composed of multiple PFTs (see *Bonan et al.* [2002]) that may differ in life form (e.g., tree, shrub, grass), vegetation physiology (e.g., leaf optical and photosynthetic properties), and structural attributes (e.g., height, leaf dimension, or root profile). A single element can thus contain a fraction of bare soil and, for instance, patches of deciduous forest and grass. Each patch, while co-occurring in the same Voronoi element, represents a separate column for which calculations of water and energy fluxes are performed. Accordingly, differences in plant properties strongly affect estimation of the surface fluxes. Water uptake properties of each PFT are controlled by the soil matric potentials Ψ^* and Ψ_w [MPa] at which, respectively, the stomatal closure and plant wilting begins. For a given soil type, these are translated into the relative soil moisture contents θ^* and θ_w [mm^3 mm^{-3}] that are used in parameterizing the stomatal resistance as a function of soil water in the root zone.

[20] The total number of PFTs that can be present within the same element is not limited, but may be restricted because of computational performance. Fractional areas that represent vegetated patches and bare soil are used to weight the relative contribution of each PFT/bare soil to the element-scale flux values. Vegetation composition and respective fractional areas are time-dependent (see section 9.8). The model assumes that plants do not explicitly compete for light and water, i.e., the respective spatial location of PFTs and the effects of shading are not explicitly considered. Instead, these effects are considered implicitly. Aboveground competition for light is treated as the competition for available space and is determined from PFT's success to produce biomass. Plant water uptake properties and the features of rooting profiles translate into PFT's differences in ability to access soil moisture and thus impose the competition for available water. Evidently, this form of interaction among PFTs is only applicable to ecosystems with sparse vegetation, where the effects of plant shading are minimal. A more comprehensive approach to representing the competition for light in densely vegetated areas would need to explicitly consider the vertical structure of vegetation organization. The model is, however, very flexible and could incorporate such an extension.

4.2. Structure, Carbon, and Nutrients

[21] Each vegetation type is represented by carbon compartments corresponding to leaves and fine roots. Additionally, in woody species, pools of living sapwood and dead structural wood are considered, the latter combines the components of both stem and coarse roots and includes bark, sapwood xylem, and heartwood. Given these carbon pools, vegetation structure is defined by a time-invariant root profile and leaf dimension and time-varying leaf area and canopy height (see section 9.8). The time-invariant vegetation properties are obtained from the literature. *Jackson et al.* [1996] provide a comprehensive study of the root distributions for a variety of species. *Bonan* [1995, 1996] provide typical values of leaf dimension (section 5.2 and Appendix A) for various plant types. The relative fine root fraction in a particular soil layer R_{root} [dimensionless] is calculated from an exponential root profile [*Jackson et al.*, 1996]:

$$R_{root}(n) = 1 - e^{-\eta n}, \qquad (1)$$

where n [mm] is soil depth taken in the direction normal to the surface and η [mm^{-1}] is the decay rate of distribution of the root biomass. This formulation allows one to adjust the profile, so that different vegetation types can have different root distributions.

[22] The time-varying vegetation characteristics are determined by using PFT-specific allometric relationships from the size of the carbon pools. The model development is tailored to arid and semiarid areas, where water constitutes the major limiting resource [e.g., *Scholes and Walker*, 1993, p. 110; *Rodriguez-Iturbe et al.*, 2001]. Nutrients are therefore not tracked in the vegetation compartments. Nonetheless, the model considers the maximum catalytic capacity of Rubisco, a nitrogen containing enzyme in leaves, catalyzing carbon fixation. It is assumed that the capacity exhibits a vertical decay throughout the canopy. This nutrient-related consideration is used to adjust the rates

of photosynthesis experienced by a PFT at various stages of growth.

5.   Surface Albedos

[23] Two types of surfaces are considered within a computational element: ground and canopy. The ground surface can be present as both bare soil and under-canopy soil. Ground albedos are parameterized on the basis of the soil surface moisture content. The reflectance properties of the canopy depend on both the biophysical properties of the vegetation type as well as the characteristics of incident shortwave radiation.

5.1.   Ground Albedos

[24] The overall direct beam $\alpha_{g\Lambda}^{\mu}$ and diffuse $\alpha_{g\Lambda}$ [dimensionless] ground albedos depend on soil color class and moisture content at the soil surface [*Dickinson et al.*, 1993]:

$$\alpha_{g\Lambda}^{\mu} = \alpha_{g\Lambda} = (\alpha_{sat\,\Lambda} + \Delta) \ \leq \ \alpha_{dry\,\Lambda}, \qquad (2)$$

where Δ [dimensionless] depends on the volumetric water content θ_1 [mm^3 mm^{-3}] of the soil surface (see section 8.2) as $\Delta = (0.11 - 0.40\,\theta_1) > 0$, $\alpha_{sat\Lambda}$ and $\alpha_{dry\Lambda}$ [dimensionless] are the albedos for saturated and dry soil color classes [*Dickinson et al.*, 1993]. The Λ symbol refers to differentiation between the two considered wavelength bands: visible [0.29–0.70 μm] (VIS) and near-infrared [0.70–4.0 μm] (NIR). The μ symbol denotes quantities corresponding to the direct beam (directional) incident radiation. As seen above, the ground albedos are assumed to be independent of the type of incident radiation but can be different for different wave bands.

5.2.   Canopy Radiative Transfer

[25] Radiative transfer within vegetative canopies is calculated from the two-stream approximation of *Dickinson* [1983] and *Sellers* [1985]. The formulation has been described in detail previously [e.g., *Sellers et al.*, 1996a; *Bonan*, 1996; *Oleson et al.*, 2004]. In summary, the approach estimates canopy radiative properties based on leaf and stem characteristics, type, and state of the canopy and plant woody components. Characteristics considered are the leaf and stem reflectances and transmittances for VIS and NIR wave bands of incident radiation, leaf average dimensions, leaf average spatial orientation, and leaf and stem areas. The model differentiates between direct beam (accounting for the incidence angle) and diffuse radiation to calculate the fractions of diffuse fluxes (per unit incident flux) leaving the top of canopy, $I\uparrow_{\Lambda}^{\mu}$ and $I\uparrow_{\Lambda}$, and the base of canopy, $I\downarrow_{\Lambda}^{\mu}$ and $I\downarrow_{\Lambda}$.

6.   Radiative Fluxes

[26] For a vegetated surface, the net radiation is estimated at two levels. At the canopy level, the net radiation is $R_{nv} = \vec{S}_v + \vec{L}_v$, and at the ground level, $R_{ng} = \vec{S}_g + \vec{L}_g$, where $\vec{S}$ and $\vec{L}$ [W m^{-2}] are the net shortwave and longwave fluxes absorbed by the vegetation ("v") and ground ("g"). At the canopy level, the net radiation R_{nv} is partitioned into sensible heat H_v and latent heat λE_v fluxes [W m^{-2}]. At the ground level, R_{ng} is partitioned into sensible heat H_g,

latent heat λE_g, and ground heat G fluxes. If no vegetation is present, only the ground level fluxes are estimated. The formulation below follows that of *Bonan* [1996] and *Oleson et al.* [2004] for the most part.

6.1.   Shortwave Solar Fluxes

[27] At the vegetation patch scale, solar radiation is conserved as

$$\sum_{\Lambda} \left[S_{atm}\downarrow_{\Lambda}^{\mu} + S_{atm}\downarrow_{\Lambda} \right] = \vec{S}_v + \vec{S}_g$$
$$+ \sum_{\Lambda} \left[S_{atm}\downarrow_{\Lambda}^{\mu} I\uparrow_{\Lambda}^{\mu} + S_{atm}\downarrow_{\Lambda} I\uparrow_{\Lambda} \right], \quad (3)$$

where $S_{atm}\downarrow_{\Lambda}^{\mu}$ and $S_{atm}\downarrow_{\Lambda}$ [W m^{-2}] are the incident direct beam and diffuse solar fluxes provided as input, $I\uparrow_{\Lambda}^{\mu}$ and $I\uparrow_{\Lambda}$ [dimensionless] are the upward diffuse fluxes per unit incident direct beam and diffuse flux. The summation term on the right side is the total solar radiation reflected by the canopy or bare soil, which is accounted for by the fractions $I\uparrow_{\Lambda}^{\mu}$ and $I\uparrow_{\Lambda}$.

6.1.1.   Nonvegetated Surface

[28] The total solar radiation absorbed by bare soil is

$$\vec{S}_g^{bare} = \sum_{\Lambda} \left[S_{atm}\downarrow_{\Lambda}^{\mu} \left(1 - \alpha_{g\Lambda}^{\mu} \right) + S_{atm}\downarrow_{\Lambda} \left(1 - \alpha_{g\Lambda} \right) \right]. \quad (4)$$

Consequently, using the notation of (3), $\vec{S}_g = \vec{S}_g^{bare}$, $\vec{S}_v = 0$, $I\uparrow_{\Lambda}^{\mu} = \alpha_{g\Lambda}^{\mu}$, and $I\uparrow_{\Lambda} = \alpha_{g\Lambda}$.

6.1.2.   Vegetated Surface

[29] With reference to Figure 1a, the direct beam flux transmitted through the canopy per unit incident flux is $e^{-K(L+S)}$ and the direct beam and diffuse fluxes absorbed by the vegetation per unit incident flux are

$$\vec{I}_{\Lambda}^{\mu} = 1 - I\uparrow_{\Lambda}^{\mu} - (1 - \alpha_{g\Lambda})I\downarrow_{\Lambda}^{\mu} - \left(1 - \alpha_{g\Lambda}^{\mu} \right)e^{-K(L+S)}, \quad (5)$$

$$\vec{I}_{\Lambda} = 1 - I\uparrow_{\Lambda} - (1 - \alpha_{g\Lambda})I\downarrow_{\Lambda}, \quad (6)$$

where L [m^2 leaf area m^{-2} ground area] is the total one-sided leaf area index and S [m^2 stem area m^{-2} ground area] is the total stem area index, and $I\downarrow_{\Lambda}^{\mu}$ and $I\downarrow_{\Lambda}$ [dimensionless] are the downward diffuse fluxes per unit incident direct beam and diffuse radiation, and K [dimensionless] is the optical depth of direct beam per unit leaf and stem area [*Dickinson*, 1983]. The total radiation absorbed by vegetation $\vec{S}_v^{veg}$ and understory ground $\vec{S}_g^{veg}$ [W m^{-2}] are

$$\vec{S}_v^{veg} = \sum_{\Lambda} \left[S_{atm}\downarrow_{\Lambda}^{\mu} \vec{I}_{\Lambda}^{\mu} + S_{atm}\downarrow_{\Lambda} \vec{I}_{\Lambda} \right], \quad (7)$$

$$\vec{S}_g^{veg} = \sum_{\Lambda} \left[S_{atm}\downarrow_{\Lambda}^{\mu} e^{-K(L+S)} \left(1 - \alpha_{g\Lambda}^{\mu} \right) \right.$$
$$\left. + \left(S_{atm}\downarrow_{\Lambda}^{\mu} I\downarrow_{\Lambda}^{\mu} + S_{atm}\downarrow_{\Lambda} I\downarrow_{\Lambda} \right)\left(1 - \alpha_{g\Lambda} \right) \right]. \quad (8)$$

Using the notation of (3), for a given vegetation patch $\vec{S}_v = \vec{S}_v^{veg}$ and $\vec{S}_g = \vec{S}_g^{veg}$.
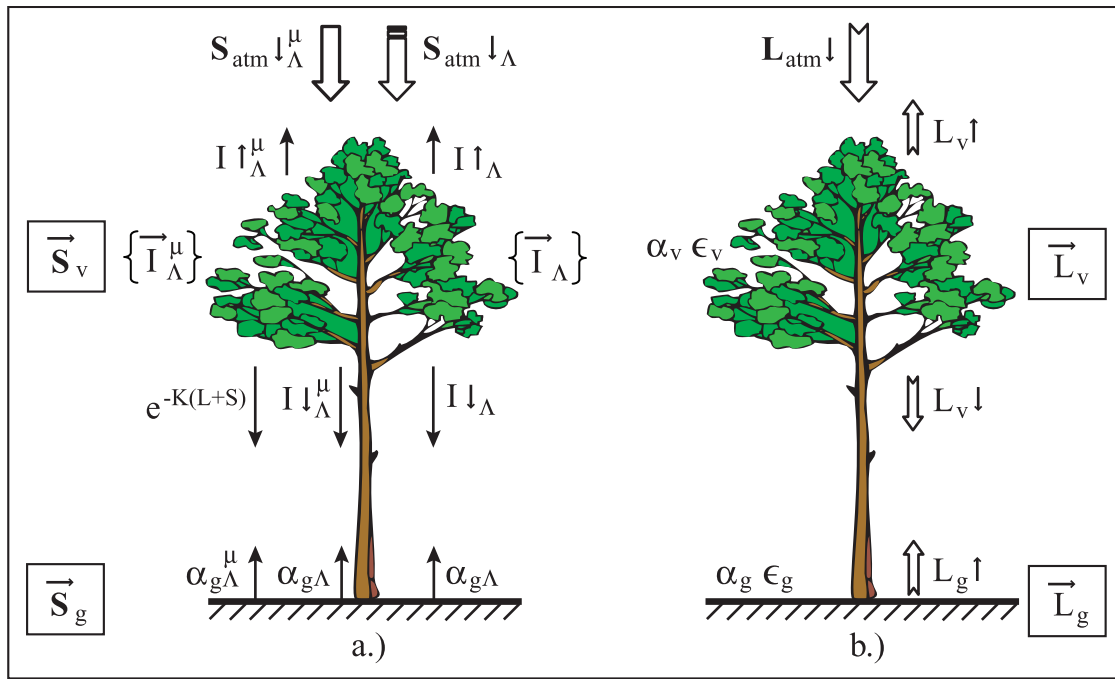
Figure 1. A schematic diagram of shortwave and longwave radiation fluxes: (a) direct beam (left-hand side of the plant) and diffuse (right-hand side of the plant) solar radiation absorbed, transmitted, and reflected by vegetation and under-canopy ground; $S_{atm}\downarrow_\Lambda^\mu$ and $S_{atm}\downarrow_\Lambda$ are the incident direct beam and diffuse shortwave fluxes provided as input; $e^{-K(L+S)}$ is the fraction of direct beam flux transmitted through the canopy; $I\uparrow_\Lambda^\mu$ and $I\downarrow_\Lambda^\mu$ are the upward and downward diffuse fluxes per unit incident direct beam radiation; $I\uparrow_\Lambda$ and $I\downarrow_\Lambda$ are the upward and downward diffuse fluxes per unit incident diffuse radiation; $\alpha_{g\Lambda}^\mu$ and $\alpha_{g\Lambda}$ are the ground albedos for direct beam and diffuse radiation; $\vec{I}_\Lambda^\mu$ and $\vec{I}_\Lambda$ are the fractions of incident direct beam and diffuse fluxes absorbed by the vegetation; $\vec{S}_v^{veg}$ and $\vec{S}_g^{veg}$ are the total solar radiation energy absorbed by vegetation and understory ground. (b) Longwave radiation absorbed, transmitted, reflected, and emitted by vegetation and under-canopy ground; $L_{atm}\downarrow$ is the downward atmospheric longwave radiation provided as input; $L_v\uparrow$ and $L_v\downarrow$ are the upward/downward longwave radiation fluxes above/below the vegetation canopy; $L_g\uparrow$ is the upward longwave radiation from the ground; $\vec{L}_v$ and $\vec{L}_g$ are the net longwave radiation energy for canopy and understory ground; ϵ_v and ϵ_g are the vegetation and ground emissivities; α_v and α_g are the vegetation and ground absorptivities.

[30] The visible and near-infrared reflectances r_{vis} and r_{nir} [dimensionless] are estimated as

$$r_\Lambda = \frac{S_{atm}\downarrow_\Lambda^\mu I\uparrow_\Lambda^\mu + S_{atm}\downarrow_\Lambda I\uparrow_\Lambda}{S_{atm}\downarrow_\Lambda^\mu + S_{atm}\downarrow_\Lambda} \qquad (9)$$

They are used to calculate the normalized difference vegetation index (NDVI) for a given vegetation patch as NDVI = $(r_{nir} - r_{vis})/(r_{nir} + r_{vis})$.

6.1.3. Canopy Fractions

[31] Canopy photosynthesis models are generally formulated to describe the fluxes of both CO_2 and water vapor at the leaf level. Multilayer and "big-leaf" approaches have been used for scaling these quantities to the canopy level [*Dai et al.*, 2004]. A multilayer model integrates the fluxes from each canopy layer to give the total flux [e.g., *Wang and Jarvis*, 1990; *Leuning*, 1995], while the big-leaf approach maps properties of the whole canopy onto a single leaf [e.g., *Sellers et al.*, 1996a]. Multilayer models use parameters that are measured at the leaf level, while big-leaf models require an assumption about the vertical profile of leaf properties. An often used hypothesis assumes that the limiting rate of carbon uptake varies with canopy depth in the same manner as the time-mean profile of photosynthetically active radiation (PAR) [e.g., *Sellers et al.*, 1992]. However, as argued by *Norman* [1993], *de Pury and Farquhar* [1997], and *Wang and Leuning* [1998], it is theoretically incorrect to ignore the instantaneous distribution of radiation in the canopy due to strong nonlinearities in the leaf biochemical processes that depend on PAR and leaf temperature. For instance, the photosynthesis of shaded leaves has an essentially linear response to absorbed PAR, while photosynthesis of sunlit leaves is often light saturated. Direct sunshine may heat sunlit leaves several degrees warmer than shaded leaves.

[32] *Wang and Leuning* [1998] have demonstrated that the two-leaf approach, i.e., the one that divides canopy into sunlit and shaded leaves, leads to assimilation rates and energy/water fluxes comparable to those of a multilayer model. Averaging PAR in each of these leaf classes is appropriate and introduces little error in the predicted canopy photosynthesis [*Dai et al.*, 2004]. *Dai et al.* [2004] also compared schemes that estimate either two temperatures (for sunlit and shaded fractions) or a single temperature for the entire canopy. The latter approach led to either an overestimation, for a tropical rain forest, or

underestimation, for a boreal conifer forest, of the canopy CO_2 and water fluxes, while "...the underlying causes are unknown" [*Dai et al.*, 2004, p. 2292]. Since the estimation of separate canopy temperatures results in an extremely high computational overhead due to the highly nonlinear coupling between the energy budget and the photosynthesis/ stomatal conductance models, the same leaf temperature is computed for both layers in the present model, similar to *Bonan* [1996] and *Dickinson et al.* [1998]. The separate treatment of the assimilation rates and stomatal conductances for sunlit and shaded leaves is assumed to be sufficient to account for the principal differences between the two canopy layers.

[33] The canopy sunlit fraction f_{sun} [dimensionless] is estimated following *Bonan* [1996] and *Oleson et al.* [2004], assuming that penetration of direct beam radiation in the canopy decays exponentially, controlled by the light extinction parameter K' [*Monsi and Saeki*, 2005]:

$$f_{sun} = \frac{1}{(L+S)} \int_0^{L+S} e^{-K'x}dx = \frac{1}{(L+S)} \frac{1-e^{-K'(L+S)}}{K'}, \quad (10)$$

where $e^{-K'(L+S)}$ is the fractional area of the direct beam radiation on a horizontal plane below $(L+S)$. The shaded fraction is $f_{shd} = 1 - f_{sun}$ and the sunlit and shaded leaf area indices are $L_{sun} = f_{sun}L$ and $L_{shd} = f_{shd}L$. In estimating f_{sun}, the parameter K' accounts for scattering in the canopy due to its geometry and beam incidence angle [*Sellers*, 1985].

[34] The solar radiation absorbed by the vegetation biomass in the visible wave band [0.29–0.70 μm] is partitioned into sunlit and shaded leaves to calculate the average absorbed PAR for sunlit, ϕ_{sun}, and shaded, ϕ_{shd} [W m^{-2}], leaves for a given hour. For $f_{sun} > 0$,

$$\phi^{sun} = \left(S_{atm}\downarrow_{vis}^{\mu}\vec{I}_{vis}^{\mu} + f_{sun}S_{atm}\downarrow_{vis}\vec{I}_{vis}\right)\frac{L}{L+S}, \quad (11)$$

$$\phi^{shd} = \left(f_{shd}S_{atm}\downarrow_{vis}\vec{I}_{vis}\right)\frac{L}{L+S}. \quad (12)$$

Absorbed radiation, ϕ_{sun} and ϕ_{shd} [W m^{-2}], is used in the estimation of photosynthesis and stomatal resistance (see section 9.1). The above equations assume the sunlit leaves absorb all the direct beam radiation, that all leaves absorb diffuse radiation (according to the fractions f_{sun} and f_{shd}), and that leaves absorb $L/(L+S)$ of the radiation absorbed by vegetation. If $f_{sun} = 0$, e.g., significant cloudiness with zero incident direct beam flux, all radiation is absorbed by the shaded leaves.

6.2. Longwave Fluxes

[35] The net longwave radiation for a surface (positive values correspond to radiation energy moving away from surface) is

$$\vec{L} = -L\downarrow + L\uparrow, \quad (13)$$

where $L\downarrow$ and $L\uparrow$ [W m^{-2}] are the downward and upward longwave radiation components. The energy emitted by a radiating surface [*Bras*, 1990] is $L\uparrow = \sigma T_{rad}^4$, where T_{rad} [K] is the radiative temperature and $\sigma = 5.6704 \times 10^{-8}$ [W m^{-2} K^{-4}] is the Stefan-Boltzmann constant.

6.2.1. Nonvegetated Surface

[36] For nonvegetated surfaces, formulation (13) for the net longwave radiation takes the form

$$\vec{L}_g^{bare} = -\alpha_g L_{atm}\downarrow + \epsilon_g \sigma T_g^4, \quad (14)$$

where $L_{atm}\downarrow$ [W m^{-2}] is the downward atmospheric longwave radiation, α_g [dimensionless] is the ground absorptivity, ϵ_g [dimensionless] is the ground emissivity, and T_g [K] is the ground temperature (section 7).

6.2.2. Vegetated Surface

[37] Using formulation (13) and with reference to Figure 1b, the net longwave radiation energy for canopy $\vec{L}_v^{veg}$ and ground under the canopy $\vec{L}_g^{veg}$ [*Bonan*, 1996] is

$$\begin{aligned}\vec{L}_v^{veg} &= \left(L_v^{veg}\downarrow - L_{atm}\downarrow\right) + \left(L_v^{veg}\uparrow - L_g^{veg}\uparrow\right) \\ &= -\alpha_v\left[1 + (1-\alpha_v)(1-\alpha_g)\right]L_{atm}\downarrow \\ &\quad - \alpha_v\epsilon_g\sigma T_g^4 + \epsilon_v\sigma\left[2 - \alpha_v(1-\alpha_g)\right]T_v^4,\end{aligned} \quad (15)$$

$$\begin{aligned}\vec{L}_g^{veg} &= \left(L_g^{veg}\uparrow - L_v^{veg}\downarrow\right) \\ &= -\alpha_g(1-\alpha_v)L_{atm}\downarrow - \alpha_g\epsilon_v\sigma T_v^4 + \epsilon_g\sigma T_g^4,\end{aligned} \quad (16)$$

where $L_v^{veg}\downarrow$ and $L_v^{veg}\uparrow$ are the downward/upward longwave radiation fluxes below/above canopy, respectively, and $L_g^{veg}\uparrow$ is the upward longwave radiation from the ground:

$$\begin{aligned}L_v^{veg}\downarrow &= (1-\alpha_v)L_{atm}\downarrow + \epsilon_v\sigma T_v^4, \\ L_g^{veg}\uparrow &= (1-\alpha_g)L_v^{veg}\downarrow + \epsilon_g\sigma T_g^4, \\ L_v^{veg}\uparrow &= (1-\alpha_v)L_g^{veg}\uparrow + \epsilon_v\sigma T_v^4.\end{aligned} \quad (17)$$

T_v and T_g [K] are the vegetation and ground temperatures (section 7), α_v and α_g [dimensionless] are the absorptivities, and ϵ_v and ϵ_g [dimensionless] are the emissivities: $\epsilon_g = 0.96$, $\epsilon_v = 1 - e^{-(L+S)}$ [*Bonan*, 1996]. The latter relationship accounts for an increase in canopy emissivity with the amount of foliage biomass [e.g., *Francois et al.*, 1997].

6.3. Sensible and Latent Heat Fluxes

[38] The parameterization of the sensible and latent heat fluxes employs a "resistance" formulation [e.g., *Shuttleworth*, 1979; *Bras*, 1990; *Arya*, 2001, p. 369]. The resistances have dimensions of inverse of velocity and depend on many factors including surface roughness (e.g., canopy structure and leaf dimensions), wind speed, and atmospheric stability.

6.3.1. Nonvegetated Surface

[39] For bare soil, the sensible heat H_g^{bare} and the latent heat λE_g^{bare} [W m^{-2}] fluxes between the atmosphere at a reference height z_{atm} [m] and the soil surface are estimated as

$$H_g^{bare} = -\rho_{atm}C_p\frac{(T_{atm} - T_g)}{r_s^h}, \quad (18)$$

$$\lambda E_g^{bare} = -\rho_{atm}\frac{C_p}{\gamma}\frac{(e_{atm} - e^*(T_g)h_{soil})}{r_s^w}, \quad (19)$$

where the following variables are defined at elevation z_{atm}: the air temperature T_{atm} [K], the density of moist air ρ_{atm} [kg m^{-3}], and the vapor pressure e_{atm} [hPa]. The ground "skin" temperature T_g [K] and the saturated vapor pressure in soil pores $e^*(T_g)$ [hPa] are defined at the ground surface level. $C_p = 1013$ [J kg^{-1} K^{-1}] is the air heat capacity, λ [J kg^{-1}] is the latent heat of vaporization, γ [hPa K^{-1}] is the psychrometric constant, r_s^h and r_s^w [s m^{-1}] are the total resistances to the sensible and latent heat flux, respectively, and h_{soil} [dimensionless] is the relative humidity of the soil pore space [Philip, 1957]:

$$h_{soil} = e^{\frac{\psi_1 g}{R_w T_g}}, \text{ if } e^*(T_g) \geq e_{atm}, \qquad (20)$$

$$h_{soil} = 1, \quad \text{if } e^*(T_g) < e_{atm}, \qquad (21)$$

where ψ_1 [m] is the soil moisture potential of the topsoil layer (first 12 mm, see section 8.2), $g = 9.8$ [m s^{-2}] is the acceleration due to gravity, and $R_w = 461.5$ [J kg^{-1} K^{-1}] is the gas constant for water vapor.

[40] Assuming a simple linear combination of resistances for the sensible and latent heat fluxes [e.g., Arya, 2001; Taiz and Zeiger, 2002]: $r_s^h = r_{ah}$ and $r_s^w = r_{aw} + r_{srf}$, where r_{ah} and r_{aw} [s m^{-1}] are the bulk resistances to sensible heat and water vapor fluxes between the ground surface and the atmosphere and r_{srf} [s m^{-1}] is the soil surface resistance, an empirical factor that is intended to take into account the impedance of the soil pores to exchanges of water vapor between the first soil layer and the immediately overlying air. Following Sellers et al. [1996a],

$$r_{srf} = e^{8.206 - 4.255 \, \beta_E^w}, \qquad (22)$$

where $\beta_E^w \leq 1$ is given by Bonan [1996] and Cox et al. [1999]:

$$\beta_E^w = \frac{\theta_1 - \theta_r}{a' \theta_s - \theta_r},$$

where θ_1 [mm^3 mm^{-3}] is the soil surface water content (first 12 mm, section 8.2), θ_s and θ_r [mm^3 mm^{-3}] are the saturation and residual soil moisture contents (section 8.3) and a' is assumed to be 0.75 to approximately relate to the soil moisture content at field capacity.

[41] Since atmospheric conditions vary, the dominant mechanisms involved in transfer of the heat fluxes away from the ground surface can differ. Highly turbulent, windy conditions lead to forced convection, and r_{ah} and r_{aw} in (18)–(19) thus represent the aerodynamic resistances between the atmosphere at reference height z_{atm} and the heights $z_{0h} + d$ and $z_{0w} + d$ [m], corresponding to the apparent sinks for heat and water vapor, respectively [Shuttleworth, 1979]. Under assumed neutral atmospheric conditions:

$$r_{ah} = \frac{1}{\kappa^2 u_{atm}} \ln\left(\frac{z_{atm} - d}{z_{0m}}\right) \ln\left(\frac{z_{atm} - d}{z_{0h}}\right), \qquad (23)$$

$$r_{aw} = \frac{1}{\kappa^2 u_{atm}} \ln\left(\frac{z_{atm} - d}{z_{0m}}\right) \ln\left(\frac{z_{atm} - d}{z_{0w}}\right), \qquad (24)$$

where $\kappa = 0.41$ is the von Karman constant, u_{atm} [m s^{-1}] is the wind speed at z_{atm} (typically, $z_{atm} = 2$ m), d [m] is the zero plane displacement, $z_{0m} + d$ [m] is the height corresponding to the apparent sink for momentum. For bare soil: $d = 0$, $z_{0m} = 0.05$ m, $z_{0h} = z_{0w} = 0.1 z_{0m}$.

[42] In calm, windless conditions, free convection is the dominant heat transfer mechanism. An empirical approach of Kondo and Ishida [1997] is used here for $u_{atm} < 1.0$ m s^{-1} to parameterize r_{ah} and r_{aw} as the reciprocal of an empirically obtained bulk transfer coefficient:

$$r_{ah} = \frac{1}{b' \Delta T_V^{\frac{1}{3}}} = \frac{1}{b'} \left[(T_g - T_{atm}) + 0.11 \left(e^*(T_g) h_{soil} - e_{atm} \right) \right]^{-\frac{1}{3}}, \qquad (25)$$

and $r_{aw} = r_{ah}$. Equation (25) assumes that with no wind, the virtual temperature difference ΔT_V [K] creates natural convection. In experiments of Kondo and Ishida [1997] the value of b' is determined empirically and for rough surfaces is assumed to be $b' = 0.0038$ m s^{-1} K$^{-1/3}$.

6.3.2. Vegetated Surface

[43] For a vegetated surface, the sensible and latent heat fluxes are partitioned into vegetation and ground (under-canopy) fluxes that depend on vegetation T_v and ground T_g [K] temperatures. Assuming the canopy air does not store heat, the sensible heat flux between the surface at height $z_{0h} + d$ and the atmosphere at height z_{atm} is partitioned into independent vegetation canopy and under-canopy fluxes, $H^{veg} = H_v^{veg} + H_g^{veg}$,

$$H_v^{veg} = -\rho_{atm} C_p \frac{(T_s - T_v)}{r_v^h}, \qquad (26)$$

$$H_g^{veg} = -\rho_{atm} C_p \frac{(T_{atm} - T_g)}{r_s^h}, \qquad (27)$$

where T_s [K] is the canopy space temperature at height $z_{0h} + d$, r_v^h and r_s^h [s m^{-1}] are the bulk resistances to sensible heat flux between the vegetation/ground surface and the atmosphere.

[44] Assuming that the canopy air does not store water vapor, the latent heat flux is partitioned into independent vegetation and ground fluxes, $\lambda E^{veg} = \lambda E_v^{veg} + \lambda E_g^{veg}$,

$$\lambda E_v^{veg} = -\frac{\rho_{atm} C_p}{\gamma} \frac{(e_s - e^*(T_v))}{r_v^w}, \qquad (28)$$

$$\lambda E_g^{veg} = -\frac{\rho_{atm} C_p}{\gamma} \frac{(e_{atm} - e^*(T_g) h_{soil})}{r_s^w}, \qquad (29)$$

where e_s [hPa] is the vapor pressure of canopy space at height $z_{0h} + d$, r_v^w and r_s^w [s m^{-1}] are the bulk resistances to the flux between the vegetation or ground surface and the atmosphere.

[45] Resistances used in equations (26)–(27) and (28)–(29) can be expressed as $r_v^h = 1/c_v^h$, $r_s^h = 1/c_s^h$, $r_v^w = 1/(c_e^w + c_t^w)$, and $r_s^w = 1/c_s^w$. As above, the formulation of resistances depends on the dominant heat transfer mechanism. For the

conditions of forced convection, the conductances c_a^h, c_a^w, c_v^h, c_s^h, c_e^w, c_t^w, and c_s^w [m s^{-1}] are defined in Appendix A. Note that the soil moisture state affects the latent heat flux through stomatal resistances, which are estimated by accounting for the soil moisture distribution in the root zone (section 8.2).

[46] The expressions for T_s in (26)–(27) and e_s in (28)–(29) are derived from the assumed equality of fluxes among different canopy levels. Note that the ground and canopy heat fluxes are assumed to be independent (for details, see *Ivanov* [2006]), which is different from the formulation of *Bonan* [1996] and *Oleson et al.* [2004]. In semiarid conditions, the latter scheme exhibits an excessively strong sensitivity of canopy energy partition on under-canopy energy fluxes (e.g., a strong decrease of transpiration due to the reduction in under-canopy soil latent heat flux). The flux equality leads to

$$-\rho_{atm}C_p(T_{atm}-T_s)\frac{1}{r_{ah}} = -\rho_{atm}C_p(T_s-T_v)\frac{2(L+S)}{r_b}, \quad (30)$$

$$-\frac{\rho_{atm}C_p}{\gamma}\frac{(e_{atm}-e_s)}{r_{aw}} = -\frac{\rho_{atm}C_p}{\gamma}\frac{(e_s-e^*(T_v))}{r_b+r_s}, \quad (31)$$

from which one can obtain

$$T_s = \frac{c_a^h T_{atm} + c_v^h T_v}{c_a^h + c_v^h}, \quad (32)$$

$$e_s = \frac{c_a^w e_{atm} + (c_e^w + c_t^w)e^*(T_v)}{c_a^w + c_e^w + c_t^w}. \quad (33)$$

[47] In calm, windless conditions, free convection is the dominant mechanism of heat transfer away from vegetated areas. For $u_{atm} < 1.0$ m s^{-1}, an empirical approach of *Kondo and Ishida* [1997] is used to parameterize the resistances as functions of empirically obtained bulk transfer coefficients (Appendix A). For free convection conditions, $T_s = T_{atm}$ and $e_s = e_{atm}$.

6.4. Ground Heat Flux and Soil Temperature

[48] Ground heat flux is an important component of the surface energy balance, particularly in semiarid areas. Since no analytical formulation is available for heat flux for arbitrary boundary conditions, approximate methods are typically used. This model employs the method of *Wang and Bras* [1999], based on the one-dimensional heat diffusion equation with a constant diffusivity parameter. By relating the soil surface temperature to the ground heat flux through a half-order derivative/integral operator, *Wang and Bras* [1999] give

$$G(t) = \sqrt{\frac{k_s C_s}{\pi}}\int_0^t \frac{dT_g(s)}{\sqrt{t-s}}, \quad (34)$$

where $G(t)$ [W m^{-2}] is the ground heat flux at time t, k_s [J m^{-1} s^{-1} K^{-1}] is the volumetric heat conductivity, C_s [J m^{-3} K^{-1}] is the heat capacity of the soil, and s is the integration variable; k_s and C_s are well documented

parameters for a variety of common soils [e.g., *De Vries*, 1963]. Both k_s and C_s depend on the soil moisture state. From *Farouki* [1981],

$$k_s = K_e k_{s,sat} + (1-K_e)k_{s,dry}, \text{ if } \theta_d/\theta_s > 10^{-7}, \quad (35)$$

$$k_s = k_{s,dry}, \quad \text{if } \theta_d/\theta_s \leq 10^{-7}, \quad (36)$$

where $k_{s,dry}$ and $k_{s,sat}$ are the dry and saturated soil thermal conductivities, θ_s [mm^3 mm^{-3}] is the saturation moisture content and θ_d is the soil moisture over depth z_d [m], and K_e [dimensionless] is the Kersten number, which is a function of the relative saturation: $K_e = \ln(\theta_d/\theta_s) + 1 \geq 0$. In this work, the depth z_d corresponds to the top 12 mm of the soil column, which is the integration depth of the first node in the finite element mesh representing the column (section 8.2). The soil heat capacity is estimated as a function of soil moisture as

$$C_s = C_{s,soi}(1-\theta_s) + \theta_d C_{liq}, \quad (37)$$

where $C_{s,soi}$ [J m^{-3} K^{-1}] is the heat capacity of the soil solid [*De Vries*, 1963] and $C_{liq} = 4.188 \times 10^6$ [J m^{-3} K^{-1}] is the specific heat capacity of water.

[49] The variable T_g represents the "skin" soil temperature. It is also important to compute the soil temperature T_{soil} [K] averaged over a certain depth, e.g., root zone. To avoid additional computational overhead, it is assumed that T_{soil} can be computed approximately using available information on T_g. Two principal features need to be represented in the dynamics of T_{soil}: (1) the smaller diurnal variability and absolute magnitudes with respect to T_g, which mimics dampening with depth; and (2) the seasonal phases of gradual soil warming and cooling that reflect average conditions for soil biochemical and biophysical processes. To ensure the above characteristics, the moving average of surface temperatures is used as a surrogate estimate of T_{soil} (with averaging interval of 10 to 36 h).

6.5. Element-Scale Quantities

[50] Any variable estimated separately for vegetated and bare soil fractions of a given element can be expressed as a quantity at the element scale. A linear combination of the relative contributions from all PFTs and bare soil present in the element is assumed for all calculations at the element scale. For instance, the element-scale quantity of NDVI, previously estimated at the scale of a given PFT, can be obtained as

$$\overline{NDVI} = \frac{\bar{r}_{nir} - \bar{r}_{vis}}{\bar{r}_{nir} + \bar{r}_{vis}},$$

where

$$\bar{r}_\Lambda = \frac{S_{v,\Lambda}\uparrow + S_{g,\Lambda}\uparrow}{S_{atm}\downarrow_\Lambda^\mu + S_{atm}\downarrow_\Lambda}, \quad (38)$$

$$S_{v,\Lambda}\uparrow = \sum_k^{N_V}\left(S_{atm}\downarrow_\Lambda^\mu I\uparrow_{k,\Lambda}^\mu + S_{atm}\downarrow_\Lambda I\uparrow_{k,\Lambda}\right)f_{v,k}, \quad (39)$$

$$S_{g,\Lambda}\uparrow = \left(\alpha_{g,\Lambda}^\mu S_{atm}\downarrow_\Lambda^\mu + \alpha_{g,\Lambda}S_{atm}\downarrow_\Lambda\right)\left(1 - \sum_k^{N_V}f_{v,k}\right), \quad (40)$$

where $f_{v,k}$ [dimensionless] is the vegetation fraction of the kth plant functional type present in a given element, and N_V is the total number of plant functional types present in the element. The element-scale quantities are useful for model confirmation/calibration, e.g., $\overline{NDVI}$ can be used to relate the model output to observations from remote sensing platforms.

7. Net Radiation

[51] The net radiation for computational elements composed of bare soil only is expressed as

$$R_{ng} = \vec{S}_g^{bare} - \vec{L}_g^{bare} = H_g^{bare} + \lambda E_g^{bare} + G. \quad (41)$$

If vegetation is present, two levels are considered: the canopy and the ground level. At the canopy level, the net radiation is composed of the total vegetated part of the element by linearly combining the contributions from all PFTs:

$$R_{nv} = \sum_k^{N_V} \left(\vec{S}_{v,k}^{veg} - \vec{L}_{v,k}^{veg} \right) f_{v,k} = \sum_k^{N_V} \left(H_{v,k}^{veg} + \lambda E_{v,k}^{veg} \right) f_{v,k}. \quad (42)$$

[52] The same approach is used for estimating the ground level net radiation: the contributions from all PFTs are lumped together with the contributions from the fraction of bare soil:

$$
\begin{aligned}
R_{ng} &= \sum_k^{N_V} \left(\vec{S}_{g,k}^{veg} - \vec{L}_{g,k}^{veg} \right) f_{v,k} + \left(1 - \sum_k^{N_V} f_{v,k} \right) \left(\vec{S}_g^{bare} - \vec{L}_g^{bare} \right) \\
&= \sum_k^{N_V} \left(H_{g,k}^{veg} + \lambda E_{g,k}^{veg} \right) f_{v,k} \\
&\quad + \left(1 - \sum_k^{N_V} f_{v,k} \right) \left(H_g^{bare} + \lambda E_g^{bare} \right) + G \quad (43)
\end{aligned}
$$

While the separate treatment of each plant type would allow the differentiation between individual responses of energy budgets to water-radiation conditions at a given location, the above approach lumps PFT contributions together, thus attempting to avoid the additional computational expense. Ultimately, the model aims to address the spatial heterogeneity of hydrology-vegetation dynamics within a complex terrain. Site-specific characteristics such as geometry, location in the landscape, and soil properties should lead to inherently distinct regimes of radiation, soil moisture, and, therefore, spatial differences in vegetation dynamics.

[53] The formulation of net radiation in (41), (42), and (43) depends on the ground temperature T_g and, if vegetation is present, the vegetation temperature T_v. Both T_g and T_v are the state variables that have to be estimated iteratively since (41)–(43) are highly nonlinear equations and analytical solutions are not available. In general, the Newton-Raphson iteration method is used to simultaneously solve for the T_v and T_g that balance the vegetation and ground

surface energy budgets. More details on the implementation are given by *Ivanov* [2006].

8. Moisture Fluxes

[54] The model parameterizes the processes of canopy interception, drainage, throughfall, evapotranspiration, infiltration, surface runoff and run-on, and lateral subsurface moisture transfer. The moisture fluxes strongly depend on the energy partition in a computational element since the latent heat flux determines the amount of water extracted from or added to the system. In addition, the moisture state of the canopy and soil affects the energy budget by modulating the amount of absorbed radiation, the partition of latent heat, and the magnitude of ground heat flux. A strongly coupled system of water-energy interactions is thus represented.

8.1. Interception and Canopy Moisture Fluxes

[55] Precipitation is either intercepted by the canopy or falls to the ground as throughfall and stem flow. Interception is estimated from the *Rutter et al.* [1971, 1975] and *Eltahir and Bras* [1993] canopy water balance model:

$$\frac{dC}{dt} = (1 - p)R - D - \frac{C}{S_c} E_E^{veg}, \quad (44)$$

where C [mm] is the canopy storage, E_E^{veg} [mm h^{-1}] is the evaporation rate from the wetted fraction of the canopy, R [mm h^{-1}] is the rainfall rate (if there is dew, it is added to R), and D [mm h^{-1}] is the canopy drainage: $D = K_c e^{g_c(C-S_c)}$, where K_c [mm h^{-1}] and g_c [mm^{-1}] are the drainage rate coefficient and exponential decay parameter [*Rutter et al.*, 1971, 1975]. The parameters S_c [mm] and p [dimensionless] are the canopy capacity and free throughfall coefficient that depend on the amount of biomass of a particular PFT [*Dickinson et al.*, 1993] as $S = 0.1 (L + S)$ and $p = e^{-0.5(L+S)}$. The wetted fraction of the canopy is calculated using the current canopy storage [*Dickinson et al.*, 1993] as $f_{wet} = [C/S]^{2/3} \leq 1$. The Runge-Kutta method is used to obtain C given the instantaneous values of R and E_E^{veg}.

[56] The total canopy evapotranspiration flux E_v^{veg} [mm h^{-1}] in (28) is partitioned into the canopy evaporation E_E^{veg} and transpiration E_T^{veg} according to the relative magnitude of conductances c_e^w and c_t^w (a function of canopy wetted fraction, f_{wet}, Appendix A). Canopy dew E_{Dc}^{veg} is nonzero only if $E_v^{veg} < 0$, $E_{Dc}^{veg} = E_v^{veg}$.

[57] The net precipitation reaching the ground in the kth PFT is $q_{NR,k} = p_k R + D_k$. At the element scale, the net precipitation is obtained by summing the contributions of net precipitation from all PFTs as well as rainfall on bare soil in a manner similar to (43). The element scale quantities for canopy evaporation, transpiration, dew, and total evapotranspiration are calculated similar to equation (42).

8.2. Infiltration and Soil Moisture Fluxes

[58] The water influx at the soil surface can be composed of several components

$$q_{infl} = q_{NR} + q_{dew} + q_{run}, \quad (45)$$

where q_{NR} is the direct rainfall and throughfall, q_{dew} is dew on the ground, and q_{run} [mm h^{-1}] is run-on. Run-on is

estimated as the surface runoff from all the upstream locations that reaches a given element after accounting for all possible reinfiltration events [*Ivanov*, 2006].

[59] The water flux q_{infl} can either infiltrate into the soil column or become runoff. Infiltration and runoff production are simulated by numerically solving the one-dimensional Richards equation [*Hillel*, 1980] that governs the unsaturated fluid flow. When moisture content θ [mm^3 mm^{-3}] is used as a dependent variable, the Richards equation for a sloped surface with balanced subsurface fluxes and zero evapotranspiration is expressed as

$$\frac{\partial \theta}{\partial t} = \frac{\partial}{\partial z}\left(D(\theta)\frac{\partial \theta}{\partial z} - K(\theta)\cos\alpha_{\triangledown}\right), \tag{46}$$

where $K(\theta)$ [mm h^{-1}] is the unsaturated hydraulic conductivity, $D(\theta)$ [mm^2 h^{-1}] is the unsaturated diffusivity, $\alpha_{\triangledown}$ [rad] is the slope of the soil surface, t [h] is time, and z [mm] denotes the normal to the soil's surface coordinate (positive downward, i.e., the direction n). The finite element, backward Euler time stepping numerical approximation is used to solve equation (46). Subsurface lateral exchange in the unsaturated zone and the evapotranspiration flux are accounted for by adding sinks/sources terms into (46). The corresponding formulation and its numerical solution for a one-dimensional soil column are described by *Ivanov* [2006]. The solution permits lateral moisture redistribution in the direction of steepest decent (direction p) as well as the surface and subsurface influx of water from multiple sources located directly above a given element. It also allows for water losses from the soil surface and root zone via the evapotranspiration process using estimates of E_g^{bare}, E_g^{veg}, and E_T^{veg}. The numerical implementation also evaluates the moisture loss from the root zone due to drainage to deeper layers, when there is water excess, or gain due to capillary rise, when the root zone is drier than deeper soil horizons.

[60] The numerical solution of (46) operates on a mesh resolving the vertical variability of soil moisture. Since the finite element method permits multiple resolution, the soil profile is resolved at a high detail near the surface, which allows one to account for the high-frequency variability in atmospheric forcing. The mesh has a coarser resolution at greater depths for computational efficiency. The volumetric water content at the soil surface θ_1 [mm^3 mm^{-3}] is integrated over the first 12 mm of the soil column.

[61] Since the soil column is resolved at multiple points, the root biomass profile (1) can be explicitly captured. If z_i [mm] is a depth in the soil profile, the corresponding fraction of the root biomass r_i [dimensionless], $i = 1\ldots I_{root}$ (note that $\Sigma_i^{I_{root}} r_i = 0.95$) attributed to that depth is

$$
\begin{aligned}
r_i &= 1 - e^{-\eta 0.5\Delta z_i}, & \text{if } & i = 1, \\
r_i &= e^{-\eta(z_i - 0.5\Delta z_{i-1})} - e^{-\eta(z_i + 0.5\Delta z_i)}, & \text{if } & z_i + 0.5\Delta z_i \le Z_{root}, \\
r_i &= e^{-\eta(z_i - 0.5\Delta z_{i-1})} - e^{-\eta Z_{root}}, & \text{if } & z_i + 0.5\Delta z_i \ge Z_{root},
\end{aligned}
\tag{47}
$$

where Δz_i [mm] is the depth difference between the nodes of finite element mesh, z_{i+1} and z_i, and Z_{root} [mm] is the depth that contains 95% of root biomass (corresponds to the I_{root}'s node of the root profile).

8.3. Soil Hydraulic Properties

[62] The *Brooks and Corey* [1964] parameterization is adopted to relate the unsaturated hydraulic conductivity and soil water potential to the moisture content (assuming isotropic media, drainage cycle, and neglecting hysteresis):

$$\psi(\theta) = \psi_b\left(\frac{\theta - \theta_r}{\theta_s - \theta_r}\right)^{-\frac{1}{\lambda_\circ}}, \tag{48}$$

where ψ_b [mm] is the air entry bubbling pressure and λ [dimensionless] is the pore size distribution index. The unsaturated conductivity $K_n(\theta)$ depends on soil moisture content as

$$K_n(\theta) = K_{sn}\left(\frac{\theta - \theta_r}{\theta_s - \theta_r}\right)^{\frac{2+3\lambda_\circ}{\lambda_\circ}}, \tag{49}$$

where K_{sn} [mm h^{-1}] is the saturated hydraulic conductivity in the normal to the soil's surface direction. From (48) and (49), one can obtain an expression for the unsaturated diffusivity $D(\theta)$ [mm^2 h^{-1}]:

$$D(\theta) = K_n(\theta)\frac{d\psi}{d\theta} = K_{sn}\frac{-\psi_b}{\lambda_\circ(\theta_s - \theta_r)}\left(\frac{\theta - \theta_r}{\theta_s - \theta_r}\right)^{2+\frac{1}{\lambda_\circ}}. \tag{50}$$

[63] In the model, the soil anisotropy a_r [dimensionless] is defined as the ratio between the hydraulic conductivities in the directions parallel to the slope K_{sp} and normal to the slope K_{sn}:

$$a_r = \frac{K_{sp}}{K_{sn}}. \tag{51}$$

This implies that soil is assumed to have anisotropy parallel to the slope [*Philip*, 1991].

9. Vegetation Dynamics

[64] As discussed in section 4, each plant type is represented by carbon stored in several compartments. The amount of metabolic (living) carbon is of crucial importance for various biochemical processes that affect the plant carbon balance and lead to either uptake or release of CO_2 from/to the atmosphere. Leaves and fine roots are present in each PFT. Woody species also contain living sapwood, i.e., all living tissues in stem, branches, and coarse roots that exhibit autotrophic respiration, such as sapwood cortical parenchyma, sheathing meristem of phloem tissue, and ray parenchyma extending radially into the xylem tissue. This pool serves as the storage of carbohydrates that are used at the beginning of the growing season to produce new foliage (section 9.7). The pool of structural (dead) wood, on the other hand, represents carbon mostly locked by plant throughout its life, consisting of all other woody tissues of stem, branches, and coarse roots, such as bark, sapwood xylem, and heartwood. Figure 2 illustrates the principal fluxes of carbon to/from living carbon pools and the corresponding vegetation biochemical processes simulated by the model, which are outlined in the following.

[65] Atmospheric carbon dioxide is fixed into carbohydrates and other organic compounds through the processes
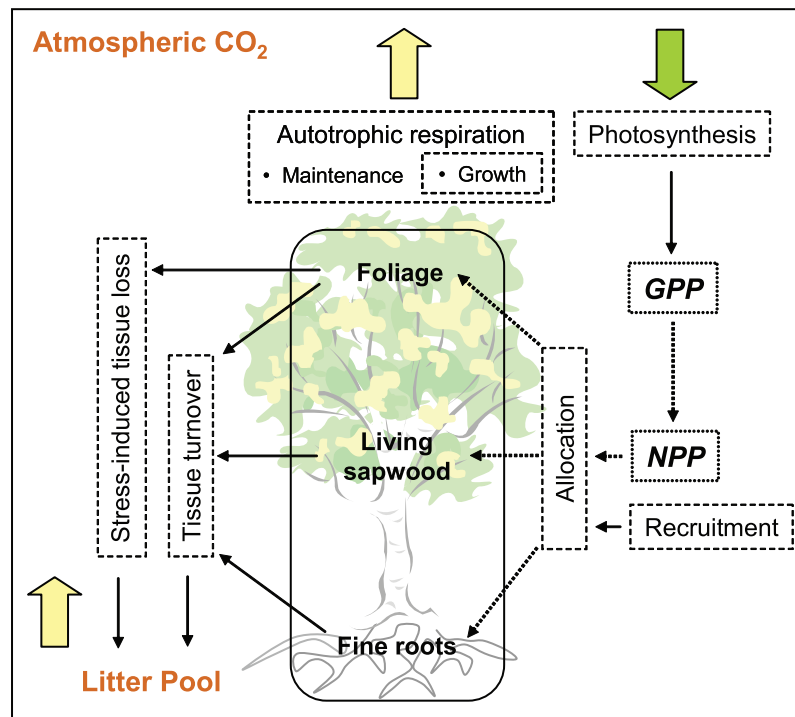
Figure 2. A conceptual diagram of carbon fluxes simulated by the model. The three major carbon pools are leaves, fine roots, and living sapwood (woody species). Boxes outlined with dashed lines illustrate processes that affect the carbon balance. The dotted line boxes represent intermediate quantities, whose magnitude impacts the occurrence of processes that are assumed to follow. The solid line arrows show carbon fluxes, while dotted line arrows depict an intermediate partition of carbon fluxes, which depends on the outcome of carbon balance at the preceding stage. The filled downward arrow depicts carbon uptake from CO_2, while the filled upward arrows show carbon loss.

of photosynthesis. The total amount of uptake is constrained both by biotic (e.g., foliage amount, leaf photosynthetic capacity, etc.) and abiotic (e.g., soil water, radiation, etc.) factors. Two uptake levels are considered in the vegetation foliage: sunlit and shaded canopy fractions, which are treated as "big leaves" with the subsequent scaling to the canopy level. The model of photosynthesis estimates the total plant carbon uptake, or gross primary production (GPP) and, simultaneously, plant canopy respiration. Then it calculates the components of mitochondrial respiration, corresponding to the fluxes from the living sapwood and fine root carbon pools. The sum of respiration fluxes from all compartments constitutes the maintenance respiration, the CO_2 emission resulting from protein repair and replacement and respiratory processes that provide energy for the maintenance of ion gradients across cell membranes [*Penning De Vries*, 1975]. If the difference between GPP and maintenance respiration is positive, growth respiration is estimated. It represents the construction cost (i.e., expended metabolic energy) for new tissue synthesis from mineral and glucose.

[66] The difference between GPP and the sum of all respiration fluxes is the net primary production, NPP. If NPP is positive, the assimilated carbon is allocated to vegetation compartments: canopy, living sapwood, and fine roots (Figure 2). The implemented allocation scheme uses information about the states of plant canopy and water availability in the root zone. For woody species, allocation

is also related to vegetation phenological status. This approach permits dynamic, state-, and stress-dependent allocation patterns as opposed to constant, prescribed allocation fractions.

[67] Turnover of plant tissues that have a certain life span leads to the production of "normal" litter (from leaves and fine roots) and to locking of carbon from living sapwood compartment in the pool of structural wood. Both fluxes depend on sizes of the corresponding plant carbon compartments and are calculated using PFT-specific longevity values for various types of plant tissue. Foliage senescence due to hydrometeorological conditions, which may impose additional controls on the deciduous characteristics of trees and grasses, is also considered. The root zone soil moisture affects the rate of the drought-induced canopy loss, while the air temperature is used to parameterize the foliage loss due to cold conditions.

9.1. Photosynthesis and Stomatal Resistance Model

[68] The canopy photosynthesis model is coupled to the stomatal resistance parameterization and, therefore, is an integral part of the framework that estimates the surface energy fluxes (section 6.3). The coupling scheme follows work of *Farquhar et al.* [1980], *Collatz et al.* [1991] for C_3 plants, and *Collatz et al.* [1992] for C_4 plants:

$$\frac{1}{r_s} = m \frac{A_n \, e_{atm}}{c_s \, e^*(T_v)} P_{atm} + b, \qquad (52)$$

where r_s [s m^2 leaf μmol^{-1}] is the leaf stomatal resistance, m [dimensionless] is an empirical parameter, A_n [μmol CO$_2$ m^{-2} leaf s^{-1}] is the net assimilation rate, c_s [Pa] is the CO$_2$ concentration at the leaf surface, e_{atm} [Pa] is the vapor pressure at the leaf surface, approximated with the atmospheric vapor pressure in a semiarid climate, $e^*(T_v)$ [Pa] is the saturation vapor pressure inside the leaf at the vegetation temperature T_v, P_{atm} [Pa] is the atmospheric pressure, and b [μmol m^{-2} leaf s^{-1}] is the minimum stomatal conductance when $A_n = 0$. Note that the above equation is relevant to a single leaf scale. One needs to integrate (52) to obtain the canopy-scale quantities.

[69] Leaf photosynthesis strongly depends on the type of incident radiation and sunlit and shaded fractions of the canopy can substantially differ in magnitudes of carbon uptake [e.g., *Saeki*, 1961; *Spitters*, 1986; *Norman*, 1993; *Wang and Leuning*, 1998]. As discussed previously, it is appropriate to treat the photosynthetic activities of these canopy fractions as two "big leaves" (section 6.1). Since the maximum photosynthetic rate, Rubisco, electron transport rates, and respiration rate have been shown to covary with leaf nitrogen content [*Ingestad and Lund*, 1986; *Field and Mooney*, 1986], the canopy nitrogen profile also needs to be accounted for to scale photosynthesis to the two canopy levels. The central assumption of the hypothesis used by many land-surface models [e.g., *Sellers et al.*, 1996a] is that the leaf nitrogen content acclimates fully to prevailing light conditions within a canopy and is proportional to the radiation-weighted, time-mean profile of PAR. A simple exponential description of radiation attenuation is used to describe the profile of PAR with the time-mean PAR extinction coefficient $\bar{K}$ [dimensionless]. Taking into account both the instantaneous value of light extinction coefficient K' (section 6.1.3) and the nitrogen extinction parameter $\bar{K}$, the scaling coefficients are obtained for the sunlit F^{sun} and shaded F^{shd} fractions of leaf area index (LAI) [m^2 leaf m^{-2} PFT ground area]. The latter units refer to a vegetated area occupied by a given PFT. In the following, [m^{-2} PFT ground area] is equivalent to [m^{-2} PFT]. The canopy fractions are formulated as

$$F^{sun} = \int_0^L e^{-\bar{K}x} e^{-K'x} dx = \frac{1 - e^{-(\bar{K}+K')L}}{\bar{K} + K'}, \quad (53)$$

$$F^{shd} = \int_0^L e^{-\bar{K}x}\left(1 - e^{-K'x}\right) dx = \frac{1 - e^{-\bar{K}L}}{\bar{K}} - \frac{1 - e^{-(\bar{K}+K')L}}{\bar{K} + K'}. \quad (54)$$

Note that the term $e^{-K'L}$ gives the fractional area of sunlit canopy on a horizontal plane below L (according to Beer's law, equation (10)). The above coefficients are used to obtain estimates of photosynthesis quantities scaled to either sunlit or shaded canopy fractions. For each of the fractions, formulation (52) can be rewritten as

$$\frac{1}{r_s^{CL}} = m \frac{A_n^{CL} e_{atm}}{c_s e^*(T_v)} P_{atm} + F^{CL} b', \quad (55)$$

where index CL refers to either sunlit or shaded canopy levels and $b' = \beta_T b$ takes into account the soil moisture

effects on the minimum stomatal conductance (see Appendix B). The formulation of the photosynthesis model is provided in Appendix B. The model yields the canopy-scale net foliage assimilation rate A_n^{CL}, respiration $R_{mC} = F^{CL} R_d$ [μmol CO$_2$ m^{-2} PFT s^{-1}], and stomatal resistance r_s^{CL} [s m^{-1}].

[70] The stomatal resistances for different canopy levels are explicitly used in the estimation of the latent heat flux (section 6.3). The bulk values of canopy net uptake A_{nC} and respiration R_{mC} are obtained by summing the values for sunlit and shaded canopy fractions: $A_{nC} = A_n^{sun} + A_n^{shd}$, $R_{mC} = F^{sun} R_d + F^{shd} R_d$.

9.2. Net Primary Production and Plant Respiration

[71] The net primary production NPP [g C m^{-2} PFT h^{-1}] can be defined as the gross plant photosynthesis, or gross primary production GPP [g C m^{-2} PFT h^{-1}], less autotrophic respiration R_a [g C m^{-2} PFT h^{-1}]:

$$NPP = GPP - R_a, \quad (56)$$

$$GPP = k_{co2c}(A_{nC} + R_{mC}), \quad (57)$$

where $k_{co2c} = 0.0432$ [g C s μmol CO$_2^{-1}$ h^{-1}] is a unit conversion coefficient. Vegetation autotrophic respiration R_a is estimated as a sum of maintenance R_m and growth R_g [g C m^{-2} PFT h^{-1}] respiration rates: $R_a = R_m + R_g$, where

$$R_m = R_{mC} + R_{mS} + R_{mR}, \quad (58)$$

$$R_g = \omega_{grw}(GPP - R_m), \quad \text{if} \quad GPP > R_m, \quad (59)$$

$$R_g = 0, \quad \text{if} \quad GPP \leq R_m, \quad (60)$$

where ω_{grw} [dimensionless] is a constant (0.25–0.33), and R_{mS} and R_{mR} [g C m^{-2} PFT h^{-1}] are the respiration rates for living sapwood and fine roots. NPP is positive when carbon uptake from photosynthesis exceeds autotrophic respiration. NPP is negative during nighttime or when soil moisture deficit does not allow vegetation to effectively photosynthesize and maintenance costs are higher than gross carbon uptake.

[72] The foliage day respiration R_{mC} is estimated along with photosynthesis (Appendix B). Canopy respiration rate during night time (maintenance respiration of mitochondria) is parameterized in a similar manner ($F^{sun} = 0$): $R_{mC} = k_{co2c} F^{shd} R_d$. The maintenance respiration for sapwood R_{mS} and root biomass R_{mR} are approximated using the first-order kinetics:

$$R_{mS} = r_{sapw} C_{sapw} f_3(T_{atm}), \quad (61)$$

$$R_{mR} = r_{root} C_{root} f_3(T_{soil}), \quad (62)$$

where T_{soil} [K] is from section 6.4, C_{sapw} and C_{root} [g C m^{-2} PFT] are pools of carbon of living sapwood and fine root for a given vegetated fraction, and r_{sapw} and r_{root} [g C g C^{-1} h^{-1}] are the tissue respiration coefficients at 10°C that can

be generally defined as $r_{sapw} = r\,\vartheta/cn_{sapw}$ and $r_{root} = r\,\vartheta/cn_{root}$, where ϑ is a rate of 22.824×10^{-4} h^{-1}, $cn_{sapw} = 330$ and $cn_{root} = 29$ are sapwood and fine root C:N mass ratios [g C g N^{-1}] [*Sitch et al.*, 2003], and r [g C g N^{-1}] is a vegetation-type-dependent coefficient. The temperature dependence function $f_3(T) = \exp[308.56/56.02 - 308.56/(T - 227.13)]$, where T [K] is either T_{atm} or T_{soil}.

9.3. Stress-Induced Foliage Loss and Tissue Turnover

[73] The amount of living carbon that enters the above and below ground litter and the amount of living sapwood that turns to structural (dead) wood are calculated using PFT-specific longevity values for different plant tissues. The turnover and stress-induced foliage loss D_{leaf}, sapwood D_{sapw}, and root D_{root} [g C m^{-2} PFT h^{-1}] turnover rates are parameterized as [*Levis et al.*, 2004; *Arora and Boer*, 2005]

$$D_{leaf} = d_{leaf}C_{leaf} + (\gamma_W + \gamma_C)C_{leaf}, \qquad (63)$$

$$D_{sapw} = d_{sapw}C_{sapw}, \qquad (64)$$

$$D_{root} = d_{root}C_{root}, \qquad (65)$$

where C_{leaf}, C_{sapw}, and C_{root} [g C m^{-2} PFT] are pools of carbon of foliage, living sapwood, and fine root, and d_{leaf}, d_{sapw}, and d_{root} [h^{-1}] are the "normal" turnover rates for foliage, sapwood, and fine roots and represent the inverse values of tissue longevities.

[74] Foliage senescence due to hydrometeorological conditions is also considered. The foliage loss due to the drought stress controls the deciduous characteristics of plants in semiarid areas. The loss rate γ_W [h^{-1}] is parameterized as a function of the PFT-dependent maximum drought loss rate $\gamma_{W\,max}$ [h^{-1}] and the root zone soil moisture factor β_T (Appendix B):

$$\gamma_W = \gamma_{W\,max}(1 - \beta_T)^{b_W}, \qquad (66)$$

where b_W [dimensionless] is the shape parameter reflecting the sensitivity of canopy to drought. The foliage loss due to drought stress is zero when root zone contains a sufficient amount of moisture ($\beta_T = 1$) and is at maximum when $\beta_T \to 0$.

[75] Foliage loss due to cold is parameterized similarly [*Arora and Boer*, 2005]:

$$\gamma_C = \gamma_{C\,max}(1 - \beta_C)^{b_C}, \qquad (67)$$

where $\gamma_{C\,max}$ [h^{-1}] is the PFT-dependent maximum cold foliage loss rate and b_C [dimensionless] is the shape parameter reflecting the sensitivity of canopy to cold, and β_C [dimensionless] is a temperature stress measure defined as

$$\beta_C = 1.0, \qquad \text{if } T_{atm} \geq T_{cold}, \qquad (68)$$

$$\beta_C = \frac{1}{5.0}\left(T_{atm} - (T_{cold} - 5.0)\right), \quad \text{if } T_{cold} > T_{atm} > (T_{cold} - 5.0), \qquad (69)$$

$$\beta_C = 0.0, \qquad \text{if } T_{atm} \leq (T_{cold} - 5.0), \qquad (70)$$

where T_{cold} [K] is a PFT-dependent temperature threshold below which cold-induced leaf loss begins to occur ($b_C < 1.0$).

9.4. Carbon Allocation

[76] If estimated NPP is positive for a given hour, the assimilated carbon needs to be allocated to canopy, fine roots, and living sapwood (woody vegetation) compartments. The implemented scheme relates allocation to the state of plant canopy, water availability in the root zone, and vegetation phenological status (woody species only, section 9.7). The approach follows the conceptual method of *Friedlingstein et al.* [1999], *Salter et al.* [2003], and *Arora and Boer* [2005], which is based on the premises that plants allocate more carbon to (1) fine roots when soil moisture is limiting, so that the below ground biomass increases; (2) canopy when leaves are few in order to increase the photosynthetic carbon gain; and (3) stem/sapwood when foliage significantly limits light penetration to lower canopy levels in order to increase the canopy supporting structure as well as plant height and lateral spread. This approach permits dynamic, state-, and stress-dependent allocation patterns. Following *Arora and Boer* [2005], for woody plant species the allocation fractions are

$$a_P = \frac{e_P + \Pi}{1 + \varpi(2 - \beta_L - \beta_T)}, \qquad (71)$$

where the symbol "P" denotes a given carbon pool: leaves, living sapwood, or fine roots, $\Pi = \varpi\,(1 - \beta_L)$ for sapwood, $\Pi = \varpi\,(1 - \beta_T)$ for fine roots, and $\Pi = 0$ for foliage carbon. $\beta_L = e^{-0.5L}$ is a scalar index used to measure the availability of light. The dynamic allocation fractions a_{sapw}, a_{root}, and a_{leaf} [0–1] are estimated using the base allocation fractions e_{sapw}, e_{root}, and e_{leaf} [0–1] for vegetation state that corresponds to $\beta_L = \beta_T = 1$, and $e_{sapw} + e_{root} + e_{leaf} = 1$. In (71), a decrease in root water availability shifts allocation to roots, while a decrease in available light shifts allocation to stem. When both water and light are available, the allocation is at maximum to leaves. The parameter ϖ [dimensionless] controls the sensitivity of allocation to changes in β_L and β_T. The allocation for grasses follows:

$$a_P = \frac{e_P + \Pi'}{1 + \varpi(1 + \beta_L - \beta_T)}, \qquad (72)$$

where P denotes a given carbon pool: leaves or fine roots, $\Pi' = \varpi\,(1 - \beta_T)$ for fine roots, and $\Pi' = \varpi\,\beta_L$ for foliage carbon, $\beta_L = \max(0, 1 - L/4.5)$ and $e_{root} + e_{leaf} = 1$. *Arora and Boer* [2005] provide more details on the above scheme.

[77] The allocation patterns can be modified under three additional conditions. First, for deciduous trees and shrubs all NPP is allocated to leaves during leaf onset (section 9.7). Second, a sufficient woody and root biomass must be present to support leaves, so that

$$\left(C_{sapw} + C_{root} + C_{strc}\right) \geq \varepsilon_s C_{leaf}^{\xi}, \qquad (73)$$

where C_{strc} [g C m^{-2} PFT] is the pool of structural wood carbon, and ε_s and ξ [dimensionless] are PFT-dependent constants [*Ludeke et al.*, 1994]. The third imposed condition is intended to maintain a minimum root:shoot ratio, i.e., the ratio of fine root carbon to foliage carbon [*Friend et al.*, 1997]. For grasses, the condition (73) is equivalent to the minimum root:shoot ratio.

9.5. Recruitment

[78] Photosynthesis and translocation of carbohydrates from the storage compartment at the beginning of growing season (woody species only, section 9.7) are the primary mechanisms of production of canopy biomass. Recruitment from seeds is another mechanism that may increase biomass of a given PFT.

[79] Currently, only herbaceous species can regenerate through seeds in the model. Both seed germination and seedling establishment require favorable temperature and sufficient amounts of water at appropriate depths in the soil profile and at certain times during the year [e.g., *Peters*, 2000]. The following conditions need to be met for recruitment: (1) the mean daily soil temperature $\overline{T}_{soil}$ has to exceed a threshold value T_{cold}; (2) soil moisture in the top 1/3 of the root maximum depth must be higher than θ^*; and (3) the Julian day of recruitment event must be within a certain period of the year, depending on grass type. If these conditions are continuously met for a certain number of days (e.g., 3 d), the biomass corresponding to leaf area index $L = 0.0025$ is added to the foliage pool of a given grass type. The recruitment root biomass is calculated from the allometric relationship (73).

9.6. Carbon Pool Dynamics

[80] The simulated carbon compartments for leaves, living sapwood (woody species), and fine roots are updated each vegetation model time step based on the estimated carbon fluxes. If NPP is positive, the change in the compartment carbon content is

$$\frac{dC_P}{dt} = a_P \text{NPP} - D_P, \qquad (74)$$

where P denotes a given carbon pool: leaves, living sapwood, or fine roots. As noted in section 9.4, the allocation fractions a_P are computed to satisfy (73) and a minimum root:shoot ratio for postincrement biomass pools. If NPP is negative,

$$\frac{dC_P}{dt} = -(R_{mP} + D_P), \qquad (75)$$

where R_{mP} is the respiration rate for a considered carbon pool. Note that in cases when NPP < 0 but $A_{nC} > 0$, the assimilates are partitioned among the pools and subtracted from the respective respiration costs.

[81] The dynamics of the pool of structural wood carbon, dC_{strc}/dt, is determined by inputs from livewood turnover and losses to litter, the latter being largely as a result of plant damage. A parameterization of the loss function suitable for long-term simulations is being developed.

[82] The aboveground net primary production (ANPP) [g C m^{-2} PFT h^{-1}] is defined as ANPP = $(dC_{leaf} + dC_{sapw})/dt + (D_{leaf} + D_{sapw})$. When summed over the duration of a season, ANPP represents one of the observable metrics of plant performance.

9.7. Vegetation Phenology

[83] Vegetation phenology refers to the timing of onset and offset of leaves, i.e., when plants transit from/to dormancy. Leaf onset and offset mark the bounds of the growing season during which surface albedo, roughness, and water and energy fluxes are dynamically modulated by vegetation. Since the model is applied to arid and semiarid areas, moisture availability effects on vegetation dynamics need to be explicitly considered.

[84] A modified semiempirical "carbon gain" parameterization of *Ludeke et al.* [1994] and *Arora and Boer* [2005] is used here. The essential assumption is that leaf onset starts when it is beneficial, in carbon terms, for a plant to produce leaves. Carbon gains are associated with photosynthesis, while losses are associated with canopy respiration and drought/cold induced foliage losses. Similarly, leaf offset is initiated when environmental conditions are unfavorable for leaf retention in terms of its carbon balance. The carbon gain approach, therefore, directly includes the effects of both temperature and soil moisture since photosynthetic activity, respiration, and foliage losses depend on historical (through soil water dynamics) and current environmental conditions (temperature, radiation, and rainfall).

[85] The transition from one growth state to another is triggered when a set of environmental conditions or a certain vegetation state are met. Leaf phenology differs for woody vegetation and grasses. For deciduous trees and shrubs (evergreen species are not currently considered), there are three leaf phenology stages: dormancy, maximum growth, and the normal growth. For herbaceous species, normal growth is either continuous or follows the dormant stage.

9.7.1. Dormant State to Maximum or Normal Growth

[86] The transition from the state of dormancy to maximum (for woody species) or normal (for herbaceous plants) growth state occurs upon arrival of favorable weather. The overall favorability is signaled by the positive net photosynthesis (less stress losses) from a "virtual" foliage. The virtual canopy represents a certain amount of foliage biomass temporarily assigned to a given PFT during its dormant state. The virtual canopy is assumed to represent the amount of foliage a plant would have at the leaf onset. It is assigned at every time step during dormancy to check whether a given PFT can photosynthesize effectively. For woody species, the virtual canopy is assumed to be proportional to the total amount of nonphotosynthesizing biomass: the initial LAI, L_{init}, corresponds to either 1−5% of the maximum canopy biomass the stem and root pools can support, according to (73), or is set to 0.05−0.2 (species-dependent), whichever is larger. L_{init}, however, might be constrained by the maximum possible amount of carbohydrate translocation from the storage compartment to foliage, which is assumed to be equal to $C_{CH} = 0.67\,C_{sapw}$ [*Friend et al.*, 1997]. For grasses, the virtual canopy LAI is set in the range of 0.05−0.2.

[87] Daily values of $[A_{nC} - D_{leaf}]$ are subsequently accumulated from hourly estimates using the virtual canopy. For the transition to occur, the following conditions have to be met for a given PFT on a daily basis: (1) The total daily net photosynthesis $[A_{nC} - D_{leaf}]$ must be positive (this involves evaluation of D_{leaf} during nighttime with possible

freezing conditions); (2) the ratio of daylight hours with zero or negative assimilation rate A_{nC} to the total number of daylight hours is less than 2/3; (3) the mean daily soil temperature $\overline{T}_{soil}$ has to exceed the threshold T_{cold}; (4) the day length D_{LH} has to exceed a certain threshold value D_{LH}^C; and (5) for grass only: soil moisture in the top 1/3 of the maximum root depth must be above the wilting point. If these conditions are continuously met for a certain number of days (e.g., 5–7 d), a transition occurs to the next phenology state. The maximum potential size of the storage compartment from which carbohydrates will be translocated to form new foliage is set to C_{CH}. The canopy biomass is set to the value corresponding to L_{init} and subtracted from C_{CH}, accounting for growth respiration costs. On the other hand, if a break occurs in the sequence of days when conditions are met (e.g., it becomes too dry or too cold), the counter of favorable days is reset to zero.

9.7.2. Maximum to Normal Growth

[88] During the stage of plant maximum growth (woody species only), all assimilated carbon is allocated to leaves. Additionally, in woody species, the carbohydrate reserves in C_{CH} are translocated to produce new canopy biomass at a specified rate $\gamma_{F\,max}$ [h^{-1}]. The foliage increments account for the expenditures of metabolic energy in synthesis of new tissue by subtracting a constant fraction ω_{grw} from the translocated carbon. The transition from the maximum to normal growth state occurs when a biomass-dependent LAI has been attained. According to *Arora and Boer* [2005], this LAI is approximately 40–50% of the maximum LAI a given stem and root biomass can support. Apparently, this phenological pattern may vary among plant species [e.g., *Schmid et al.*, 2003].

9.7.3. Normal Growth to Dormant State

[89] In the normal growth state, a PFT allocates products of photosynthesis to leaves, living sapwood (woody species), and fine roots. Values of [NPP − D_{leaf}] are accumulated over the day. The following are the necessary conditions for PFT transition to a dormant state (herbaceous and drought-deciduous woody plants): (1) The total daily value of [NPP − D_{leaf}] is negative; and (2) the ratio of daylight hours with zero or negative NPP to the total number of daylight hours is higher than 2/3. A PFT transits to the dormant state if these conditions are met for a certain number of days and (1) for woody species, the amount of foliage biomass is less than 1% of the maximum a given stem and root biomass can support; and (2) for herbaceous species, the above ground biomass is within 10% of the value used for initialization, when vegetation season starts. While the term "dormancy" is used, for grasses it merely implies the end of the active growing season. Biomass dynamics are not tracked until the arrival of favorable conditions.

9.8. PFT Structural Attributes and Fractional Area

[90] Allocation to, and losses from, the carbon compartments make them time-varying. Changes in the biomass contents modify vegetation structural attributes that are used in the energy and water balance calculations.

9.8.1. Woody Species

[91] *Sitch et al.* [2003] suggest an approach to relate the concept of allometry at the plant individual level with the concept of the "average" individual at the element scale.

For each individual, the average individual's LAI, L_{ind} [m^2 leaf area m^{-2} PFT area], which is equal to PFT's LAI, L, is estimated as the following:

$$L_{ind} = L = C_{leaf}\,S_{la}, \tag{76}$$

where S_{la} [m^2 leaf area g C^{-1}] is the specific leaf area and C_{leaf} [g C m^{-2} PFT area] refers to the carbon content of an element area covered by crowns of a given woody species (the sum of nonoverlapping, ground-projected areas of tree/shrub crowns). One can see that an average individual's carbon content in units of [g C individual^{-1}] is $C_{leaf,\,ind} = C_{leaf}\,\Upsilon_{ind}$, where Υ_{ind} [m^2 PFT area individual^{-1}] is the average individual's crown projective area. The stem area index S_{ind} [m^2 stem area m^{-2} PFT area] of an average individual, same as the index of a PFT, S, is assumed to be 25% of maximum L_{ind} for a given PFT (constant).

[92] The foliage projective cover of (FPC) an average individual $f_{v,ind}$ [m^2 FPC area m^{-2} PFT area], defined as the ground area covered by foliage directly above it, is parameterized by the Lambert-Beer law [*Monsi and Saeki*, 2005] as $f_{v,ind} = 1 - e^{-0.5\,(L_{ind}+S_{ind})}$. The fractional cover of a given PFT, f_v, [m^2 FPC area m^{-2} element area] of the element area is

$$f_v = P\,\Upsilon_{ind}\,f_{v,ind}, \tag{77}$$

where P [individual m^{-2} element area] is the population density or the number of individuals per unit area. Note that the product $P\,\Upsilon_{ind}$ specifies the fraction of ground area containing projected areas of all canopy crowns. As can be seen, the vegetation fraction f_v for woody species is the same as the foliage projective cover of an average individual, scaled to the population level. Since f_v is also used in estimating the element-scale hydrological quantities, such as transpiration, the same fraction is also associated with the below-ground fraction of lateral spread of roots.

[93] Height of an average individual H_v [m] and crown projective area Υ_{ind} can be estimated from allometric functions specific for a given PFT [e.g., *Shinozaki et al.*, 1964; *Waring et al.*, 1982]. The approach follows that of *Sitch et al.* [2003].

9.8.2. Herbaceous Species

[94] Grass leaf area index is estimated by equation (76). It is assumed, however, that irrespective of the actual area occupied by grass, only one individual is present, i.e., $P\,\Upsilon_{ind} = 1$. This implies that grass can be homogeneously distributed within the entire element area, if no other vegetation types are present, or only within a fraction of it. This is consistent with the hierarchical approach to modeling vegetation dynamics in ecology [e.g., *Tilman*, 1994], which assumes that grass uniformly occupies space where woody species do not grow. Using the above assumption, it follows that the grass vegetation fraction is the same as the foliage projective cover of grass canopy:

$$f_v = f_{v,ind} = 1 - e^{-0.5,(L+S)}, \tag{78}$$

where S reflects the amount of biomass of grass supporting tissues, taken to be 5% of LAI. The fraction f_v is also used

Table 1. Soil Hydraulic, Heat Transfer, and Albedo Parameters of Generic Soil Types Used in This Paper and by *Ivanov et al.* [2008][a]

Parameter	K_{sn}	θ_s	θ_r	$\lambda_\circ$	ψ_b	$k_{s,dry}$	$k_{s,sat}$	$C_{s,soi}$
Sand[b]	235.0	0.417	0.020	0.592	−73	0.214	2.689	2136115
Loamy sand[c]	45.0	0.401	0.035	0.374	−87	0.214	2.639	2148443
Loam[d]	15.0	0.434	0.027	0.220	−111	0.196	2.250	2205100
Clay[e]	1.0	0.385	0.090	0.150	−370	0.189	1.706	2320750

[a]The hydraulic parameterization follows the work by *Rawls et al.* [1982] with slightly modified values for K_{sn} and $\lambda_\circ$. The heat transfer and albedo parameters are from *Dickinson et al.* [1993] and *Bonan* [1996]. K_{sn} [mm h^{-1}] is the saturated hydraulic conductivity in the surface normal direction, θ_s [mm^3 mm^{-3}] is the saturation moisture content, θ_r [mm^3 mm^{-3}] is the residual moisture content, $\lambda_\circ$ [dimensionless] is the pore size distribution index, ψ_b [mm] is the air entry bubbling pressure, $k_{s,dry}$ and $k_{s,sat}$ [J m^{-1} s^{-1} K^{-1}] are the dry and saturated soil thermal conductivities, and $C_{s,soi}$ [J m^{-3} K^{-1}] is the heat capacity of the soil solid. The soil albedo parameters are assumed to be uniform across all considered soil types. The values of the shortwave albedos for saturated soil ($\alpha^u_{sat\Lambda} = \alpha_{sat\Lambda}$) are assigned as 0.11 for visible and 0.225 for near-infrared spectral bands. The values of the shortwave albedos for dry soil ($\alpha^u_{dry\Lambda} = \alpha_{dry\Lambda}$) are assigned as 0.22 for visible and 0.45 for near-infrared spectral bands.
[b]Sand 92%, clay 3%.
[c]Sand 81%, clay 7%.
[d]Sand 42%, clay 18%.
[e]Sand 20%, clay 60%.

Table 3. Parameters of Biochemical Processes for Generic Broadleaf Deciduous Trees and C$_4$ Grass[a]

Parameter/PFT	Broadleaf Deciduous Tree	C$_4$ Grass
$V_{\max 25}$	90.0	30.0
$\bar{K}$	0.5	0.3
m	9	4
b	10,000	40,000
$\epsilon_{3,4}$	0.08	0.053
r_{sapw}	9.61×10^{-10}	-
r_{root}	109×10^{-10}	400×10^{-10}
ω_{grw}	0.25	0.25
d_{leaf}	1	1
d_{sapw}	1/25	-
d_{root}	1/3	1

[a]$V_{\max 25}$ [μmol CO$_2$ m^{-2} leaf s^{-1}] is the maximum catalytic capacity of Rubisco at 25°C; $\bar{K}$ [dimensionless] is the time-mean PAR extinction coefficient parameterizing decay of nitrogen content in the canopy; m [dimensionless] is an empirical slope parameter; b[μmol m^{-2} s^{-1}] is the minimum stomatal conductance; $\epsilon_{3,4}$ [μmol CO$_2$ μmol^{-1} photons] is the intrinsic quantum efficiency for CO$_2$ uptake for C$_3$ and C$_4$ plants; r$_{sapw}$ and r$_{root}$ [g C g C^{-1} s^{-1}] are the sapwood and fine root tissue respiration coefficients at 10°C; ω_{grw} [dimensionless] is the fraction of canopy assimilation less maintenance respiration utilized for tissue growth; d_{leaf}, d_{sapw} and d_{root} [a^{-1}] are the "normal" turnover rates for foliage, sapwood, and fineroots, representing the inverse values of tissue longevities.

for the below-ground fraction of lateral spread of roots. Grass height is estimated following *Levis et al.* [2004] as $H_v = 0.25\ L$.

10. Model Testing and Confirmation

[95] This section illustrates the various coupling mechanisms captured by the simulation framework in modeling the energy and water budgets of vegetated surfaces. It also demonstrates how vegetation in the model adaptively responds to environmental conditions and adjusts its biomass to both favorable and unfavorable situations. First, the energy partition and soil moisture dynamics are illustrated for surfaces vegetated with generic broadleaf deciduous trees for initially saturated soil. In these examples, the properties of vegetation are assigned at the beginning and

Table 2. Vegetation Biophysical and Interception Parameters[a]

Parameter/PFT	Broadleaf Deciduous Tree	C$_4$ Grass
χ_L	0.01	−0.30
α^{leaf}_Λ(VIS)	0.10	0.11
α^{leaf}_Λ(NIR)	0.45	0.58
α^{stem}_Λ(VIS)	0.16	0.36
α^{stem}_Λ(NIR)	0.39	0.58
τ^{leaf}_Λ(VIS)	0.05	0.07
τ^{leaf}_Λ(NIR)	0.25	0.25
τ^{stem}_Λ(VIS)	0.001	0.22
τ^{stem}_Λ(NIR)	0.001	0.38
K_c	0.18	0.10
g_c	3.9	3.2
S_{la}	0.041	0.020

[a]Here χ_L is the departure of leaf angles from a random distribution and equals +1 for horizontal leaves, 0 for random leaves, and −1 for vertical leaves, α^{leaf}_Λ and τ^{leaf}_Λ [dimensionless] are the leaf reflectances and transmittances, α^{stem}_Λ and τ^{stem}_Λ [dimensionless] are the stem reflectances and transmittances, "VIS" and "NIR" are used to denote the visible and near-infrared spectral bands, K_c [mm h^{-1}] is the canopy water drainage rate coefficient, g_c [mm^{-1}] is the exponential decay parameter of canopy water drainage rate, and S_{la} [m^2 leaf area kg C^{-1}] is the specific leaf area.

do not change throughout the simulation. Second, the fully dynamic response of C$_4$ grass is illustrated for initially saturated or dry soil in terms of its carbon assimilation, CO$_2$ respiration, and turnover fluxes. Next, a model confirmation study is presented in which the simulated aboveground biomass of a generic C$_4$ grass is compared against field measurements for Black Grama grass (*Bouteloua eriopoda*) for a site located in a semiarid environment of central New Mexico.

[96] A generic loamy sand soil is used. The hydraulic properties are parameterized according to *Rawls et al.* [1982]. The heat transfer and albedo parameters are from *Dickinson et al.* [1993] and *Bonan* [1996]. Table 1 provides the corresponding values of the soil hydraulic, heat transfer, and albedo parameters.

[97] The parameters used in the description of canopy radiative transfer, photosynthesis, respiration, turnover, and phenology are assigned according to typical parameterizations for broadleaf deciduous trees and C$_4$ grasses employed in many land-surface schemes [e.g., *Bonan*, 1996; *Sellers et al.*, 1996b; *Foley et al.*, 1996; *Haxeltine and Prentice*, 1996; *Friend et al.*, 1997; *Cox et al.*, 1999; *Kucharik et al.*, 2000; *Levis et al.*, 2004; *Arora and Boer*, 2005; *Krinner et al.*, 2005]. The parameter values are provided in Tables 2, 3, and 4.

10.1. Energy Partition and Soil Water Dynamics of a Flat Surface Vegetated With Broadleaf Deciduous Trees

[98] A weather generator [*Ivanov et al.*, 2007] parameterized for the location of Albuquerque, New Mexico, is used to force the hydrological simulations with 1 August as the starting date, which approximately corresponds to the middle of the monsoon season that drives the major phase of the growing season in New Mexico. To simplify the examples, rainless periods with zero cloudiness are assumed. The corresponding simulated time series of the shortwave radiation are shown in Figure 3a. Another simplification is that the air temperature is simulated in

Table 4. Parameters of Vegetation Allocation, Phenology, and Water Uptake Processes[a]

Parameter/PFT	Broadleaf Deciduous Tree	C_4 Grass
$\gamma_{W\max}$	1/40	1/50
b_W	3.0	4.0
$\gamma_{C\max}$	1/6.7	1/10
b_C	3.0	3.0
T_{cold}	5.0	3.0
e_{leaf}	0.25	0.45
e_{sapw}	0.10	−
e_{root}	0.65	0.55
ϖ	0.80	0.70
ε_s	30.0	1.25
ξ	1.60	1.0
$\bar{T}_{soil}$	10.0	5.0
D^C_{LH}	10	10
$\Delta T_{min,\,Fav}$	7	5
$f_{C,\,init}$ / L_{init}	0.015/0.075	−/0.20
Ψ^*	−0.5	−0.1
Ψ_w	−2.8	−4.0

[a]Here $\gamma_{W\max}$ and $\gamma_{C\max}$ [d^{-1}] are the maximum drought and cold induced foliage loss rates; b_W and b_C [dimensionless] are the shape parameters reflecting the sensitivity of canopy to drought and cold; T_{cold} [°C] is the temperature threshold below which cold-induced leaf loss begins; e_{leaf}, e_{sapw}, and e_{root} [dimensionless] are the base allocation fractions for canopy, sapwood, and roots; ϖ [dimensionless] is the sensitivity parameter of allocation fractions to changes in light and soil water availability; ε_s and ξ [dimensionless] are the constant and exponent, controlling the relation between carbon content in the above and below-ground stores; $\bar{T}_{soil}$ [°C] and D^C_{LH} [h] are the mean daily soil temperature and day length, that have to be exceeded for the growing season to start; $\Delta T_{min,\,Fav}$ [day] is the minimum duration of period for which the conditions of transition from/to the dormant season have to be continuously met; $f_{C,init}$ and L_{init} [dimensionless] are the fraction of the structural biomass and the leaf area index used to initiate the leaf onset; Ψ^* and Ψ_w [MPa] are the soil matric potentials at which the stomatal closure or plant wilting begins.

such a manner as to obtain a smooth time series (Figure 3b). The dew point temperature is assumed to be constant $T_{dew} = 12.8°C$ (corresponding to 30–70% daily variability of humidity typical for the location of Albuquerque for the considered period). Furthermore, the wind speed is also assumed to be constant throughout the simulation, $u_{atm} = 3$ m s^{-1}.

[99] As an initial condition, it is assumed that a loamy sand soil column of 1.8 m depth is completely saturated. Free gravitational drainage is assumed as the lower boundary condition during the simulation. A flat horizontal element is considered, which is not affected by the lateral effects such as shadow cast by remote objects, moisture transfer in the unsaturated zone, or run-on. No groundwater effects are simulated.

[100] Figures 3, 4, 5, and 6 show the results for a surface vegetated with broadleaf deciduous trees with $L = 3.0$, $S = 0.75$, $H_v = 5.0$ m, $d_{leaf} = 4.0$ cm, and $f_v = 1$, i.e., trees occupy the entire area, no bare soil. Vegetation structural attributes and the fractional area do not change during the simulation and therefore only water-energy dynamics are emphasized. The root zone extends down to ~1 m depth with the root biomass distribution parameterized with $\eta = 0.003046$ mm^{-1} (equation (1)). Water uptake parameters are taken as $\Psi^* = -0.5$ MPa and $\Psi_w = -2.80$ MPa. Note that these values are translated to characteristic relative soil moisture values θ^* and θ_w [mm^3 mm^{-3}], used in the estimation of transpiration flux.

[101] As can be seen in Figure 4a, as the soil gradually desaturates, the evaporative fraction decreases. While the daily cycle of the transpiration flux experiences only a minor reduction over the period of time (Figure 4b), the change in soil evaporation is more substantial (Figure 4c) and corresponds to a more significant decrease of the surface soil moisture. Figure 4d shows gravitational drainage from the root zone that exhibits a sharp decline during the simulation.

[102] Figure 5 illustrates temperatures as well as the components of the canopy and ground surface energy balances. Time series of estimated canopy and soil surface temperatures that balance the canopy and ground surface energy budgets are shown in Figure 5a. As can be seen, the maximum radiant temperatures of canopy and ground negatively lag maximum air temperature and are consistently associated with the input of solar energy. The soil surface daily maximum temperatures exhibit a gradual increase throughout the simulation, while the daily course of the canopy temperature remains essentially unchanged. This is attributed to the differences in the soil moisture dynamics at the ground surface and in the root zone. Notice that the
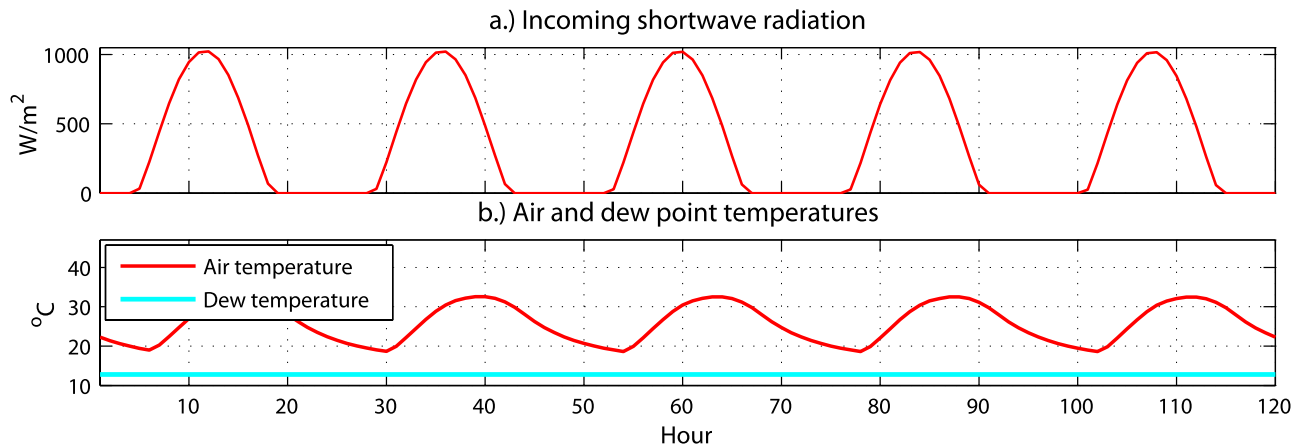
Figure 3. Time series of synthetic hydrometeorological forcing and temperature response: (a) global shortwave radiation and (b) air and dew point temperatures.
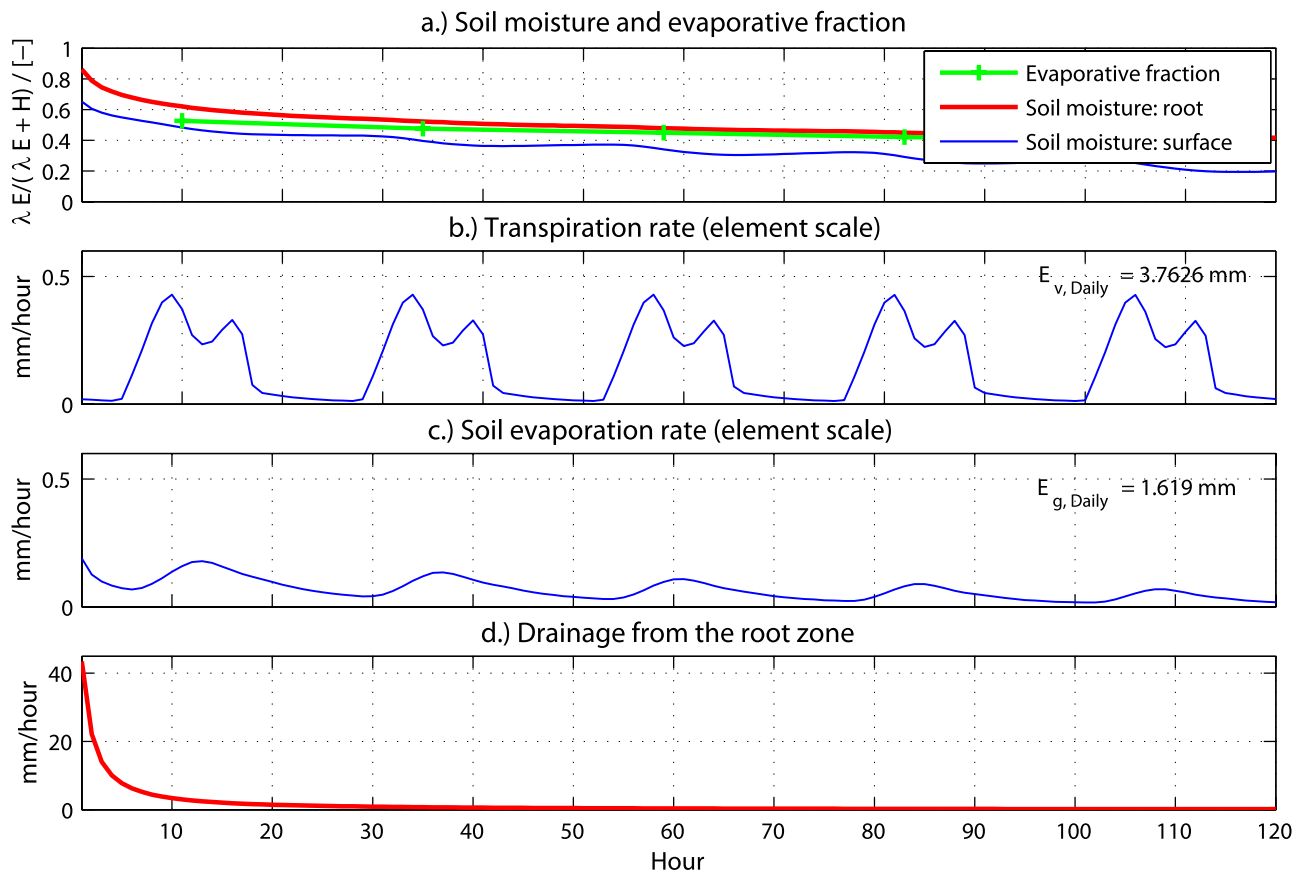
Figure 4. Simulated soil water contents, evaporative fraction, and moisture fluxes for an area vegetated with broadleaf deciduous trees: (a) surface θ_1 and root zone θ_{root} soil moisture and evaporative fraction $\lambda E/(\lambda E + H)$; (b) transpiration rate E_T^{veg}; (c) under-canopy soil evaporation rate E_g^{veg}; and (d) drainage from the root zone to deeper layers $Q_{D\ out}$. "$E_{v,Daily}$" and "$E_{g,Daily}$" are the mean values of daily transpiration and soil evaporation over the simulation period.

dense tree canopy intercepts most of the incoming short-wave radiation (Figure 5b) with a relatively small fraction reaching the under-canopy ground. This results in lower net radiation at the ground surface (Figure 5c). The root zone is relatively wet throughout the simulation and the canopy daylight latent heat flux is therefore high (Figure 5g, midday depressions in the time series are attributed to partial stomatal closure, explained later). Since vegetation exhibits some "leakage" moisture flow (i.e., an uncontrolled loss of water by stomata, section 9.1), the nighttime latent heat flux is somewhat above zero. The soil surface layer dries quickly, which leads to a decrease of latent heat flux and growth of sensible heat flux as well as gradual heating of the surface (Figures 5a, 5f, and 5g). The progressive desaturation of soil also leads to a reduction in the ground heat flux (Figure 5e).

[103] The simulated resistances, used to compute heat fluxes from the ground and canopy surfaces, are illustrated in Figure 6. Since wind is constant, aerodynamics and leaf boundary layer resistances are time-invariant (Figure 6a). The stomatal resistances, shown in Figure 6b for sunlit and shaded fractions of the canopy exhibit a midday peak during the daily cycle. This model behavior has been previously reported [Collatz et al., 1991] and is associated with partial stomatal closure caused by high daylight time air moisture deficit (T_{dew} is constant in this example) as well as signif-

icant shortwave irradiance of the leaves (Figure 5b). The increase in the stomatal resistance causes the midday depressions in the photosynthesis and latent heat flux (Figure 5g), experimentally observed in leaves [Beyschlag et al., 1986] and open canopies [Tan and Black, 1976; Campbell, 1989; Kinyamario and Imbamba, 1992]. Contrasting this observed feature, the biochemistry of C_4 grass is less sensitive to the extreme environments of arid areas. A similar numerical experiment carried out for a generic C_4 grass does not exhibit midday depressions in the latent heat flux [Ivanov, 2006].

[104] The decrease in the surface soil moisture leads to a higher resistance to the ground latent heat flux (Figure 6c). An apparent periodicity in the time series is due to the daytime depletion of moisture and nighttime capillary rise that partially replenishes surface soil water.

[105] The above experiment illustrates the dynamic coupling between soil hydrological states and vegetation stomatal response and highlights important aspects of interrelationships among energy-water dynamics. Furthermore, it points to the significance of modeling at fine timescales. As the stomatal response to hydrometeorological forcing is highly nonlinear, using the mean daily quantities would not result in the same estimates of energy and moisture fluxes, as compared to those obtained from subdaily variations. The case considered so far, however,
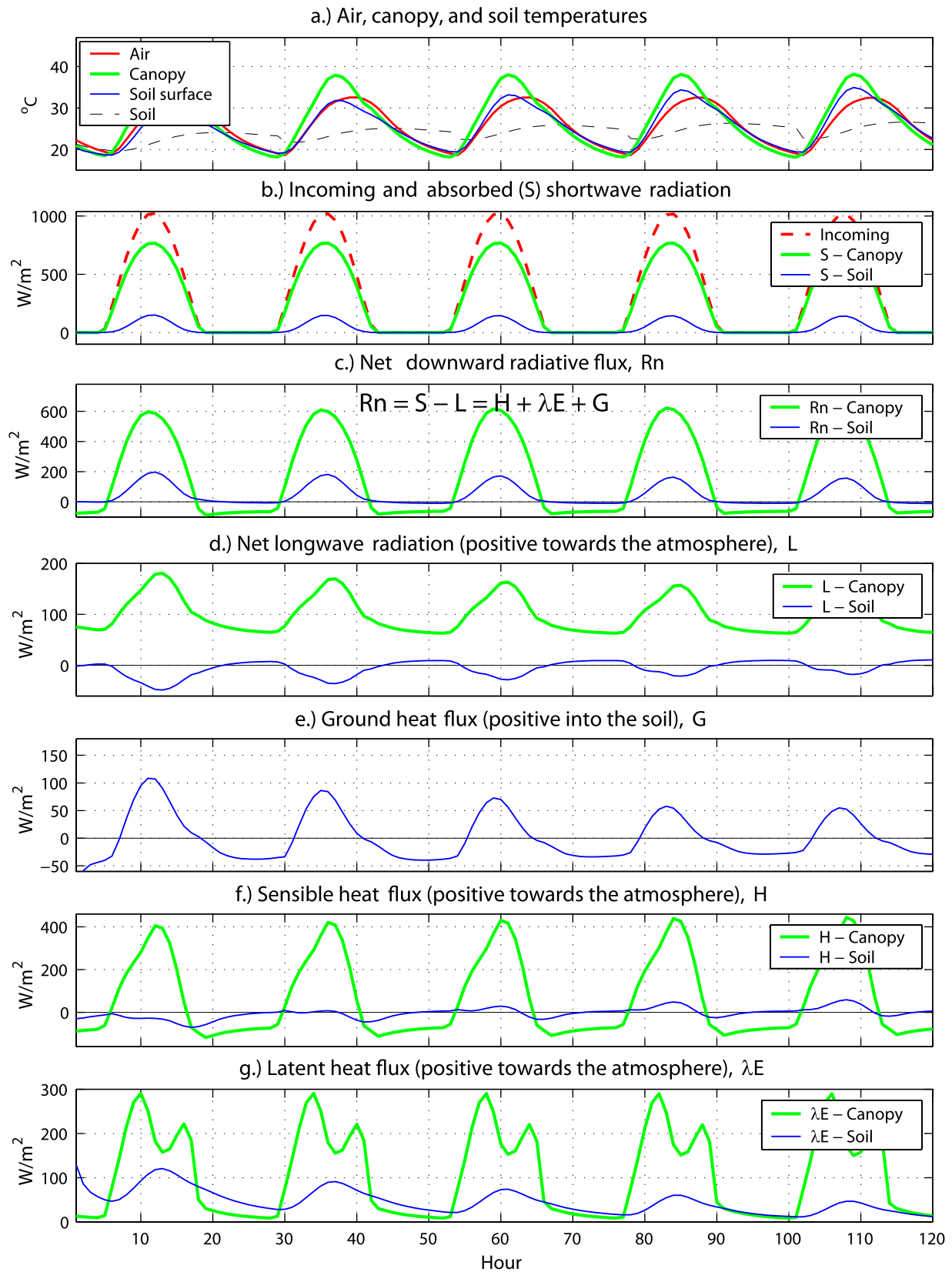
Figure 5. Temperature response and components of canopy and ground surface energy budgets for an area vegetated with broadleaf deciduous trees: (a) air T_{atm}, canopy T_v, soil surface T_g, and soil T_{soil} temperatures; (b) incoming global and absorbed shortwave radiation (($S_{atm}\downarrow_\Lambda{}^\mu + S_{atm}\downarrow_\Lambda$) and ($\vec{S}_v^{veg}$ and $\vec{S}_g^{veg}$)); (c) net radiation (R_{nv} and R_{ng}); (d) net longwave radiation ($\vec{L}_v^{veg}$ and $\vec{L}_g^{veg}$); (e) ground heat flux G; (f) sensible heat flux (H_v^{veg} and H_g^{veg}); (g) latent heat flux (λE_v^{veg} and λE_g^{veg}).
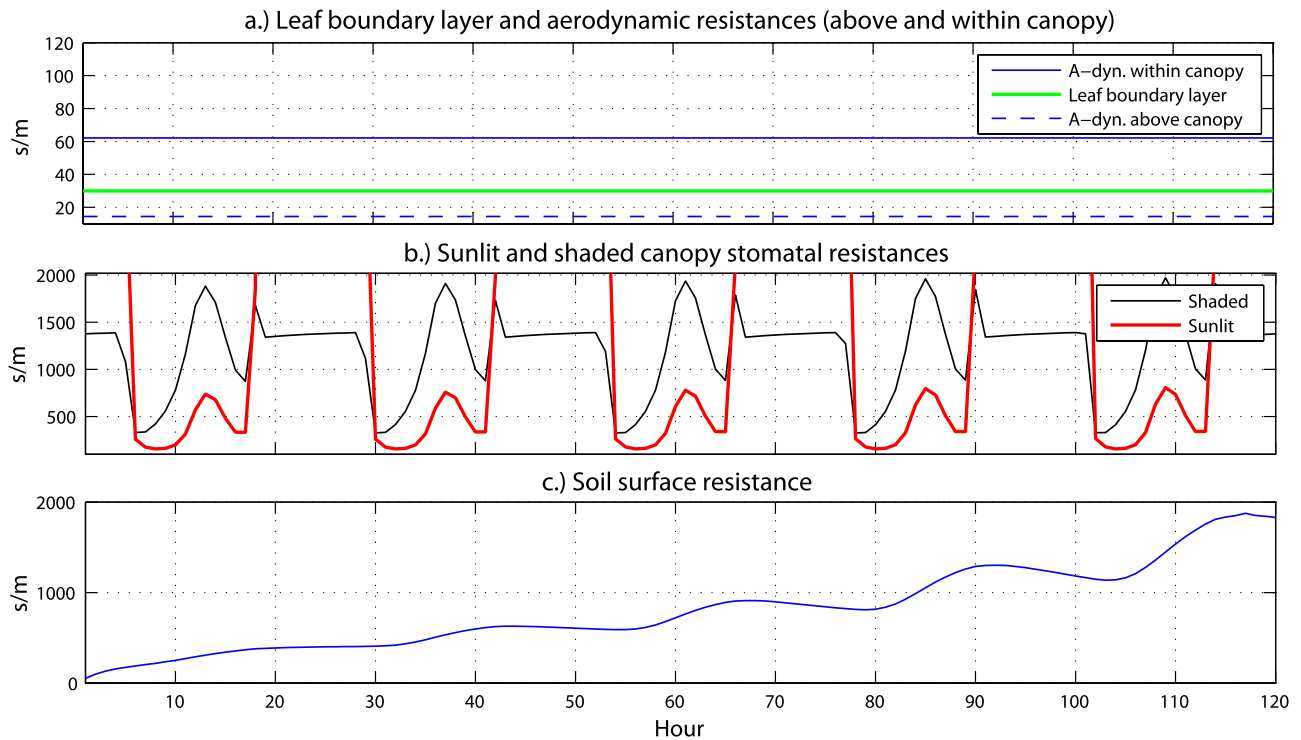
Figure 6. Simulated resistances used to estimate canopy and ground surface energy fluxes for an area vegetated with broadleaf deciduous trees: (a) leaf boundary layer r_b and aerodynamic resistances (r_{ah} and r'_{ah}); (b) sunlit and shaded canopy stomatal resistances (r_s^{sun} and r_s^{shd}); (c) soil surface resistance r_{srf}.

does not include vegetation dynamics, which should not be significant for broadleaf deciduous trees over the period of 5 d. The following example will discuss feedbacks of vegetation dynamics to hydrometeorological conditions and the soil water state.

10.2. Vegetation Processes of C$_4$ Grass for Favorable and Unfavorable Soil Moisture Conditions

[106] The hydrometeorological forcing and soil characteristics are the same as in the previous example. A generic C$_4$ grass is used with $L = 3.0$, $S = 0.15$, $H_v = 0.75$ m, and $d_{leaf} = 0.5$ cm. The root zone extends down to $\sim$0.33 m depth, with $\eta = 0.009$ mm^{-1}. Water uptake properties are taken as $\Psi^* = -0.1$ MPa and $\Psi_w = -4.0$ MPa. The structural attributes and the fractional area of grass are dynamically updated throughout the simulations.

[107] In the first numerical experiment, it is assumed that loamy sand soil column of 1.8 m depth is initially completely saturated. Figure 7 illustrates the estimated canopy and ground temperatures, soil water state, and biochemical rates of carbon assimilation and release of CO$_2$. As soil dries from the initially saturated state, one can observe a substantial growth in the daily amplitude of the ground surface temperature (Figure 7a). The transpiration factor β_T and the foliage assimilation (Figures 7b and 7c), are not affected until hour 82, after which one can observe a slight decrease in the assimilation rates and productivity. Since the soil water store and incoming PAR are in sufficient quantities, NPP is positive during the daylight hours throughout the entire simulation. Grass can both support its existing biomass and uptake new carbon. The maintenance respiration rates for the grass canopy and root biomass (Figure 7d) during daylight hours are around 15–20% of the gross CO$_2$

assimilation and exhibit diurnal variability associated with the changes in canopy and soil temperatures. Note that the sum of maintenance and growth respiration over the simulation period is around 50% of the total gross CO$_2$ uptake.

[108] Figure 8 illustrates the estimated variables characterizing the canopy and root zone states. As the soil surface and root zone become drier (Figure 7b), the diurnal cycle of the canopy state (Figures 8a, 8b, and 8c) changes only slightly. The canopy exhibits higher water vapor content than the atmosphere above (Figure 8a). The canopy stomatal resistances (Figure 8b), sunlit and shaded, exhibit a relatively minor growth on the last day of simulation, associated with the change in β_T. Since the simulation spans only a period of favorable conditions, the canopy biomass grows slightly, which is reflected in the maximum magnitude of sunlit and shaded leaf area index (Figure 8c). Note that the total LAI is shown as the shaded LAI during nighttime hours.

[109] In the second experiment, dry soil conditions are assumed for the same initial vegetation state (Figures 9 and 10). As can be seen in Figure 9b, the soil is initially very dry with β_T close to zero. The soil surface becomes slightly wetter due to dew on the soil surface. The daily amplitudes of the estimated ground surface and canopy temperature are substantially higher than those of the previous case since transpiration and soil evaporation fluxes are near zero. The low root zone soil water results in the stomatal closure and, consequently, zero foliage CO$_2$ assimilation rates. Since artificially high biomass is initially assigned, the maintenance respiration rate is also high. Consequently, the NPP is negative throughout the simulation (Figure 9c). The outcome of the combined effect of water-stressed conditions
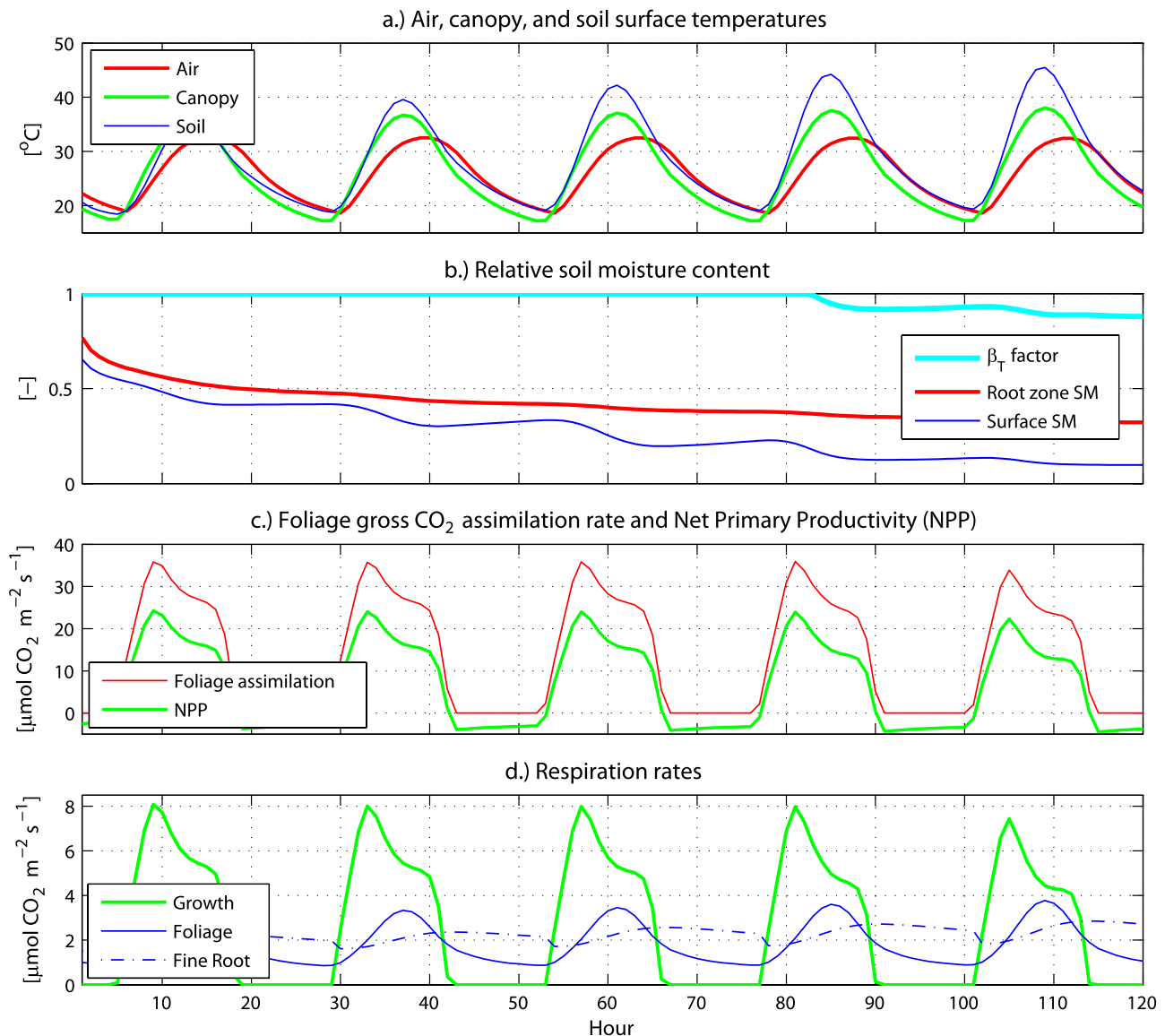
Figure 7. Time series of environmental characteristics and grass biochemical CO_2 fluxes for initially wet soil: (a) air, canopy, and soil surface temperatures; (b) relative soil moisture contents and transpiration factor β_T; (c) foliage gross CO_2 assimilation rate and net primary productivity (NPP); (d) growth, foliage, and root respiration flux rates.

and high initial biomass is a high drought-induced carbon loss of foliage biomass (Figure 10a). Because of the overall negative carbon balance, the canopy and fine root carbon pools rapidly reduce within the considered period of time (Figure 10b). As a consequence, the vegetation fraction also rapidly decreases.

[110] The above examples illustrate the dynamic features of vegetation. As was shown, grass is responsive to both favorable and unfavorable conditions and can adjust its biomass rapidly. The temporal evolution of canopy and ground level energy partition correspondingly depends on changes in biomass. If vegetation is considered static, then, on average, one could expect the following differences in behavior with respect to a fully dynamic case: (1) higher sensible heat/smaller transpiration and slower depletion of soil water reservoir during favorable periods; and (2) shorter timescales of soil moisture depletion during drier, rainless periods. The significance of such effects for modeling land-surface processes needs to be investigated.

10.3. Confirmation of Vegetation-Hydrology Model for C_4 grass

[111] This section outlines a model confirmation/verification study based on measurements of the aboveground biomass, Bowen ratio variables (J. R. Gosz, Bowen ratio evapotranspiration data, 1996–1999, Sevilleta LTER Database, 2000, http://sevilleta.unm.edu/data/archive/climate/bowen/[March 2007]), and soil moisture (J. R. Gosz, Time domain reflectometry, soil moisture, 1996–1999, Sevilleta LTER Database, 1999, http://sevilleta.unm.edu/data/archive/soil/tdr/March 2007) for a semiarid site of central New Mexico, located in Sevilleta National Wildlife Refuge. The Sevilleta Refuge is a Long-Term Ecological Research site focused on studying climate change
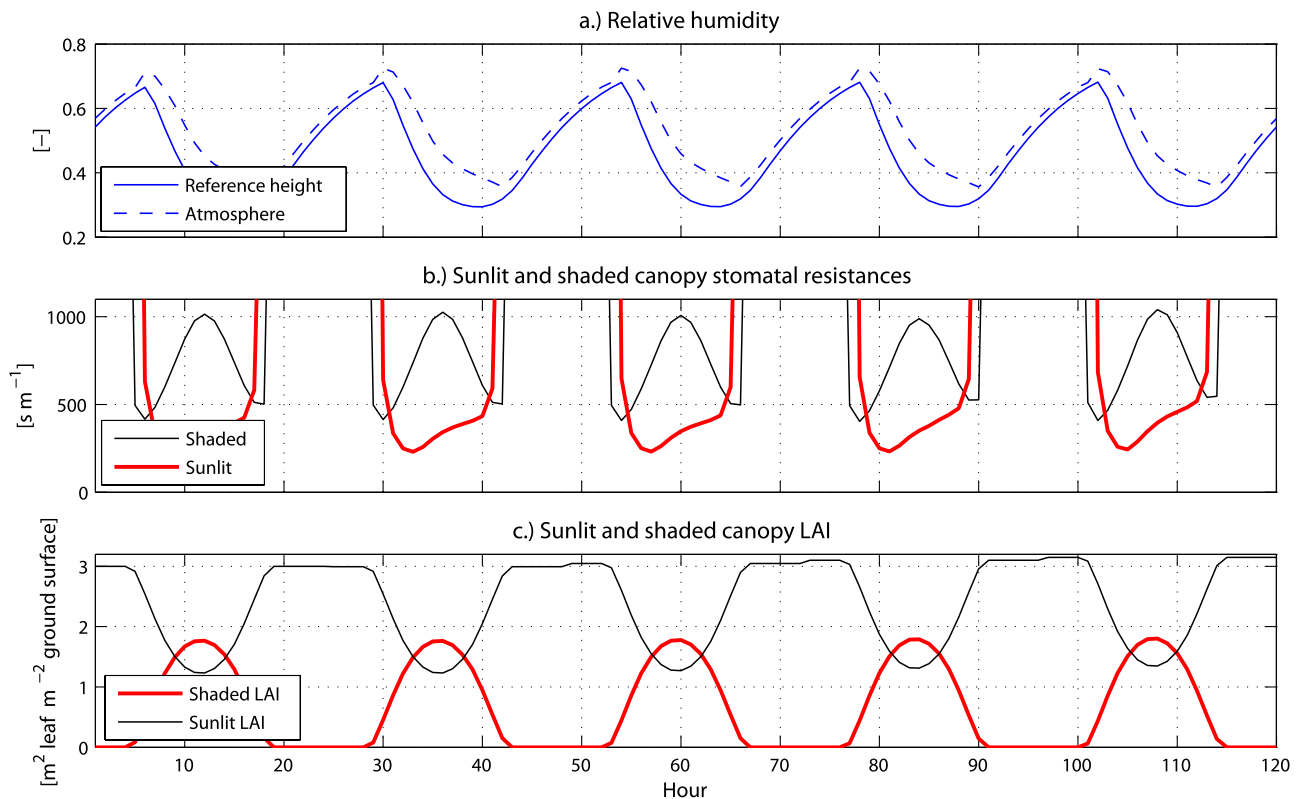
Figure 8. Time series of environmental and biophysical characteristics for initially wet soil: (a) relative humidity of the atmosphere and canopy-space air (at the reference height $z_{0h} + d$); (b) sunlit and shaded canopy stomatal resistances; (c) sunlit and shaded canopy LAI. Note that the shaded LAI equals to the total LAI during nighttime hours.

effects in a biome transition zone as well as habitat and biodiversity of semiarid environments. Long-term records from a weather station in Socorro (~40 km south of Sevilleta) show that the annual precipitation ranges between 100 and 500 mm, with a mean value of 244 mm. Summer precipitation occurs as intense thunderstorms accounting for over half of the annual rainfall, while El Niño-Southern Oscillation (ENSO) influences winter precipitation [*Milne et al.*, 2003]. Mean monthly temperatures range from 2.5°C to 25.1°C.

[112] Hourly time series of hydrometeorological variables are required to force the vegetation-hydrology model: rainfall, cloud cover, shortwave radiation (with partition into direct and diffuse types, as well as into VIS and NIR wave bands), air and dew point temperatures, and wind speed. Several weather stations (J. R. Gosz, Meteorological data, 1988–1999, Sevilleta LTER Database, 2000, http://sevilleta.unm.edu/data/archive/climate/meteorology/ [March 2007]) operated in the Sevilleta during the period of 1989–1999. Station 40 (the Deep Well site, 34.36°N, 106.69°W) is the closest to the fertilization site (see section 10.3.1). Since the available data did not include cloudiness data and the partition of shortwave radiation, observational data at the Albuquerque airport were used in addition to synthesize a complete set of forcing data. Because of the relative proximity of Albuquerque to the Sevilleta Refuge (~80 km north), the following methodology was used: (1) the cloudiness data for Albuquerque were used without

changes; (2) the global solar radiation at Station 40 was partitioned into the direct beam and diffuse components using the same fractional composition as observed in Albuquerque; and (3) to partition the radiative fluxes into the VIS and NIR bands, the calibrated radiative transfer model of *Gueymard* [1989] (a component of a weather generator described by *Ivanov et al.* [2007]) was utilized; the obtained fractional composition was then applied to the observed data. Additionally, data gaps were filled with data corresponding to a nearest weather station in Sevilleta.

[113] Inspection of digital elevation data for the area of interest reveals that its topography can be characterized as a flat surface situated in a nonconvergent terrain location. Therefore, all simulated dynamics are assumed to be one-dimensional with negligible lateral effects such as radiative shading or water transfer from adjacent areas. A flat plot-scale element is used for simulations. Since no data are available on the hydraulic properties of Turney Loamy Sand soil (see section 10.3.1), a generic loamy sand soil type [*Rawls et al.*, 1982] is used (Table 1).

[114] The soil water profile was initialized with a uniform depth-averaged value of $0.1\ \theta_s$, corresponding to -7 MPa of the suction pressure head. In order to reduce the effect of initial soil moisture conditions on the results, a 1-year spin-up period was introduced. The simulation thus spans the period of 1988–1999 with all vegetation-hydrology dynamics driven by deterministic forcing from the observed (partially synthesized) meteorological data.
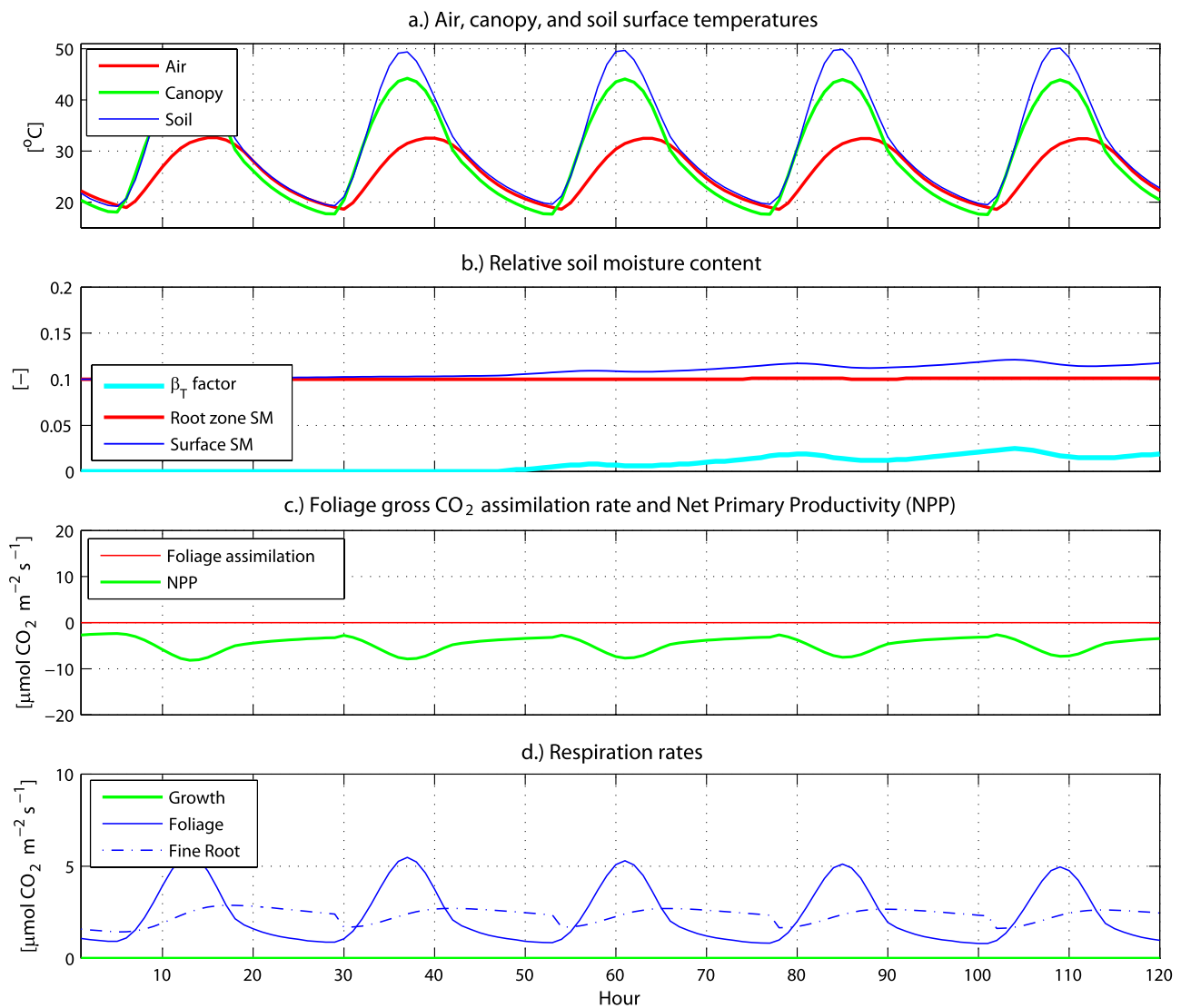
Figure 9. Time series of environmental characteristics and grass biochemical CO_2 fluxes for initially dry soil: (a) air, canopy, and soil surface temperatures; (b) relative soil moisture contents and transpiration factor β_T; (c) foliage gross CO_2 assimilation rate and net primary productivity (NPP); (d) growth, foliage, and root respiration flux rates.

10.3.1. Grass Biomass

[115] In 1989, a study was initiated to examine the effect of fertilization on grassland productivity (J. R. Gosz, C_3-C_4 Biomass, 1989–1992, Sevilleta LTER Database, 2000, http://sevilleta.unm.edu/research/local/plant/fertilizer/data/wt_summary [January 2005]). Plots were established on the east and west sides of the Sevilleta. The site on the east side, McKenzie Flats site, represents mixed Chihuahuan Desert and Great Plains Grasslands on Turney Loamy Sand soil, dominated by warm season C_4 grasses, such as Black Grama (*Bouteloua eriopoda*) with lesser amounts of Blue Grama (*Bouteloua gracilis*) and Galleta Grass (*Hilaria jamesii*). Since the C_4 photosynthesis pathway is typical for grasses in semiarid environments, the data for McKenzie Flats site were used in this study.

[116] The site was gridded into 30 m × 30 m plots. In 1989 and 1990, fertilizer treatment, in the form of NH$_4$-NO$_3$, was applied to the site. In 1989 and 1990, nine and eight plots, respectively, were randomly selected among the treatment and control plots both during the late spring and early fall. Within each plot, three 1 m × 0.5 m quadrats were randomly selected and clipped to estimate plant biomass. A subsequent laboratory procedure consisted in sorting the clipped plant material into live (green) and dead material by species. The samples were oven dried and the weights from the three quadrats were then averaged to provide live and dead biomass estimates in [g m^{-2}] of the plot. The fertilization aspect of the study was discontinued after 1990, but biomass samples from the plots continued to be collected through 1992 to monitor annual vegetation production of the grasslands. The period of 1989–1992 appears to be particularly suitable for verification since the annual precipitation recorded at the Deep Well station involved two contrasting years of below-average 156 mm in 1989 and above-average 335 mm in 1991 (1990, 244 mm; 1992, 240 mm).
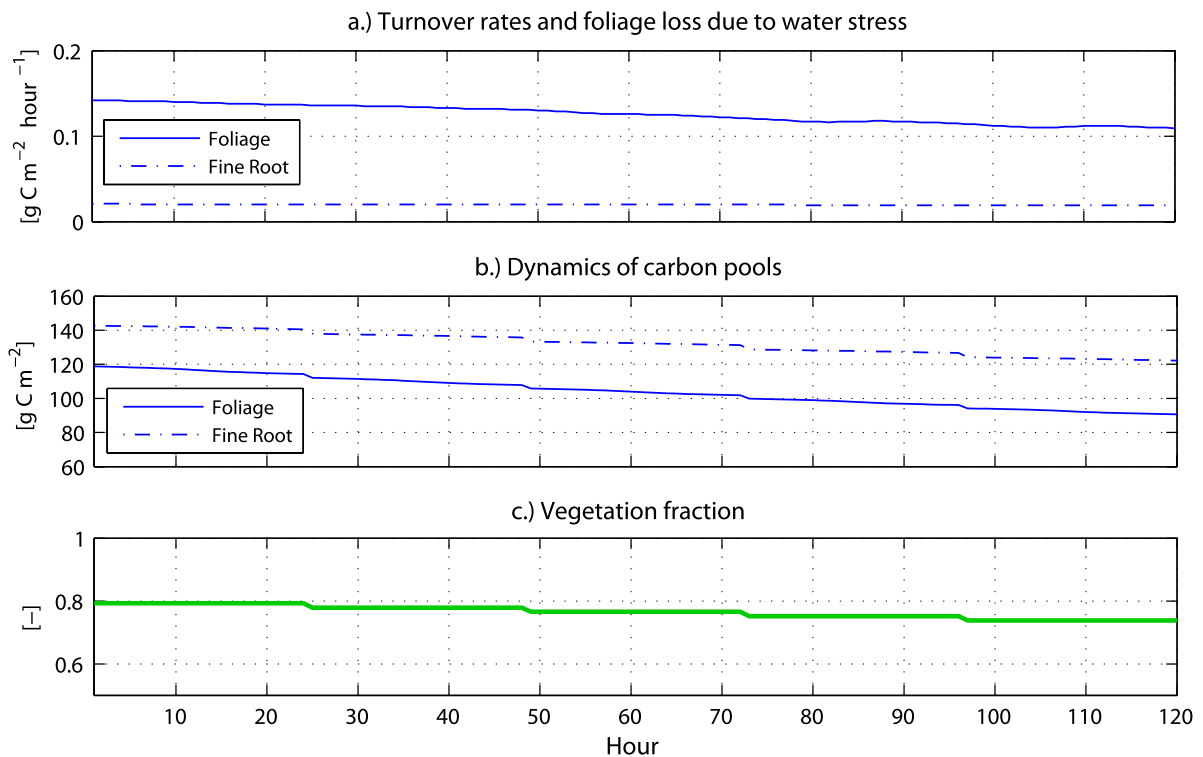
Figure 10. Time series of grass water stress induced foliage loss, dynamics of carbon pools and vegetation fraction for initially dry soil: (a) foliage and root turnover rates (vegetated fraction scale); (b) foliage and root carbon pool dynamics (computational element scale); (c) vegetation fraction dynamics.

[117] Figure 11 illustrates the simulation results and measured data on grass biomass. One can clearly observe the relative difference in terms of precipitation among the illustrated years. For example, winter and spring of 1989 were drier than other years of the simulation period (Figure 11a). Correspondingly, the pregrowing season root zone soil water content was lower and the grass development was essentially delayed until the arrival of the monsoon in July. Precipitation during the monsoon period was also relatively smaller and, consequently, the total grass biomass was smaller for 1989. In contrast, the hydrometeorological conditions in 1991 favored grass development since there was a substantial soil water content at the beginning of the growing season and precipitation during the monsoon was higher than in other years. The simulated biomass exhibits rapid development during the spring and subsequent accumulation in the summer. Consequently, the soil water partition into outfluxes shows considerable differences between 1989 and 1991. For instance, the amount of soil evaporation in 1989 is almost equal to that of 1991, while the amount of transpiration is substantially smaller in 1989.

[118] It is worth noting that with the arrival of favorable conditions, after a prolonged stress period, grass does not immediately transpire at maximum potential rates. This case is most apparent for the summer of 1992 (Figure 11b), although the timescale is too coarse to clearly observe that. An initial period of biomass growth exists during which the grass fractional area increases. During such a period, soil water is depleted primarily through soil evaporation at rates relatively smaller than the maximum potential transpiration rates, due to the control imposed by the highly variable moisture at the soil surface. Only after attaining a certain cover fraction can grass transpiration reach the potential rates, e.g., $1.5-2$ mm d^{-1}. Such a situation thus illustrates a case where some ecohydrological models with static vegetation may fail to properly estimate soil water dynamics. These models typically assume rates near the potential transpiration, immediately after the arrival of favorable conditions [e.g., *Cordova and Bras*, 1981; *Rodriguez-Iturbe et al.*, 1999a; *Laio et al.*, 2001a].

[119] Figure 11c illustrates the simulated gross photosynthetic uptake and NPP. As discussed in section 9.7, the growing season starts only when the imposed conditions for leaf onset are met, with the positive net photosynthesis (less foliage stress losses) assumed to be the key criterion. Figure 11d compares the simulated and measured aboveground biomass. While the input meteorological data and the experimental setup contain certain problems (e.g., missing data, artificial partition of global radiation, soil moisture initialization, generic soil parameterization), the simulated C_4 grass biomass does exhibit the same pattern and consistency as the measured data. One may notice a delay in growth during the driest year and a faster accumulation during favorable periods. The simulated minimum root:shoot ratio ($\varepsilon_s = 1.25$) is always maintained. The simulation results also indicate that variability of grass biomass during the growing season can be quite significant. For example, the results for 1991 and 1992 show substantially different dynamics of foliage due to the differences in precipitation
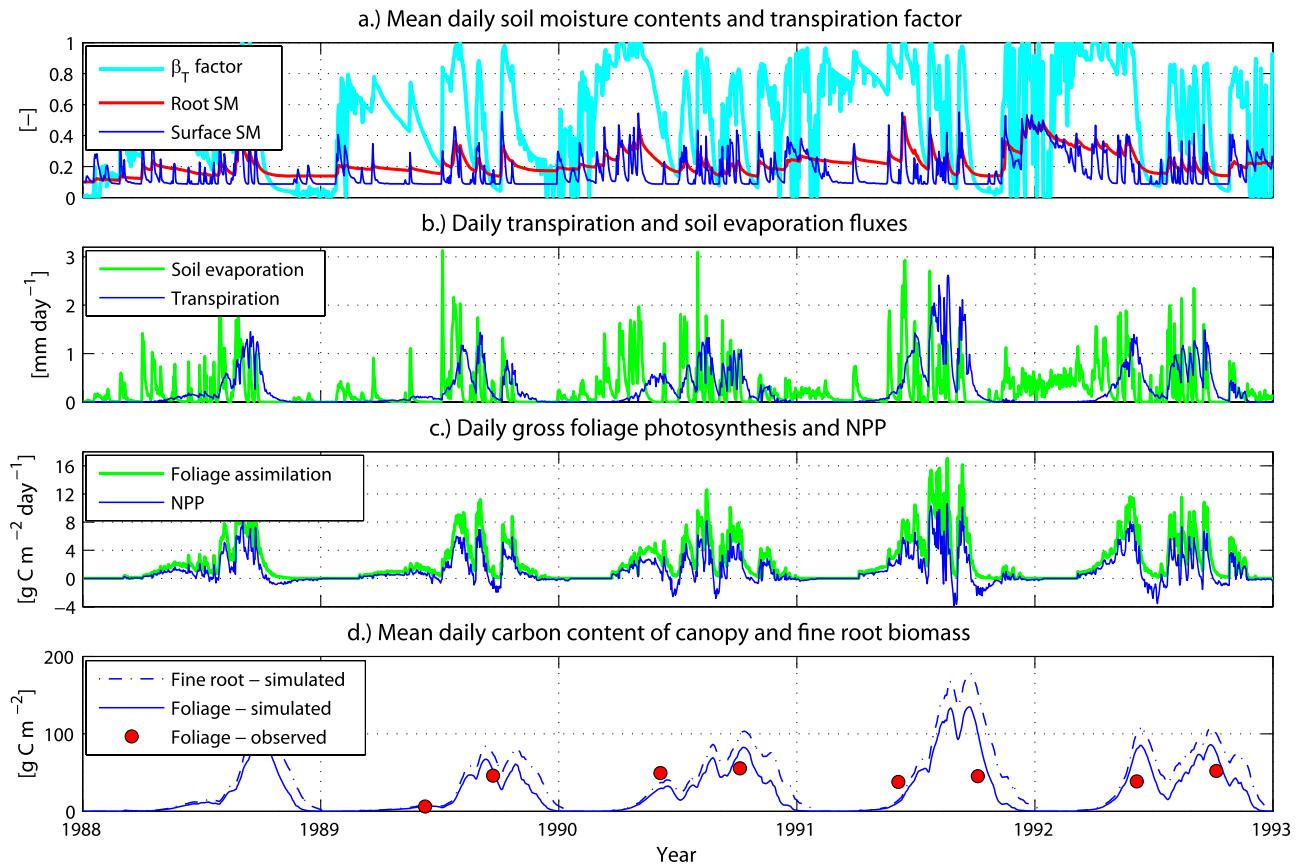
Figure 11. Time series of (a) simulated mean daily relative soil moisture contents and transpiration factor β_T; (b) total simulated daily transpiration and soil evaporation; (c) simulated gross foliage assimilation and net primary productivity (NPP); (d) simulated and observed above ground carbon content in grass biomass for McKenzie Flats site in the Sevilleta National Wildlife Refuge. The fluxes and densities are provided as the element scale quantities.

regimes. The observations, however, do not directly suggest the existence of this variability, most likely because the measurements were carried out either to early or too late in the growing season.

10.3.2. Energy Fluxes and Soil Moisture

[120] In addition to the above test, data for a Bowen ratio tower (J. R. Gosz, Bowen ratio evapotranspiration data, 1996–1999, Sevilleta LTER Database, 2000, http://sevilleta.unm.edu/data/archive/climate/bowen/ [March 2007]), which was located adjacent to the Deep Well meteorological station, are used in this study for further confirmation of model consistency. Data for the entire observation period of 1996–1999 are used for comparison with modeled data taken from a simulation that continuously extends the previous modeling run through 1999. Additionally, Time Domain Reflectometry (TDR) soil moisture data (J. R. Gosz, Time domain reflectometry, soil moisture, 1996–1999, Sevilleta LTER Database, 1999, http://sevilleta.unm.edu/data/archive/soil/tdr/ [March 2007]) are available for the Deep Well site for the same period and are used to complement this test data set. Detailed information on observational design of Bowen ratio and soil water content measurements can be found in the relevant Web-based documents (J. R. Gosz, Bowen ratio evapotranspiration data, 1996–1999, Sevilleta

LTER Database, 2000, http://sevilleta.unm.edu/data/archive/climate/bowen/ [March 2007]).

[121] Figure 12 illustrates a comparison between the observed and modeled data for the period of 22 June through 26 July 1998. Note that net radiation is an independent measurement, while latent heat flux is estimated as a fraction of the difference between net radiation and ground heat flux divided by the sum of unity and Bowen ratio [e.g., *Lewis*, 1995]. The latter is computed from the observed temperature and vapor pressure gradients over grass. Original data provide soil heat flux from two flux plates buried at 10 cm at the Deep Well site. In computing the ground heat flux at the soil surface G_0 [W m^{-2}], heat storage in the top 10 cm was accounted for as $G_0(t) = G_{0d}(t) + C_s\ d_p\ \Delta T_{0-d}(t)/\Delta t_m$, where $G_{0\,d}$ is the flux measured at depth $d_p = 0.1$ m, ΔT_{0-d} [K] is the change in soil temperature of top 10 cm since the last observation $\Delta t_m = 1200$ [s] period, and C_s [J m^{-3} K^{-1}] is the soil heat capacity estimated according to equation (37), accounting for water content in the soil of thickness d_p. The latter was obtained as the mean value of soil moisture contents at depths of 5 and 10 cm, measured using TDR probes. The estimation of coefficients involved in the latent heat flux computation follows a standard procedure provided by Campbell Scientific (supplier of the utilized Bowen ratio system) in the
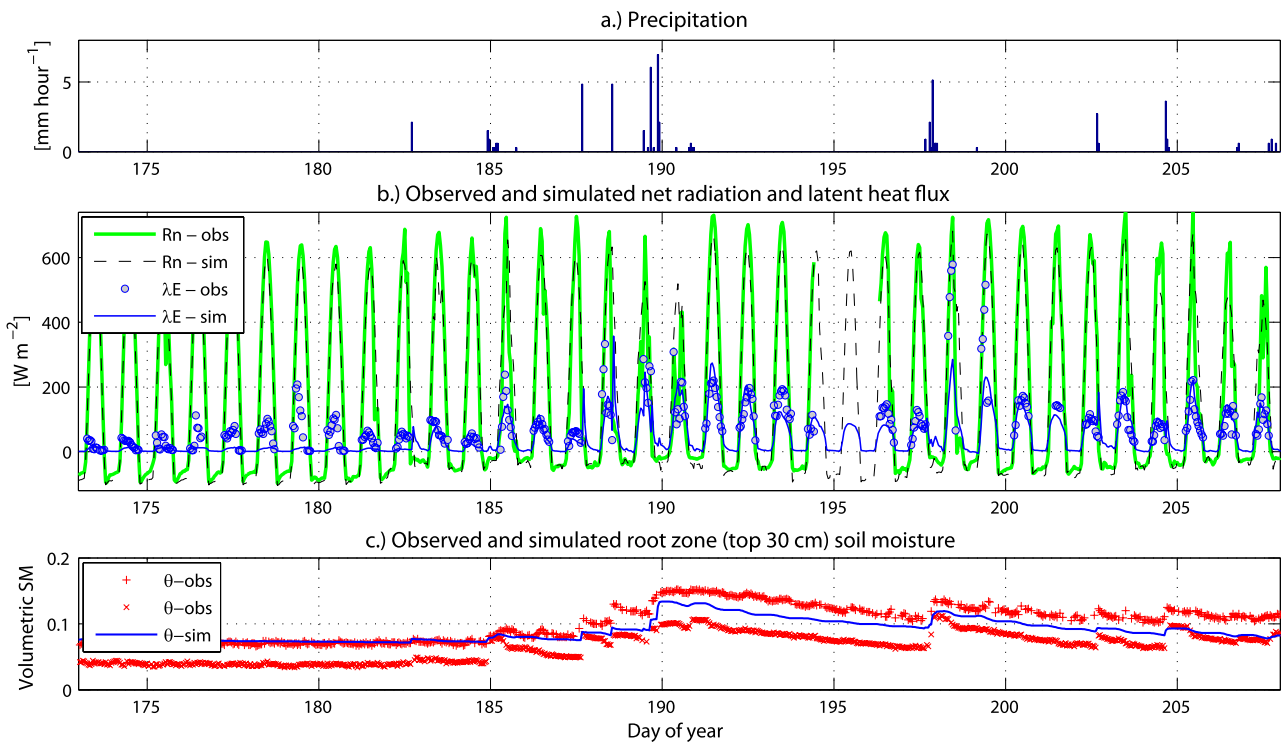
Figure 12. A comparison between observed ("obs") and modeled ("sim") data for the period of 22 June through 26 July 1998, from the continuous 1988–1999 simulation for Deep Well meteorological site in the Sevilleta National Wildlife Refuge: (a) observed rainfall; (b) observed and simulated net radiation (*Rn*) and latent heat (*λE*) flux; (c) measured and simulated volumetric soil moisture for the top 30 cm of soil (assumed to represent grass root zone).

instruction manual for the measurement system that was used at the site. The computed latent heat flux series are filtered to eliminate apparently erroneous, nighttime, sunrise, and dawn flux values.

[122] As one can observe in Figure 12b, the observed and simulated net radiation series show a very good agreement over the period of interest, although the simulated net radiation is somewhat smaller during the peak daytime hours. The net radiation series also exhibit a consistent covariation when weather conditions switch to a wetter period (after day 182), both showing a decrease in nighttime cooling due to the increased heat capacity of wetter soil (Figure 12c).

[123] A fairly prolonged dry period precedes the period of comparison: there were only ~8.8 mm of rainfall since 31 March, with the latest rainfall of ~1.5 mm that occurred on 10 June 1998. Both simulated and derived latent heat flux start with very small values, however, the flux estimated from the observed states exhibits a spurious increase during days 175 through 180. This increase can be explained neither by precipitation records (Figure 12a), nor by measured soil moisture states (Figure 12c) or net radiation (the same pattern of nighttime cooling is preserved as in the preceding days) during that period. Apparently, measurement errors affected the estimation of flux from the Bowen ratio system data and therefore these data need to be interpreted with caution. Throughout the rest of the illustration period, however, the agreement is consistent with the precipitation occurrence and nearly excellent,

except for the hours when latent heat flux almost equals to net radiation.

[124] Measured and modeled volumetric soil moisture in the top 30 cm of soil (assumed to represent grass root zone) are shown in Figure 12c. A potential explanation for the different observations may be that one of the TDR sensors may have been installed in a bare soil fraction, while the other one in a grassy patch. However, no additional information is available to verify this statement. The simulated soil water content is computed as an integral value for a surface that contains both vegetated and bare soil patches (section 8.2). Taking into account this simplification, the assumption of invariant root profile distribution with depth, and the fact that a generic loamy sand soil type was used to parameterize soil hydraulic properties, it can be concluded that the agreement between the series is surprisingly good.

[125] In order to characterize the consistency of simulation results over larger timescales and thus to develop more confidence on the modeling framework, several additional confirmation/verification examples are provided. These results intend to highlight several aspects of energy-water dynamics of vegetated surfaces, reproduced by the model, which are important for the discussion of outcomes of a study presented by *Ivanov et al.* [2008]. For example, Figure 13 shows the mean observed and simulated daily cycles of the net radiation budget and ground heat flux, computed over the interval of 1 June through 15 September 1997–1999 (the observational data for 1996 were not included in this analysis due to a significant gap). The time
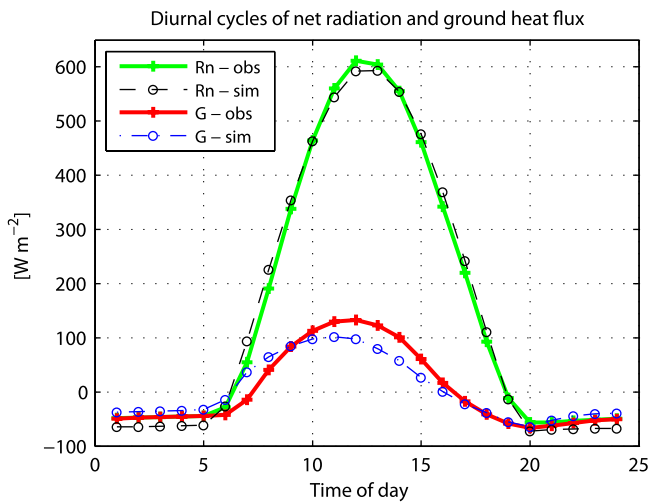
Figure 13. Mean observed and simulated daily cycles of the net radiation budget (*Rn*) and ground heat flux (*G*) for Deep Well meteorological site in the Sevilleta. Data are taken for the interval of 1 June through 15 September for 3 years, 1997–1999, from both observed and simulated series.

interval covers a dry month of June and most of the wetter monsoon period during which the major phase of grass dynamics occurs. The same interval was used by *Kurc and Small* [2004] in their analysis of characteristics of energy and water budgets for the same site in the Sevilleta, which allows for an additional independent qualitative comparison. As can be seen, the agreement between diurnal cycles of net radiation is quite good, although, as in the above example, the estimated cycle is somewhat smaller (<5%) than the observed one during the peak time. The simulated nighttime radiation also tends to be smaller. The simulated soil heat flux cycle appears to be leading the observed cycle. However, the simulated cycle is more consistent with the soil heat flux cycle provided by *Kurc and Small* [2004, Figure 5], which also peaks at around 11 am (2000–2002 analysis period).

[126] Another important metric to compare against is the typical timescale of evapotranspiration response, which describes how quickly the deposited precipitation is returned to the atmosphere. This allows one to characterize how the simulation framework is capable of reproducing persistence characteristics of the modeled vegetation-hydrology system [e.g., *Scott et al.*, 1997]. Since the latent heat flux computed from the variables measured by the Bowen ratio system contains issues at certain periods of time, as demonstrated above, data of *Kurc and Small* [2004] obtained with both Bowen ratio and eddy covariance measurement techniques are used here. Their approach is used in constructing Figure 14, which shows the mean daily evapotranspiration as a function of days since last rainfall over 8 mm until the next measured rainfall (>2 mm). The timescale of response corresponding to the simulated results is longer than the one obtained from the observed data [*Kurc and Small*, 2004, Figure 11]; however, the mismatch between the corresponding sampling periods, 1989–1999

and 2000–2002, introduces uncertainty in the exact interpretation of such a feature. Nonetheless, it should be pointed out that qualitatively the modeled evapotranspiration fluxes exhibit very similar characteristics in terms of both the magnitudes and the decay rate.

[127] Figure 15 complements the above example and illustrates the timescales of soil moisture response integrated over two depths: top 5 cm and top 30 cm (root soil moisture). The observed data show a persistent difference between the data of the two probes, presumably because of the difference of surface properties in locations of sensor placement (e.g., vegetated and bare soil patches). For the most part, the simulated results are within the envelope of observed values. This is yet another evidence of reliability of the modeling approach in reproducing the vegetation-hydrology behavior of a grass system in semiarid environment.

11. Summary

[128] Vegetation plays a fundamental role in the exchange of heat and moisture over a range of spatiotemporal scales by altering surface albedo, roughness, soil macroporosity, intercepting rainfall, uptaking water from deeper soil locations, among other effects. Furthermore, plants adaptively evolve and respond to seasonal and interannual cycles of radiative forcing and water redistribution. Even though the role of vegetation in the physical processes of land-surface energy and water balance is well recognized, the bidirectionality of existing linkages and feedbacks is rarely taken into account.

[129] This paper, of the first two, emphasizes the coupled nature of water, energy, and vegetation dynamics. The study constructs a mechanistic framework that couples a model of plant dynamics to a spatially distributed hydrological model. Among strengths of the approach is the capability of using
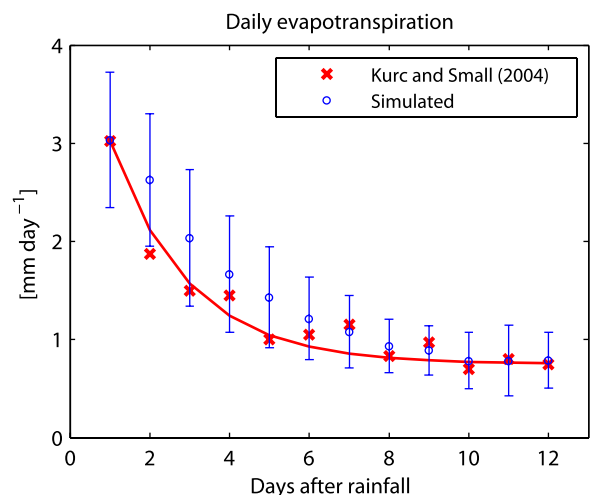
Figure 14. Mean daily evapotranspiration as a function of days since last rainfall over 8 mm for Deep Well meteorological site in the Sevilleta. Both observed and simulated data are taken from the interval of 1 June through 15 September. Observed data are for *Kurc and Small* [2004] study, and the solid line is the fitted exponential model. Simulated data were averaged over the entire simulation period 1989–1999. Error bars show one standard deviation.
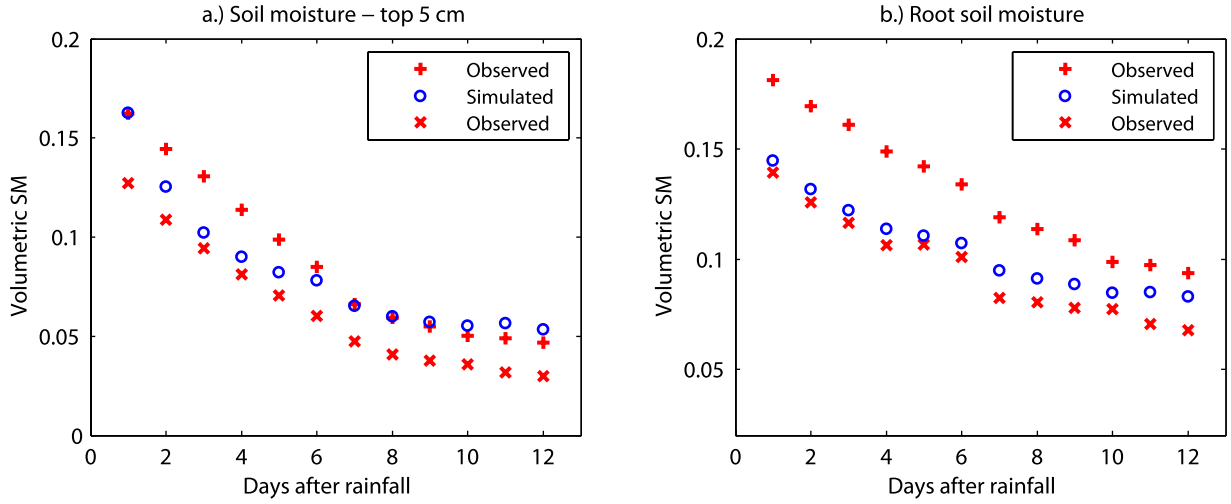
Figure 15. Mean volumetric soil moisture content in the (a) top 5 cm of soil and (b) root zone (top 30 cm, integrating sensors were used) as a function of days since last rainfall over 8 mm for Deep Well meteorological site in the Sevilleta. Data are taken for the interval of 1 June through 15 September for 4 years, 1996–1999, from both observed and simulated series. The observed data are taken for two time domain reflectometry soil moisture sensors, presumably, one of which is installed in a bare soil fraction, while the other one in a grassy patch.

the developed framework for domains of complex geometry, which allows to address a variety of questions of ecohydrology as applied to natural watersheds. The paper discusses existing mechanistic linkages and demonstrates a competent, consistent model performance using observations for a site located in a semiarid environment of central New Mexico. *Ivanov et al.* [2008] further utilize the modeling system to address questions of ecohydrology related to topographic controls of vegetation systems.

Appendix A: Resistances to Heat and Moisture Transfer From Vegetated Surfaces

A1.   Forced Convection

[130] In conditions of forced convection, the conductances c_a^h, c_a^w, c_v^h, c_s^h, c_e^w, c_t^w, and c_s^w [m s^{-1}] are defined as

$$c_a^h = \frac{1}{r_{ah}},$$

$$c_a^w = \frac{1}{r_{aw}},$$

$$c_v^h = \frac{2(L+S)}{r_b},$$

$$c_s^h = \frac{1}{r'_{ah} + r_{ah}},$$

$$c_e^w = f_{wet}\frac{(L+S)}{r_b},$$

$$c_t^w = (1 - f_{wet})\left(\frac{1}{r_b^{sun} + r_s^{sun}} + \frac{1}{r_b^{shd} + r_s^{shd}}\right),$$

$$c_s^w = \frac{1}{r'_{aw} + r_{srf} + r_{aw}},$$

where r'_{ah} and r'_{aw} [s m^{-1}] are the aerodynamic resistances to sensible and latent heat flux between the ground levels z'_{0h}

and z'_{0w} and the heights $z_{0h} + d$ and $z_{0w} + d$ [m], r_b [s m^{-1}] is the one-sided bulk leaf boundary resistance with the appropriate partitioning between sunlit r_b^{sun} and shaded r_b^{shd} fractions of the canopy, r_s^{sun} and r_s^{shd} [s m^{-1}] are the sunlit and shaded canopy stomatal resistances (section 9.1), and f_{wet} [dimensionless] is the wetted fraction of the canopy. Note that the soil moisture state affects the latent heat flux through the stomatal resistances r_s^{sun} and r_s^{shd}, which are estimated explicitly accounting for the soil moisture distribution within the root zone (section 8.2).

[131] The roughness lengths z_{0m}, z_{0h}, and z_{0w} and the displacement height d used to calculate r_{ah} and r_{aw} vary with leaf and stem area and canopy height [*Brutsaert*, 1982; *Sellers et al.*, 1996a]. Here, however, they are considered to be dependent only on vegetation roughness height, according to *Shuttleworth* [1992, p. 4.12]: $d = 0.67\,H_v$, $z_{0m} = 0.123\,H_v$, $z_{0h} = z_{0w} = 0.1\,z_{0m}$, and $z_{atm} = H_M + H_v$, where H_v [m] is the vegetation height and H_M [m] is the standard measurement height (typically $H_M = 2$ m). The heights z'_{0h} and z'_{0w} [m] are the ground roughness lengths used in calculation of the aerodynamic resistances within the canopy, $z'_{0h} = z'_{0w} = 0.005$ m.

[132] The aerodynamic resistances to sensible and latent heat transfer within the canopy r'_{ah} and r'_{aw} are parameterized according to *Choudhury and Monteith* [1988]. Assuming an exponential profile of the eddy diffusivity K_h [m^2 s^{-1}] in the canopy, then

$$r'_{ah} = \frac{H_v}{aK_h(H_v)}\left[e^{a\left(1 - z'_{0h}/H_v\right)} - e^{a\left(1 - (z_{0h}+d)/H_v\right)}\right], \qquad (A1)$$

where $a = 3$ is an empirical parameter [*Bonan*, 1996]. It is assumed that $r'_{ah} = r'_{aw}$ since the roughness lengths for sensible heat and water vapor are identical; $K_h(H_v) = u_*\kappa(H_v - d)$, when the effects of atmospheric stability are ignored and $K_h(H_v)$ is obtained for neutral conditions. The

friction velocity is estimated as $u_* = \kappa \, u_{atm}/\ln\left(\frac{z_{atm}-d}{z_{0m}}\right)$ [m s^{-1}].

[133] The mean one-sided bulk leaf boundary resistance $r_b(z)$ depends on a typical leaf dimension d_{leaf} [m] and wind profile in the canopy as $1/r_b = 0.02/a\sqrt{u(H_v)/d_{leaf}}\,[1-e^{-a/2}]$ [*Choudhury and Monteith*, 1988]. To account appropriately for the latent heat transfer from sunlit and shaded fractions of the canopy: $r_b^{sun} = r_b/L_{sun}$, $r_b^{shd} = r_b/L_{shd}$. In this formulation, these resistances refer to one side of the leaf.

A2. Free Convection

[134] In calm, windless conditions, free convection is the dominant mechanism of the heat transfer from vegetated areas. In the model, for $u_{atm} < 1.0$ m s^{-1}, an empirical approach of *Kondo and Ishida* [1997] is used to parameterize the resistances as functions of empirically obtained bulk transfer coefficients:

$$c_v^h = b'[T_v - T_{atm}]^{\frac{1}{3}},$$

$$c_s^h = b'\left[(T_g - T_{atm}) + 0.11\left(e^*(T_g)h_{soil} - e_{atm}\right)\right]^{\frac{1}{3}},$$

$$c_t^w = (1 - f_{wet})\left(\frac{c_v^h f_{sun}}{1 + c_v^h f_{sun} r_s^{sun}} + \frac{c_v^h f_{shd}}{1 + c_v^h f_{shd} r_s^{shd}}\right),$$

$$c_s^w = \frac{c_s^h}{1 + c_s^h r_{srf}}.$$

Appendix B: Photosynthesis Model

[135] *Collatz et al.* [1991] describe leaf photosynthesis for C$_3$ species as the minimum of three rates, J_c, J_e, and J_s [μmol CO$_2$ m^{-2} leaf s^{-1}] that refer to assimilation rates as limited by the efficiency of the photosynthetic enzyme system (Rubisco-limited), the amount of PAR captured by leaf chlorophyll, and the capacity of the leaf to export or utilize the products of photosynthesis. For C$_4$ species, the terms J_c and J_e still refer to Rubisco and light limitations but J_s refers to a PEP-carboxylase limitation [*Collatz et al.*, 1992]. The formulation below refers to the scale of sunlit/shaded canopy fraction (index CL).

[136] The RuBP-carboxylase (Rubisco enzyme) limited carboxylation rate is formulated as

$$J_c = F^{CL}V_{\max}\left[\frac{c_i - \Gamma^*}{c_i + K_c(1 + O_i/K_o)}\right], \quad \text{for } C_3, \tag{B1}$$

$$J_c = F^{CL} V_{\max}, \quad \text{for } C_4. \tag{B2}$$

The maximum rate of carboxylation allowed by the capacity to regenerate RuBP (i.e., the light limited rate) is

$$J_e = 4.56\phi^{CL}\epsilon_3\left[\frac{c_i - \Gamma^*}{c_i + 2\Gamma^*}\right], \quad \text{for } C_3, \tag{B3}$$

$$J_e = 4.56\,\phi^{CL}\,\epsilon_4, \quad \text{for } C_4. \tag{B4}$$

The export limited rate of carboxylation (for C$_3$ plants) and the PEP-carboxylase limited rate of carboxylation (for C$_4$ plants) are

$$J_s = F^{CL}\,0.5\,V_{\max}, \quad \text{for } C_3, \tag{B5}$$

$$J_s = F^{CL}\,1.8\times10^4\,V_{\max}\frac{c_i}{P_{atm}}, \quad \text{for } C_4. \tag{B6}$$

In the above equations, c_i and O_i [Pa] are the partial pressures of CO$_2$ and O$_2$ in leaf interior, ϕ^{CL} [W m^{-2}] is the amount of the visible solar radiation absorbed by either sunlit or shaded leaves, converted to photosynthetic photon flux assuming 4.56 [μmol photon m^{-2} s^{-1}] per unit absorbed [W m^{-2}], and $\epsilon_{3,4}$ [μmol CO$_2$ μmol^{-1} photons] is the intrinsic quantum efficiency for CO$_2$ uptake for C$_3$ and C$_4$ plants. Γ^* [Pa] is the CO$_2$ compensation point: $\Gamma^* = 0.105\,O_i\,K_c/K_o$, where K_c and K_o [Pa] are the Michaelis-Menten constants for CO$_2$ and O$_2$, expressed as functions of leaf temperature T_v (used here in units of [K]):

$$K_c = K_{c25}\,a_{kc}^{0.1(T_v - 298.15)}, \tag{B7}$$

$$K_o = K_{o25}\,a_{ko}^{0.1(T_v - 298.15)}. \tag{B8}$$

$K_{c25} = 30$ and $K_{o25} = 3\times10^4$ [Pa] are values of constants at 25°C and $a_{kc} = 2.1$ and $a_{ko} = 1.2$ are the temperature sensitivity parameters. The parameter V_{max} [μmol CO$_2$ m^{-2} leaf s^{-1}] is the maximum catalytic capacity of Rubisco:

$$V_{\max} = V_{\max 25}\,a_{vmax}^{0.1(T_v - 298.15)}f_1(T_v)\,\beta_T, \tag{B9}$$

where V_{max25} [μmol CO$_2$ m^{-2} leaf s^{-1}] is the value at 25°C, $a_{vmax} = 2.4$ for C$_3$ species and $a_{vmax} = 2.0$ for C$_4$ species is a temperature sensitivity parameter, and $f(T_v)$ mimics thermal breakdown of metabolic processes [*Farquhar et al.*, 1980; *Collatz et al.*, 1991]:

$$f_1(T_v) = \left[1 + e^{\frac{-220000 + 703\,T_v}{8.314\,T_v}}\right]^{-1}, \quad \text{for } C_3, \tag{B10}$$

$$f_1(T_v) = \left[\left(1 + e^{0.3\,(T_v - 309.15)}\right)\left(1 + e^{0.3\,(286.15 - T_v)}\right)\right]^{-1}, \quad \text{for } C_4. \tag{B11}$$

The expression for a heuristic function β_T [dimensionless] that limits canopy photosynthesis based on the soil moisture availability in the root zone [*Bonan*, 1996]:

$$\beta_T = \sum_{i}^{I_{root}} \beta_{T,i}(z_i)\,r_i(z_i), \tag{B12}$$

$$\beta_{T,i}(z_i) = \max\left[0,\ \min\left(1,\ \frac{\theta_i(z_i) - \theta_w}{\theta^* - \theta_w}\right)\right], \quad \text{if } T_{soil} > 273.15, \tag{B13}$$

$$\beta_{T,i}(z_i) = 0.01, \quad \text{if } T_{soil} \le 273.15, \tag{B14}$$

where index i, $i = 1 \ldots I_{root}$ refers to a depth z_i of the soil profile with an associated root biomass fraction $r_i(z_i)$ (section 8.2), θ_w [mm^3 mm^{-3}] is the wilting point and θ^* [mm^3 mm^{-3}] is the threshold soil moisture contents for a given vegetation type (section 4). T_{soil} is used to constrain transpiration if soil temperature drops below the freezing point. As can be seen from (B12), $\beta_T \in [0, 1]$ takes into account soil moisture variability within the root profile since explicit weights of the root biomass with depth, r_i, are considered.

[137] Observations indicate that the transition from one limiting rate (J_c, J_e, and J_s) to another is not abrupt and that coupling between the three processes leads to smooth curves rather than superposition of straight lines. *Collatz et al.* [1991] describe this effect by combining the rate terms into two quadratic equations, which are then solved for their smaller roots:

$$\alpha_{ce} J_p^2 - J_p(J_c + J_e) + J_e J_c = 0,$$
$$\alpha_{ps} \left(A^{CL}\right)^2 - A^{CL}\left(J_p + J_s\right) + J_p J_s = 0, \tag{B15}$$

where J_p [μmol CO$_2$ m^{-2} leaf s^{-1}] is a "smoothed" minimum of J_c and J_e, A^{CL} [μmol CO$_2$ m^{-2} s^{-1}] is the gross assimilation rate of sunlit or shaded canopy fraction, α_{ce} and α_{ps} are the coupling coefficients defined as $\alpha_{ce} = 0.98$, $\alpha_{ps} = 0.95$ for C$_3$ species [*Sellers et al.*, 1996b]; $\alpha_{ce} = 0.83$, $\alpha_{ps} = 0.90$ for C$_4$ species [*Cox et al.*, 1998].

[138] The net foliage assimilation rate A_n^{CL} is then given by

$$A_n^{CL} = A^{CL} - F^{CL} R_d, \tag{B16}$$

where R_d [μmol CO$_2$ m^{-2} leaf s^{-1}] is leaf mitochondrial ("dark") respiration estimated following *Collatz et al.* [1991, 1992] as

$$R_d = 0.015 \, V_{max\,25} \, a_{rmax}^{0.1(T_v - 298.15)} f_2(T_v), \quad \text{for C}_3, \tag{B17}$$

$$R_d = 0.025 \, V_{max\,25} \, a_{rmax}^{0.1(T_v - 298.15)} f_2(T_v), \quad \text{for C}_4, \tag{B18}$$

where $a_{vmax} = 2.0$ is a temperature sensitivity parameter and $f_2(T_v)$ is a temperature inhibition function: $f_2(T_v) = [1 + e^{1.3(T_v - 328.15)}]^{-1}$. The CO$_2$ concentration at the leaf surface c_s [Pa] and the internal leaf CO$_2$ concentration c_i [Pa] are assumed to be representative for a considered canopy level (sunlit or shaded) and calculated assuming that the capacity to store CO$_2$ at the leaf surface is negligible, so that using the Fick's first law,

$$A_n^{CL} = \frac{c_{atm} - c_i}{\left(1.37 \, r_b^{CL} + 1.65 \, r_s^{CL}\right) P_{atm}} = \frac{c_{atm} - c_s}{1.37 \, r_b^{CL} P_{atm}} = \frac{c_s - c_i}{1.65 \, r_s^{CL} P_{atm}}, \tag{B19}$$

where $c_{atm} = 340 \times 10^{-6} P_{atm}$ [Pa] is the background atmospheric CO$_2$ concentration, the coefficients 1.37 and 1.65 are the ratios of diffusivity of CO$_2$ to H$_2$O for the leaf boundary layer resistance and stomatal resistance [*von Caemmerer and Farquhar*, 1981; *Landsberg*, 1986], and r_b^{CL} [s m^2 μmol^{-1}] is the one-sided bulk leaf boundary

resistance estimated for sunlit or shaded fraction of the canopy:

$$r_b^{CL} = r_b^{sun, shd} \frac{0.0224 \, (1.013 \times 10^5) \, T_{atm}}{P_{atm} \, 273.15} \times 10^{-6}, \tag{B20}$$

where $r_b^{sun, shd}$ is given in [s m^{-1}].

[139] Both the productivity A_n^{CL} and the stomatal resistance r_s^{CL} are a function of the internal leaf CO$_2$ concentration c_i [Pa], which is a function of leaf temperature and atmospheric moisture deficit. Since c_i is unknown, the estimation of r_s^{CL} and A_n^{CL} is therefore formulated as a problem of finding c_i as the root of a nonlinear equation (follows from (B19)): $(c_s(c_i) - 1.65 \, r_s^{CL}(c_i) \, A_n^{CL}(c_i) \, P_{atm}) - c_i = 0$ using the Newton method [*Ivanov*, 2006].

[140] The nighttime stomatal resistance is a function of the minimum stomatal conductance and soil water stress. Taking $r_s^{sun} \to \infty$, the nighttime stomatal resistance is formulated as $r_s^{shd} = 1/(\beta_T \, b \, L)$, where L is the canopy total leaf area index.

References

Arora, V. K., and G. J. Boer (2005), A parameterization of leaf phenology for the terrestrial ecosystem component of climate models, *Global Change Biol.*, 11(1), 39–59.

Arya, S. P. (2001), *Introduction to Micrometeorology*, 2nd ed., 420 pp. Academic, New York.

Band, L. E., P. Patterson, R. Nemani, and S. W. Running (1993), Forest ecosystem processes at the watershed scale—Incorporating hillslope hydrology, *Agric. For. Meteorol.*, 63(1-2), 93–126.

Ben Wu, X., and S. R. Archer (2005), Scale-dependent influence of topography-based hydrologic features on patterns of woody plant encroachment in savanna landscapes, *Landscape Ecol.*, 20(6), 733–742.

Beyschlag, W., O. L. Lange, and J. D. Tenhunen (1986), Photosynthesis and water relations of the Mediterranean evergreen sclerophyll *Arbutus unedo* L. throughout the year at a site in Portugal. 1. Diurnal courses of CO$_2$ gas-exchange and transpiration under natural conditions, *Flora*, 178(6), 409–444.

Bonan, G. B. (1995), Land-atmosphere interactions for climate system models—Coupling biophysical, biogeochemical, and ecosystem dynamical processes, *Remote Sens. Environ.*, 51(1), 57–73.

Bonan, G. B. (1996), A land surface model (LSM version 1.0) for ecological, hydrological, and atmospheric studies: Technical description and user's guide, *NCAR Tech. Note NCAR/TN-417*, Natl. Cent. for Atmos. Res., Boulder, Colo.

Bonan, G. B., S. Levis, L. Kergoat, and K. W. Oleson (2002), Landscapes as patches of plant functional types: An integrating concept for climate and ecosystem models, *Global Biogeochem. Cycles*, 16(2), 1021, doi:10.1029/2000GB001360.

Bras, R. L. (1990), *An Introduction to Hydrologic Science*, 643 pp., Addison-Wesley-Longman, Reading, Mass.

Bras, R. L., G. E. Tucker, and V. Teles (2003), Six myths about mathematical modeling in geomorphology, in *Prediction in Geomorphol.*, Geophys. Monogr. Ser., vol. 135, edited by P. Wilcock and R. Iverson, pp. 63-82, AGU.

Brooks, R. H., and A. T. Corey (1964), *Hydraulic Properties of Porous Media, Hydrol. Pap. 3*, Colo. State Univ., Fort Collins.

Brutsaert, W. (1982), *Evaporation Into the Atmosphere: Theory, History, and Applications*, D. Reidel, Dordecht, Netherlands.

Campbell, D. I. (1989), Energy-balance and transpiration from tussock grassland in New-Zealand, *Boundary Layer Meteorol.*, 46(1–2), 133–152.

Choudhury, B. J., and J. L. Monteith (1988), A 4-layer model for the heat-budget of homogeneous land surfaces, *Q. J. R. Meteorol. Soc.*, *114*(480), 373–398.

Collatz, G. J., J. T. Ball, C. Grivet, and J. A. Berry (1991), Physiological and environmental regulation of stomatal conductance, photosynthesis and transpiration—A model that includes a laminar boundary-layer, *Agric. For. Meteorol.*, *54*(2–4), 107–136.

Collatz, G. J., M. Ribas-Carbo, and J. A. Berry (1992), Coupled photosynthesis-stomatal conductance model for leaves of C4 plants, *Aust. J. Plant Physiol.*, *19*(5), 519–538.

Cordova, J. R., and R. L. Bras (1981), Physically-based probablistic models of infiltration, soil moisture, and actual evapotranspiration, *Water Resour. Res.*, *17*(1), 93–106.

Cox, P. M., C. Huntingford, and R. J. Harding (1998), A canopy conductance and photosynthesis model for use in a GCM land surface scheme, *J. Hydrol.*, *213*(1–4), 79–94.

Cox, P. M., R. A. Betts, C. B. Bunton, R. L. H. Essery, P. R. Rowntree, and J. Smith (1999), The impact of new land surface physics on the GCM simulation of climate and climate sensitivity, *Clim. Dyn.*, *15*(3), 183–203.

Dai, Y. J., R. E. Dickinson, and Y. P. Wang (2004), A two-big-leaf model for canopy temperature, photosynthesis, and stomatal conductance, *J. Clim.*, *17*(12), 2281–2299.

de Pury, D. G. G., and G. D. Farquhar (1997), Simple scaling of photosynthesis from leaves to canopies without the errors of big-leaf models, *Plant Cell Environ.*, *20*(5), 537–557.

De Vries, D. A. (1963), Thermal properties of soils, in *Physics of Plant Environment*, edited by W. R. van Wijk, pp. 210–233, John Wiley, New York.

Dickinson, R. E. (1983), Land surface processes and climate surface albedos and energy balance, *Adv. Geophys.*, *25*, 305–353.

Dickinson, R. E. (2000), How coupling of the atmosphere to ocean and land helps determine the timescales of interannual variability of climate, *J. Geophys. Res.*, *105*(D15), 20,115–20,119.

Dickinson, R. E., A. Henderson-Sellers, and P. J. Kennedy (1993), Biosphere-atmosphere transfer scheme (BATS) version 1E as coupled to the NCAR Community Climate Model, *Tech. Rep. NCAR/TN-387+STR*, Natl. Cent. for Atmos. Res., Boulder, Colo.

Dickinson, R. E., M. Shaikh, R. Bryant, and L. Graumlich (1998), Interactive canopies for a climate model, *J. Clim.*, *11*(11), 2823–2836.

Dietrich, W. E., and J. T. Perron (2006), The search for a topographic signature of life, *Nature*, *439*(7075), 411–418.

Dirnbock, T., R. J. Hobbs, R. J. Lambeck, and P. A. Caccetta (2002), Vegetation distribution in relation to topographically driven processes in southwestern Australia, *Appl. Vegetat. Sci.*, *5*(1), 147–158.

D'Odorico, P., L. Ridolfi, A. Porporato, and I. Rodriguez-Iturbe (2000), Preferential states of seasonal soil moisture: The impact of climate fluctuations, *Water Resour. Res.*, *36*(8), 2209–2219.

Eagleson, P. S. (1978a), Climate, soil, and vegetation 1. Introduction to water balance dynamics, *Water Resour. Res.*, *14*(5), 705–712.

Eagleson, P. S. (1978b), Climate, soil, and vegetation 2. The Distribution of annual precipitation derived from observed storm sequences, *Water Resour. Res.*, *14*(5), 713–721.

Eagleson, P. S. (1978c), Climate, soil, and vegetation 3. A Simplified model of soil moisture movement in the liquid phase, *Water Resour. Res.*, *14*(5), 722–730.

Eagleson, P. S. (1978d), Climate, soil, and vegetation 4. The expected value of annual evapotranspiration, *Water Resour. Res.*, *14*(5), 731–739.

Eagleson, P. S. (1978e), Climate, soil, and vegetation 5. A derived distribution of storm surface runoff, *Water Resour. Res.*, *14*(5), 741–748.

Eagleson, P. S. (1978f), Climate, soil, and vegetation 6. Dynamics of the annual water balance, *Water Resour. Res.*, *14*(5), 749–764.

Eagleson, P. S. (1978g), Climate, soil, and vegetation 7. A Derived distribution of annual water yield, *Water Resour. Res.*, *14*(5), 765–776.

Eagleson, P. S. (2002), *Ecohydrology: Darwinian Expression of Vegetation Form and Function*, 496 pp. Cambridge Univ. Press, Cambridge, U.K.

Eltahir, E. A. B. (1996), Role of vegetation in sustaining large-scale atmospheric circulations in the tropics, *J. Geophys. Res.*, *101*(D2), 4255–4268.

Eltahir, E. A. B., and R. L. Bras (1993), A Description of rainfall interception over large-areas, *J. Clim.*, *6*, 1002–1008.

Farouki, O. T. (1981), *Thermal Properties of Soils, CRREL Monogr. 81-1*, pp. 134, U.S. Army Cold Reg. Res. and Eng. Lab., Hanover, N. H.

Farquhar, G. D., and S. von Caemmerer (1982), Modelling of photosynthetic response to environmental conditions, in *Encyclopedia of plant physiology. Physiological Plant Ecology II.* edited by O. L. Lange et al., pp. 550-587, Springer, Berlin, Germany.

Farquhar, G. D., S. von Caemmerer, and J. A. Berry (1980), A biochemical model of photosynthetic CO_2 assimilation in leaves of C-3 species, *Planta*, *149*(1), 78–90.

Field, C., and H. A Mooney (1986), The photosynthesis-nitrogen relationship in wild plants, in *On the economy of plant form and function*, edited by T. J. Givnish, pp. 25-55, Cambridge Univ. Press, Cambridge, U. K.

Florinsky, I. V., and G. A. Kuryakova (1996), Influence of topography on some vegetation cover properties, *Catena*, *27*(2), 123–141.

Foley, J. A., I. C. Prentice, N. Ramankutty, S. Levis, D. Pollard, S. Sitch, and A. Haxeltine (1996), An integrated biosphere model of land surface processes, terrestrial carbon balance, and vegetation dynamics, *Global Biogeochem. Cycles*, *10*(4), 603–628.

Foley, J. A., S. Levis, M. H. Costa, W. Cramer, and D. Pollard (2000), Incorporating dynamic vegetation cover within global climate models, *Ecol. Appl.*, *10*(6), 1620–1632.

Francois, C., C. Ottle, and L. Prevot (1997), Analytical parameterization of canopy directional emissivity and directional radiance in the thermal infrared. Application on the retrieval of soil and foliage temperatures using two directional measurements, *Int. J. Remote Sens.*, *18*, 2587–2621.

Franklin, J. (1998), Predicting the distribution of shrub species in southern California from climate and terrain-derived variables, *J. Vegetat. Sci.*, *9*(5), 733–748.

Friedlingstein, P., G. Joel, C. B. Field, and I. Y. Fung (1999), Toward an allocation scheme for global terrestrial carbon models, *Global Change Biol.*, *5*(7), 755–770.

Friend, A. D., A. K. Stevens, R. G. Knox, and M. G. R. Cannell (1997), A process-based, terrestrial biosphere model of ecosystem dynamics (Hybrid v3.0), *Ecol. Model.*, *95*(2-3), 249–287.

Garrote, L., and R. L. Bras (1995), A distributed model for real-time flood casting using digital elevation models, *J. Hydrol.*, *167*, 279–306.

Gueymard, C. (1989), A 2-band model for the calculation of clear sky solar irradiance, illuminance, and photosynthetically active radiation at the earth's surface, *Sol. Energy*, *43*(5), 253–265.

Guswa, A. J., M. A. Celia, and I. Rodriguez-Iturbe (2002), Models of soil moisture dynamics in ecohydrology: A comparative study, *Water Resour. Res.*, *38*(9), 1166, doi:10.1029/2001WR000826.

Haxeltine, A., and I. C. Prentice (1996), BIOME3: An equilibrium terrestrial biosphere model based on ecophysiological constraints, resource availability, and competition among plant functional types, *Global Biogeochem. Cycles*, *10*(4), 693–709.

Hillel, D. (1980), *Fundamentals of Soil Physics*, 413 pp. Academic, New York.

Hutjes, R. W. A., et al. (1998), Biospheric aspects of the hydrological cycle—Preface, *J. Hydrol.*, *213*(1–4), 1–21.

Ingestad, T., and B. B. Lund (1986), Theory and techniques for steady state mineral nutrition and growth of plants, *Scand. J. For. Res.*, *1*, 439–453.

Ivanov, V. Y. (2006), Effects of dynamic vegetation and topography on hydrological processes in semi-arid areas, Ph.D. thesis, Mass. Inst. of Technol., Cambridge.

Ivanov, V. Y., E. R. Vivoni, R. L. Bras, and D. Entekhabi (2004a), Catchment hydrologic response with a fully distributed triangulated irregular network model, *Water Resour. Res.*, *40*, W11102, doi:10.1029/2004WR003218.

Ivanov, V. Y., E. R. Vivoni, R. L. Bras, and D. Entekhabi (2004b), Preserving high-resolution surface and rainfall data in operational-scale basin hydrology: A fully-distributed physically-based approach, *J. Hydrol.*, *298*(1–4), 80–111.

Ivanov, V. Y., R. L. Bras, and D. C. Curtis (2007), A weather generator for hydrological, ecological, and agricultural applications, *Water Resour. Res.*, *43*, W10406, doi:10.1029/2006WR005364.

Ivanov, V. Y., R. L. Bras, and E. R. Vivoni (2008), Vegetation-hydrology dynamics in complex terrain of semiarid areas: 2. Energy-water controls of vegetation spatiotemporal dynamics and topographic niches of favorability, *Water Resour. Res.*, *44*, W03430, doi:10.1029/2006WR005595.

Jackson, R. B., J. Canadell, J. R. Ehleringer, H. A. Mooney, O. E. Sala, and E. D. Schulze (1996), A global analysis of root distributions for terrestrial biomes, *Oecologia*, *108*(3), 389–411.

Kim, Y., and E. A. B. Eltahir (2004), Role of topography in facilitating coexistence of trees and grasses within savannas, *Water Resour. Res.*, *40*, W07505, doi:10.1029/2003WR002578.

Kinyamario, J. I., and S. K. Imbamba (1992), Savanna at Nairobi National Park, Nairobi, in *Primary Productivity of Grass Ecosystems of the Tropics and Sub-Tropics*, edited by S. P. Long, M. B. Jones, and M. J. Roberts, pp. 25-69, Chapman and Hall, Pdastow, U.K.

Kondo, J., and S. Ishida (1997), Sensible heat flux from the earth's surface under natural convective conditions, *J. Atmos. Sci.*, *54*(4), 498–509.

Konikow, L. F., and J. D. Bredehoeft (1992), Ground-water models cannot be validated, *Adv. Water Resour.*, *15*, 75–83.

Krinner, G., N. Viovy, N. de Noblet-Ducoudr, J. Oge, J. Polcher, P. Friedlingstein, P. Ciais, S. Sitch, and I. C. Prentice (2005), A dynamic global vegetation model for studies of the coupled atmosphere-biosphere system, *Global Biogeochem. Cycles*, *19*, GB1015, doi:10.1029/2003GB002199.

Kucharik, C. J., J. A. Foley, C. Delire, V. A. Fisher, M. T. Coe, J. D. Lenters, C. Young-Molling, N. Ramankutty, J. M. Norman, and S. T. Gower (2000), Testing the performance of a dynamic global ecosystem model: Water balance, carbon balance, and vegetation structure, *Global Biogeochem. Cycles*, *14*(3), 795–825.

Kurc, S. A., and E. E. Small (2004), Dynamics of evapotranspiration in semiarid grassland and shrubland ecosystems during the summer monsoon season, central New Mexico, *Water Resour. Res.*, *40*, W09305, doi:10.1029/2004WR003068.

Laio, F., A. Porporato, L. Ridolfi, and I. Rodriguez-Iturbe (2001a), Plants in water-controlled ecosystems: Active role in hydrologic processes and response to water stress – II. Probabilistic soil moisture dynamics, *Adv. Water Resour.*, *24*(7), 707–723.

Laio, F., A. Porporato, C. P. Fernandez-Illescas, and I. Rodriguez-Iturbe (2001b), Plants in water-controlled ecosystems: Active role in hydrologic processes and response to water stress – IV. Discussion of real cases, *Adv. Water Resour.*, *24*(7), 745–762.

Landsberg, J. J. (1986), *Physiological Ecology of Forest Production*, 198 pp. Academic, London.

Larcher, W. (2001), *Physiological Plant Ecology*, 4th ed., 513 pp. Springer, New York.

Leuning, R. (1995), A critical appraisal of a combined stomatal-photosynthesis model for C-3 plants, *Plant Cell Environ.*, *18*(4), 339–355.

Levin, S. A. (1998), Ecosystems and the biosphere as complex adaptive systems, *Ecosystems*, *1*, 431–436.

Levis, S., G. B. Bonan, M. Vertenstein, K. W. Oleson (2004), The Community Land Model's Dynamic Global Vegetation Model (CLM-DGVM): Technical description and user's guide, *Tech. Note NCAR/TN-459+IA*, Natl. Cent. for Atmos. Res., Boulder, Colo.

Lewis, J. M. (1995), The story behind the Bowen ratio, *Bull. Am. Meteorol. Soc.*, *76*(12), 2433–2443.

Ludeke, M. K. B., et al. (1994), The Frankfurt biosphere model: A global process-oriented model of seasonal and long-term CO2 exchange between terrestrial ecosystems and the atmosphere. I. Model description and illustrative results for cold deciduous and boreal forests, *Clim. Res.*, *4*(2), 143–166.

Mackay, D. S. (2001), Evaluation of hydrologic equilibrium in a mountainous watershed: Incorporating forest canopy spatial adjustment to soil biogeochemical processes, *Adv. Water Resour.*, *24*(9-10), 1211–1227.

Meentemeyer, R. K., A. Moody, and J. Franklin (2001), Landscape-scale patterns of shrub-species abundance in California chaparral—The role of topographically mediated resource gradients, *Plant Ecol.*, *156*(1), 19–41.

Milne, B. T., D. I. Moore, J. L. Betancourt, J. A. Parks, T. W. Swetnam, R. R. Parmenter, and W. T. Pockman (2003), Multidecadal drought cycles in south-central New Mexico: Patterns and consequences, in *Climate Variability and Ecosystem Response at Long-Term Ecological Research Sites*, edited by D. Greenland, D. G. Goodin, and R. C. Smith, pp. 286-307 Oxford Univ. Press, New York.

Monsi, M., and T. Saeki (2005), On the factor light in plant communities and its importance for matter production, *Ann. Bot.*, *95*, 549–567.

Norman, J. M. (1993), Scaling processes between leaf and canopy levels, in *Scaling Physiological Processes: Leaf to Globe*, edited by J. Ehleringer and C. Field pp. 41-76, Academic, New York.

Oleson, K., et al. (2004), Technical Description of the Community Land Model (CLM), *Tech. Note NCAR/TN-461+STR*, Natl. Cent. for Atmos. Res., Boulder, Colo.

Oreskes, N., K. Shrader-Frechette, and K. Belitz (1994), Verification, validation and confirmation of numerical models in the earth sciences, *Science*, *263*, 641–646.

Penning De Vries, F. W. T. (1975), Cost of maintenance processes in plant-cells, *Ann. Bot.*, *39*(159), 77–92.

Peters, D. P. C. (2000), Climatic variation and simulated patterns in seedling establishment of two dominant grasses at a semi-arid grassland ecotone, *J. Vegetat. Sci.*, *11*(4), 493–504.

Philip, J. R. (1957), Evaporation, and moisture and heat fields in the soil, *J. Meteorol.*, *14*, 354–366.

Philip, J. R. (1991), Hillslope infiltration—Planar slopes, *Water Resour. Res.*, *27*(1), 109–117.

Pielke, R. A. (2001), Influence of the spatial distribution of vegetation and soils on the prediction of cumulus convective rainfall, *Rev. Geophys.*, *39*(2), 151–177.

Protopapas, A. L., and R. L. Bras (1987), A model for water-uptake and development of root systems, *Soil Sci.*, *144*(5), 352–366.

Protopapas, A. L., and R. L. Bras (1988), State-space dynamic hydrological modeling of soil-crop-climate interactions, *Water Resour. Res.*, *24*(10), 1765–1779.

Rawls, W. J., D. L. Brakensiek, and K. E. Saxton (1982), Estimation of soil-water properties, *Trans. ASAE*, *25*(5), 1316–1320.

Refsgaard, J. C., and H. J. Henriksen (2004), Modelling guidelines terminology and guiding principles, *Adv. Water Resour.*, *27*, 71–82.

Ridolfi, L., P. D'Odorico, A. Porporato, and I. Rodriguez-Iturbe (2000a), Duration and frequency of water stress in vegetation: An analytical model, *Water Resour. Res.*, *36*(8), 2297–2307.

Ridolfi, L., P. D'Odorico, A. Porporato, and I. Rodriguez-Iturbe (2000b), Impact of climate variability on the vegetation water stress, *J. Geophys. Res.*, *105*(D14), 18,013–18,025.

Rodriguez-Iturbe, I. (2000), Ecohydrology: A hydrologic perspective of climate-soil-vegetation dynamics, *Water Resour. Res.*, *36*(1), 3–9.

Rodriguez-Iturbe, I., A. Porporato, L. Ridolfi, V. Isham, and D. R. Cox (1999a), Probabilistic modelling of water balance at a point: The role of climate, soil and vegetation, *Proc. R. Soc. London Ser. A*, *455*(1990), 3789–3805.

Rodriguez-Iturbe, I., P. D'Odorico, A. Porporato, and L. Ridolfi (1999b), On the spatial and temporal links between vegetation, climate, and soil moisture, *Water Resour. Res.*, *35*(12), 3709–3722.

Rodriguez-Iturbe, I., A. Porporato, F. Laio, and L. Ridolfi (2001), Plants in water-controlled ecosystems: Active role in hydrologic processes and response to water stress – I. Scope and general outline, *Adv. Water Resour.*, *24*(7), 695–705.

Rutter, A. J., K. A. Kershaw, P. C. Robins, and A. J. Morton (1971), A predictive model of rainfall interception in forests. 1. Derivation of the model from observation in a plantation of Corsican pine, *Agric. Meteorol.*, *9*, 367–384.

Rutter, A. J., A. J. Morton, and P. C. Robins (1975), Predictive model of rainfall interception in forests. 2. Generalization of model and comparison with observations in some coniferous and hardwood stands, *J. Appl. Ecol.*, *12*(1), 367–380.

Rykiel, E. R. (1996), Testing ecological models: The meaning of validation, *Ecol. Model.*, *90*, 229–244.

Saeki, T. (1961), Inter-relationship between leaf amount, light distribution, and total photosynthesis in a plant community, *Bot. Mag.*, *11*, 235–241.

Salter, M. G., K. A. Franklin, and G. C. Whitelam (2003), Gating of the rapid shade-avoidance response by the circadian clock in plants, *Nature*, *426*(6967), 680–683.

Schlesinger, S., et al. (1979), Terminology for model credibility, *Simulation*, *32*(3), 103–104.

Schmid, H. P., H.-B. Su, C. S. Vogel, and P. S. Curtis (2003), Ecosystem-atmosphere exchange of carbon dioxide over a mixed hardwood forest in northern lower Michigan, *J. Geophys. Res.*, *108*(D14), 4417, doi:10.1029/2002JD003011.

Scholes, R. J., and B. H. Walker (1993), *An African Savanna: Synthesis of the Nylsvley Study*, 318 pp., Cambridge Univ. Press, Cambridge, U.K.

Scott, R., D. Entekhabi, R. Koster, and M. Suarez (1997), Timescales of land surface evapotranspiration response, *J. Clim.*, *10*, 559–566.

Sellers, P. J. (1985), Canopy reflectance, photosynthesis and transpiration, *Int. J. Remote Sens.*, *6*(8), 1335–1372.

Sellers, P. J., J. A. Berry, G. J. Collatz, C. B. Field, and F. G. Hall (1992), Canopy reflectance, photosynthesis, and transpiration. 3. A reanalysis using improved leaf models and a new canopy integration scheme, *Rem. Sens. Environ.*, *42*(3), 187–216.

Sellers, P. J., D. A. Randall, G. J. Collatz, J. A. Berry, C. B. Field, D. A. Dazlich, C. Zhang, G. D. Collello, and L. Bounoua (1996a), A revised land surface parameterization (SiB2) for atmospheric GCMs. 1. Model formulation, *J. Clim.*, *9*(4), 676–705.

Sellers, P. J., S. O. Los, C. J. Tucker, C. O. Justice, D. A. Dazlich, G. J. Collatz, and D. A. Randall (1996b), A revised land surface parameterization (SiB2) for atmospheric GCMs. 2. The generation of global fields of terrestrial biophysical parameters from satellite data, *J. Clim.*, *9*(4), 706–737.

Shinozaki, K., K. Yoda, K. Hozumi, and T. Kira (1964), A quantitative analysis of plant form: The pipe model theory. I. Basic analyses, *Jpn. J. Ecol.*, *14*, 97–105.

Shuttleworth, W. J. (1979), Evaporation, *Report 56*, Inst.e of Hydrol., Wallingford, UK.

Shuttleworth, W. J. (1992), Evaporation, in *Handbook of Hydrology*, edited by D. R. Maidment, pp. 4.1-4.53, McGraw-Hill, New York.

Sitch, S., B. Smith, I. C. Prentice, A. Arneth, A. Bondeau, W. Cramer, J. O. Kaplan, S. Levis, W. Lucht, M. T. Sykes, K. Thonicke, and S. Venevsky (2003), Evaluation of ecosystem dynamics, plant geography and terrestrial carbon cycling in the LPJ dynamic global vegetation model, *Global Change Biol.*, *9*(2), 161–185.

Smith, T. M., H. H. Shugart, and F. I. Woodward (1997), *Plant Functional Types: Their Relevance to Ecosystem Properties and Global Change, Int. Geosphere Biosphere Programme Book Ser.*, vol. 1, 369 pp., Cambridge Univ. Press, New York.

Spitters, C. J. T. (1986), Separating the diffuse and direct component of global radiation and its implications for modeling canopy photosynthesis. 2. Calculation of canopy photosynthesis, *Agric. For. Meteorol.*, *38*(1–3), 231–242.

Taiz, L., and E. Zeiger (2002), *Plant Physiology*, 3rd ed., 690 pp. Sinauer Assoc., Inc., Sunderland, Mass.

Tan, C. S., and T. A. Black (1976), Factors affecting the canopy resistance of a Douglas-fir forest, *Boundary Layer Meteorol.*, *10*, 475–488.

Tilman, D. (1994), Competition and biodiversity in spatially structured habitats, *Ecology*, *75*, 2–16.

Tucker, G. E., S. T. Lancaster, N. M. Gasparini, R. L. Bras, and S. M. Rybarczyk (2001), An object-oriented framework for distributed hydrologic and geomorphic modeling using triangulated irregular networks, *Comput. Geosci.*, *27*(8), 959–973.

Urban, D. L., R. V. O'Neill, and H. H. Shugart (1987), Landscape ecology, *BioScience*, *37*, 119–127.

van Wijk, M. T., and I. Rodriguez-Iturbe (2002), Tree-grass competition in space and time: Insights from a simple cellular automata model based on ecohydrological dynamics, *Water Resour. Res.*, *38*(9), 1179, doi:10.1029/2001WR000768.

Vivoni, E. R., V. Y. Ivanov, R. L. Bras, and D. Entekhabi (2004), Generation of triangulated irregular networks based on hydrological similarity, *J. Hydrol. Eng.*, *9*(4), 288–302.

von Caemmerer, S., and G. D. Farquhar (1981), Some relationships between the biochemistry of photosynthesis and the gas exchange of leaves, *Planta*, *153*, 376–387.

Wang, G. L., and E. A. B. Eltahir (2000), Biosphere-atmosphere interactions over West Africa. II: Multiple climate equilibria, *Q. J. R. Meteorol. Soc.*, *126*(565), 1261–1280.

Wang, J., and R. L. Bras (1999), Ground heat flux estimated from surface soil temperature, *J. Hydrol.*, *216*(3–4), 214–226.

Wang, Y. P., and P. G. Jarvis (1990), Description and validation of an array model—MAESTRO, *Agric. For. Meteorol.*, *51*(3–4), 257–280.

Wang, Y. P., and R. Leuning (1998), A two-leaf model for canopy conductance, photosynthesis and partitioning of available energy I: Model description and comparison with a multi-layered model, *Agric. For. Meteorol.*, *91*(1–2), 89–111.

Waring, R. H., P. E. Schroeder, and R. Oren (1982), Application of the pipe model-theory to predict canopy leaf-area, *Can. J. For. Res.*, *12*(3), 556–560.

————————————

R. L. Bras, Department of Civil and Environmental Engineering, Ralph M. Parsons Laboratory 48-213, Massachusetts Institute of Technology, Cambridge, MA 02139, USA. (rlbras@mit.edu)

V. Y. Ivanov, Department of Civil and Environmental Engineering, University of Michigan, 1351 Beal Avenue, 105 EWRE, Ann Arbor, MI 48109-2125, USA. (ivanov@umich.edu)

E. R. Vivoni, MSEC 244, Department of Earth and Environmental Science, New Mexico Institute of Mining and Technology, Socorro, NM 87801, USA. (vivoni@nmt.edu)